Politecnico di Torino

Politecnico di Torino

Master's Degree in Aerospace Engineering

Academic Year 2025/2026

Graduation Session April 2026

Reduced Order Models for the Evaluation of Hypersonic Vehicles Aerothermodynamic Databases

Thesis in collaboration with MBDA Italia

Supervisors:

Prof. Domenic D'AMBROSIO

Ing. Immacolata CASTALDO

Candidate:

Daniele MINI

Acknowledgements

I am deeply grateful to Prof. Domenic D'Ambrosio, my internal supervisor, and to Eng. Immacolata Castaldo, my industrial tutor at MBDA Italy, for their guidance and support throughout the development of this thesis.

I especially thank Prof. D'Ambrosio for the passion and curiosity he demonstrated in computational fluid dynamics and hypersonic aerothermodynamics. His rigorous approach and enthusiasm for the subject have represented an important point of reference and a source of inspiration, helping to shape my academic path.

A special thanks to Imma for her valuable technical support and for guiding me through the project's practical development. Her passion, inclusivity, and constant willingness to engage in discussion have been fundamental throughout the entire journey. I am also grateful to her for her support and patience, especially during the last month, and for all the advice that contributed concretely both to the success of this work and to my professional growth.

I would also like to extend my gratitude to MBDA, and in particular to the Aerodynamics Team, for the opportunity to carry out this thesis in a highly stimulating and professional environment, allowing me to engage with real-world engineering challenges in hypersonic aerodynamics.

Abstract

Hypersonic flight has attracted increasing interest in recent decades due to its importance in both civil and military aerospace applications. However, predicting the aerodynamic forces acting on vehicles operating in the hypersonic regime is particularly challenging because of the complex physical phenomena involved. Although high-fidelity Computational Fluid Dynamics (CFD) simulations generate accurate solutions, their computational cost often makes them unsuitable for rapid design iterations and large parametric studies.

This thesis, carried out in collaboration with MBDA Italia, focuses on the development of a reduced-order computational framework for the rapid evaluation of aerodynamic characteristics of hypersonic configurations. A MATLAB-based tool has been developed to compute the main aerodynamic coefficients directly from three-dimensional geometries provided as STL surface meshes.

The implemented methodology relies on a combination of classical local surface inclination methods and empirical hypersonic models, where different reduced-order models have been systematically implemented and combined in order to identify the most suitable modeling strategies for distinct geometric regions and flight conditions. The accuracy of the proposed framework was evaluated by comparing the results with high-fidelity CFD simulations performed under inviscid, viscous, and chemically reacting flow assumptions.

The results show that the proposed approach captures the main aerodynamic trends while significantly reducing computational time, making it an effective tool for preliminary aerodynamic assessment and early-stage design studies of hypersonic configurations.

Table of Contents

List of Tables

List of Figures

Chapter 1

Introduction

In recent decades, interest in hypersonic flight has grown remarkably, driven by scientific and technological objectives as well as strategic and military demands. Atmospheric re-entry missions, reusable orbital transport vehicles, hypersonic glide vehicles (HGVs), and high-speed cruise aircraft concepts currently represent the main applications of this regime.

The hypersonic regime features a tight interplay among fluid dynamics, thermal, and chemical phenomena, leading to a highly nonlinear aerothermodynamic response. Resolving these interactions with sufficient accuracy generally requires high-fidelity CFD solvers based on the Navier–Stokes equations that incorporate real-gas models.

However, the computational cost associated with these simulations is often prohibitive, especially during conceptual iterative design and large-scale preliminary analyses, when it is necessary to explore wide flight envelopes across Mach number, angle of attack, altitude, and complex geometric configurations.

In this context, the use of Reduced Order Models (ROMs) becomes particularly advantageous, as they enable the rapid and efficient reconstruction of the aerodynamic behavior of hypersonic vehicles. These models make it possible to generate continuous aerothermodynamic databases while drastically reducing both computational cost and time, and are therefore well suited for preliminary characterization.

The present work introduces a numerical tool developed in MATLAB that implements several reduced-order aerodynamic models and is capable of rapidly estimating the aerodynamic characteristics (CL, CD, CM, and E) of generic hypersonic geometries provided as input. Finally, the accuracy of the implemented models is assessed under different flight conditions through comparisons with inviscid and viscous CFD simulations, including cases with high-temperature effects modeled using a five-species non-equilibrium air model.

1.1 Thesis Outline

The thesis is organized as follows.

- **Chapter 2** introduces the main physical phenomena characterizing hypersonic flows and highlights the complexity of their aerothermodynamic behavior, as well as the significant computational cost associated with high-fidelity CFD analyses.
- **Chapter 3** presents the theoretical background of the reduced-order aerodynamic models adopted in this work, with particular focus on local surface inclination methods commonly used in hypersonic aerodynamics.
- **Chapter 4** describes the numerical framework developed in MATLAB, including the structure of the computational tool and the procedures used to process the input geometries and evaluate the aerodynamic coefficients. The chapter also introduces the fast console developed to automatically test different combinations of reduced-order models and rank the most suitable configurations for the analyzed geometry. Preliminary comparisons with inviscid CFD simulations over cone geometries are also presented.
- **Chapter 5** presents the application and validation of the proposed methodology through comparisons with high-fidelity CFD simulations over HB-2 and HGV configurations under different flow conditions, including viscous and chemically reacting cases.
- **Chapter 6** summarizes the main conclusions of the work and outlines possible directions for future developments.

Chapter 2

Hypersonic Flows

The term hypersonic typically refers to flows with Mach numbers exceeding 5 or 6, although this threshold is conventional rather than absolute. Instead of an abrupt transition in flow behavior at Mach 5, the hypersonic regime is distinguished by the increasing dominance of particular physical phenomena as velocity rises.
In the hypersonic regime, significant variations in temperature and density across the shock wave, combined with real-gas effects such as molecular dissociation, chemical reactions, ionization, and vibrational excitation, substantially affect the aerothermodynamic properties of the flow. These mechanisms alter the shock structure, aerodynamic performance, and thermal environment encountered by the vehicle.
Under these conditions, the bow shock forms in close proximity to the body surface, resulting in a thin shock layer with steep pressure and temperature gradients. The curvature of the shock wave produces entropy and vorticity layers that interact with the boundary layer, while elevated temperatures induce pronounced viscous and chemical effects. Consequently, the flow exhibits strong coupling, necessitating the simultaneous consideration of fluid dynamics, thermodynamics, and gas chemistry for accurate characterization.
This chapter summarizes some of the main physical and theoretical features of the hypersonic flow regime, which are discussed in greater detail by Anderson in Hypersonic and High-Temperature Gas Dynamics [1] and evidence the complexity associated with the hight fidelity CFD analysis.

2.1 Characteristic Phenomena of Hypersonic Flow

2.1.1 Shock Waves

In the analysis of compressible flows, when the Mach number, defined as the ratio between the flow velocity and the local speed of sound, is greater than one, the flow is said to be supersonic.
When, in this regime, the flow is deflected onto itself, for instance by a ramp, a dissipative, adiabatic and viscous phenomenon of infinitesimally small thickness known as a shock wave is generated.
If the local Reynolds number is sufficiently high, the flow can be separated into a viscous region and an inviscid region. In the latter case, due to the extremely small thickness of the shock, shock waves are treated as both mathematical and physical discontinuities.
Across these discontinuities, very large increases of the static flow properties such as pressure, temperature, density and entropy occur, and these increases tend to grow with increasing Mach number. On the other hand, a loss of total pressure is observed, which results in an increase of the so-called wave drag.
The magnitude of these variations is strongly related to the free–stream Mach number and to the flow deflection angle δ, which together determine the shape of the shock wave and the corresponding local shock angle β. In the case of two–dimensional shocks, these three quantities are related through the well–known θ–β–M relation

$$\tan\delta = 2\cot\beta\frac{M_\infty^2\sin^2\beta - 1}{M_\infty^2(\gamma + \cos 2\beta) + 2}$$

which can be represented graphically by the classical δ–β–M diagram shown in Fig. 2.1a.
Considering, as in Fig. 2.1b, a ramp with different deflection angles δ at fixed M_∞, the following shock configurations can be obtained:

- $\delta \leq \delta^*$: the shock remains attached to the ramp. In this regime the only physically realized solution is the weak-shock solution, for which the downstream flow remains supersonic ($M_2 > 1$) and becomes sonic when $\delta = \delta^*$.

- $\delta^* < \delta < \delta_{max}$: the downstream flow becomes subsonic behind the shock up to the sonic line, while the shock assumes a curved shape. In this regime the only admissible solution is the strong-shock solution, for which the downstream flow is subsonic ($M_2 < 1$).

- $\delta > \delta_{max}$: the shock is detached and a subsonic pocket forms in front of the body within the shock layer.

where δ_{max} is the maximum deflection angle, for a given Mach number, for which an attached shock can still exist, while δ^* represents the maximum deflection angle for which the downstream flow remains supersonic. In these configurations, it is possible to observe Prandtl–Meyer expansion waves interacting with the shock wave, modifying its curvature and strength. Expansions are isentropic processes that allow the flow to turn smoothly around a convex corner, leading to an increase in velocity and a decrease in static pressure through a Prandtl–Meyer fan originating at the corner and composed of an infinite number of Mach waves.

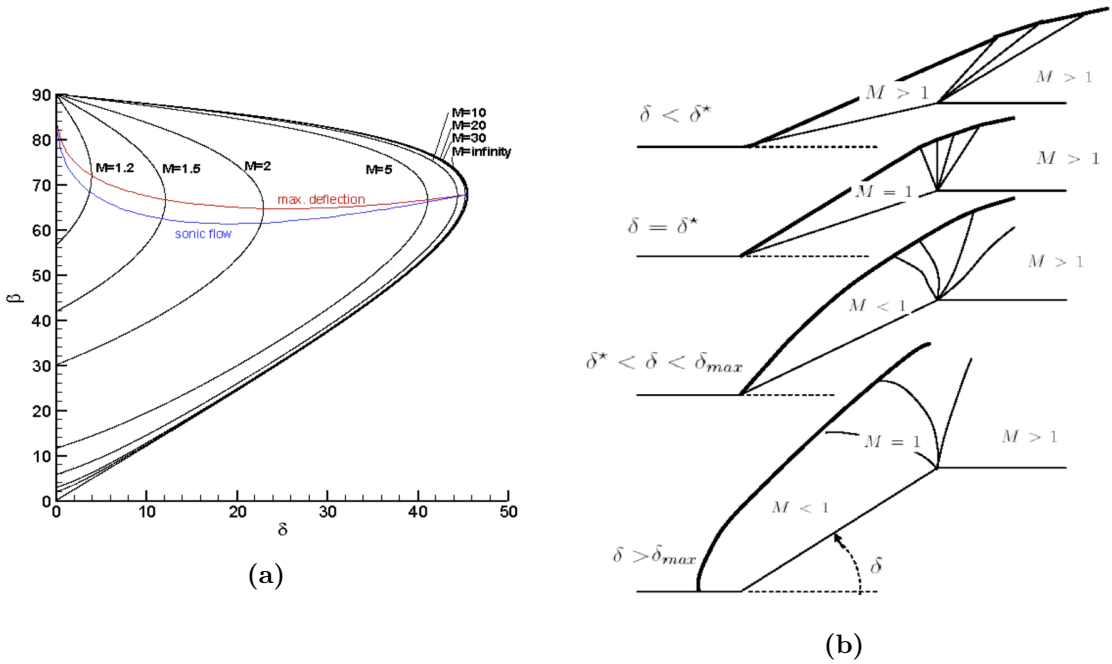

Figure 2.1: Shock-wave shapes. (a) δ–β–M diagram. (b) Shock shapes as a function of the ramp angle δ.

When the Mach number increases to the hypersonic regime, the shock and expansion relations remain the same as those governing supersonic flows, although they can be expressed in simplified forms in the limit as $M \to \infty$.
In any case, blunt-nose configurations, which are typical of hypersonic vehicles, always generate a detached bow shock with a subsonic pocket ahead of the body, corresponding to the strong-shock regime predicted by the θ–β–M diagram.

Conical Shock Waves

Compared with the ramp analysis presented previously, three–dimensional effects lead, for the same deflection angle, to a reduction of the shock angle.
This occurs because the presence of the third dimension creates a larger region

through which the flow can expand, so that a smaller shock angle is required to accommodate the same mass flow rate.
Nevertheless, as shown in Fig. 2.2a, a streamline initially undergoes a deflection that can be approximated by the classical oblique shock relations. Afterwards, the streamlines progressively adjust and tend to bend, approaching the body's surface asymptotically.
The conditions for attached, curved, or detached shocks are analogous to those of the ramp case and can be interpreted using the θ–β–M diagram characteristic of conical flows, shown in Fig. 2.2b.

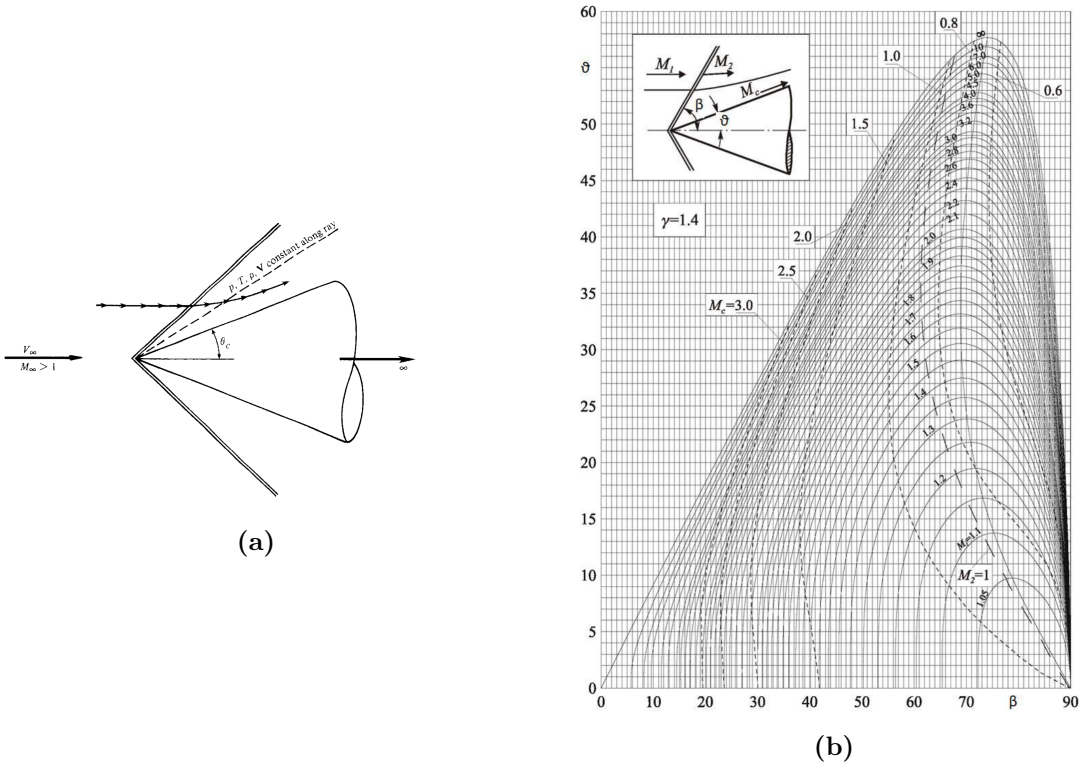

Figure 2.2: Conical shock-wave structure. (a) Conical shock and streamlines. (b) θ–β–M diagram for conical flows.

In this case, the conical shock solution is described by the Taylor–Maccoll ordinary differential equation, which does not admit a closed-form analytical solution and therefore must be solved numerically.
The numerical procedure is extensively discussed in the well-known book *Modern Compressible Flow* by J. Anderson [2] and has been implemented numerically in the MATLAB code developed by D. Joshi, reported in Appendix A.

2.1.2 Blunt-Body Problem

In order to avoid high concentrations of heat flux and to thermally protect the stagnation points and the surface of a body immersed in a hypersonic flow, blunt-nose configurations, characterized by a large radius of curvature, are generally adopted. The large radius of curvature, as shown in the previous section, leads to the formation of a strong detached shock wave in the most forward region of the nose, which becomes weaker moving away from the nose. This results in a shock layer characterized by two regions, a subsonic and a supersonic one, separated by the sonic line.
In the inviscid analysis of the shock layer, this represents a complication in the governing equations since the steady Euler equations are elliptic in the subsonic region and hyperbolic in the supersonic region, making them inadequate for accurately describing the entire flow field. The classical solution to this problem, still widely used, is based on a time-dependent finite-difference approach applied to the unsteady Euler equations, which are hyperbolic with respect to time. Starting from arbitrary initial conditions, the steady flow field is obtained iteratively as the asymptotic limit for large times. This method was developed by Moretti and Abbett and is suitable for all regions of the flow field.
A correct analysis of blunt bodies is essential to obtain accurate estimates of the pressure distribution and the resulting aerodynamic characteristics of the body. Consequently, even when reduced-order models are employed, it is important to take into account the fluid-dynamic properties typical of blunt-shaped configurations.

2.1.3 Thin Shock Layer

According to the oblique shock relations, for a given ramp angle δ, there is a progressive increase in density downstream of the shock wave as the Mach number increases. This compresses the flow into a smaller area called the thin shock layer, characterized by a shock significantly close to the body, as shown in Fig. 2.3.

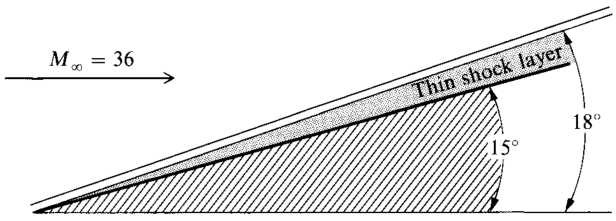

Figure 2.3: Thin Shock Layer visualization adapted from [1]

The impact angle reduction effect β is also amplified if dissociation effects are taken

into account.
At the extreme, for $M \to \infty$ and $\gamma \to 1$, the shock layer becomes infinitely dense and thin; the impact angle tends to the ramp angle, meaning that the shape of the body, the streamlines, and the impact become the same line. In this limit, the fluid dynamic field approaches the impact model postulated by Newton and described in detail in Chapter 3.

2.1.4 Entropy Layer

Another characteristic of hypersonic flows is the formation of an entropy layer that propagates from the nose of the body, enveloping its surface. This phenomenon is due to the different entropic states of the streamlines crossing the shock in regions of different intensity. Considering, for example, the blunt-nosed shape proposed in Fig. 2.4, it is possible to note how a streamline crossing the nose region, i.e., the region of strong shock, undergoes a significant increase in entropy, generating a strong gradient that propagates along the surface, unlike a streamline crossing a weak part of the shock.

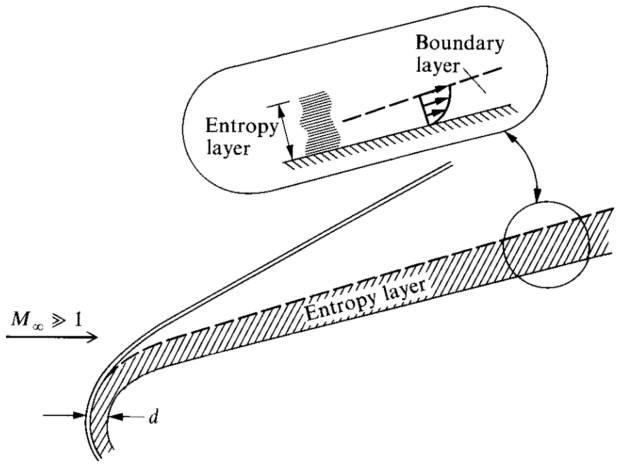

Figure 2.4: Entropy Layer over blunted nose configuration [1].

Consistent with Crocco's Theorem and the reduction of the stand-off distance as the Mach number increases, the strong entropy gradient corresponds to continuous vorticity production that interacts with the boundary-layer development, making it difficult to choose appropriate boundary conditions for a correct analysis.

2.1.5 Viscous Interaction

An important interaction phenomenon between the boundary layer and the external inviscid flow is the so-called viscous interaction. When a hypersonic flow slows due to viscous effects in the boundary layer, much of its kinetic energy is converted into the gas's internal energy, increasing the boundary-layer temperature. Since the pressure is constant in the direction normal to the wall and viscosity is related to temperature, according to the perfect gas law, an increase in temperature is followed by a decrease in gas density, resulting in a rapid increase in boundary layer thickness due to conservation of mass flow rate compared to flows at lower velocities.
Due to the thickening of the boundary layer and the high density within it, the body appears larger than it actually is to the external inviscid flow, generating a displacement effect and, consequently, modifying the external flow field, which in turn affects the boundary layer thickness.
The effects of this viscous interaction significantly affect the surface pressure distribution and, consequently, key aerodynamic characteristics such as lift, drag, and stability. In the most extreme cases, the shock can merge with the boundary layer, rendering the inviscid-shock-layer hypothesis ineffective and requiring alternative approaches to traditional boundary-layer methods.

2.1.6 High-Temperature Effects

The extreme viscous dissipation within hypersonic boundary layers generates a temperature increase that triggers dissociation and ionization phenomena, which invalidates the simplifying assumptions of a thermally and calorically perfect gas ($\gamma = 1.4$). In this case, we are talking about a chemically reactive boundary layer. Beginning at $800°K$, the vibrational degrees of freedom are excited, and the vibrational energy can no longer be described with classical thermodynamics but requires a more complex approach based on quantum physics. In this case, the specific heat ratio initially becomes a function of temperature and, with the onset of chemical reactions, dissociation and exchange, also of density ($\gamma = \frac{C_p}{C_v} = f(T, p)$). Above $9000°K$, furthermore, the chemically reactive gas begins to partially ionize (plasma), requiring a more complex treatment (models with 11 or more species). In this case, the ions dispersed in the gas can absorb electromagnetic radiation, leading to the communications blackout phenomenon.
Another complication arises from the inclusion of the chemical and vibrational non-equilibrium state.
The equilibrium state of a flow is analyzed by comparing the residence times of the particles in a certain region of the field t_{ref} with the characteristic times of the

thermochemical phenomenon t_t using the Damköhler number Da:

$$Da = \frac{t_{ref}}{t_c}, \quad \Rightarrow \quad \begin{cases} Da \to 0 & \text{Frozen Flow} \\ \text{Frozen Flow} < \text{Equilibrium Flow} < \text{Non-Equilibrium Flow} \\ Da \to \infty & \text{Non-Equilibrium Flow} \end{cases} \tag{2.1}$$

In hypersonic flow, the flow is in chemical nonequilibrium, as the particles do not have time to reach an equilibrium they never attain, making the flow's thermochemical characteristics dependent on the flow history and the catalytic properties of the wall.
The characteristic equations of chemical non-equilibrium, combined with the introduction of pyrolysis products arising from the potential use of ablative heat shields, become more complex, thereby increasing computational cost.
Chemically reactive flows at high temperatures also influence the pressure distribution and fundamental aerothermodynamic parameters, such as lift, drag, and heat fluxes, leading to deviations from analyses conducted without these considerations. In particular, surface heat fluxes are the most affected parameter, and in this flow regime, in addition to convective heat transfer by the boundary layer, radiative fluxes from the shock layer toward the surface become relevant.

2.1.7 Mach Number Independence Principle

The Mach number independence principle, originally formulated by Oswatitsch for the inviscid analysis of hypersonic flows, states that, when the Mach number of the undisturbed flow becomes sufficiently high, many dimensionless aerodynamic quantities tend to become weakly dependent on the exact value of M_∞.
In particular, aerodynamic quantities such as the pressure coefficient, lift, and wave-drag coefficients tend to progressively reach asymptotic values. At the same time, the low-field structure (such as shock wave shapes and Mach wave patterns) is independent of the Mach number.
This can be justified by introducing a dimensionless formulation of the Euler equations, using the properties of the undisturbed flow, such as density, velocity, and a characteristic length, as reference quantities. In this form, the equations of motion are expressed in terms of non-dimensional variables and do not explicitly contain the Mach number, which appears only in the boundary conditions associated with the shock wave.
This behavior has also been widely confirmed by experimental data, which show that, beyond a certain Mach number, the aerodynamic coefficients tend to reach a plateau; an example from Anderson [1] is shown in Fig.2.5.
The Oswatitsch principle, therefore, constitutes one of the theoretical foundations

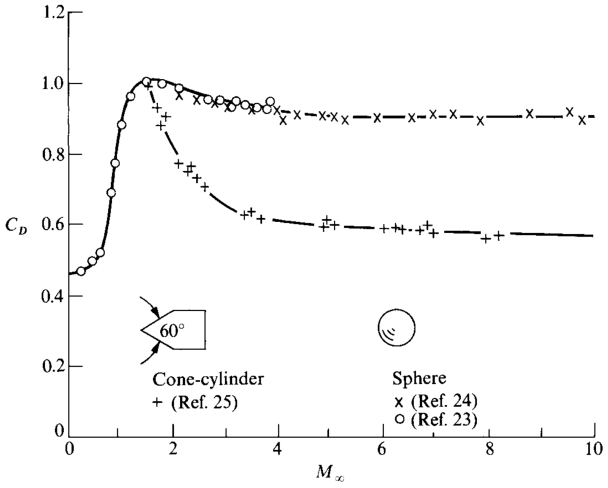

Figure 2.5: Drag coefficient for a sphere and a cone-cylinder from ballistic range measurements ,adapted from [1]

of hypersonic aerodynamics and justifies the use of simplified models, based on local surface inclination angles, to predict pressure distributions and aerodynamic performance in the very high Mach regime.

2.1.8 Free Molecular Flow and CFD limits

The numerical modelling of hypersonic flows is generally based on the continuum hypothesis, according to which the gas is treated as a continuous medium whose properties are defined at every point in space. Under this assumption, the governing equations of the flow are given by the compressible Navier–Stokes equations, which describe the conservation of mass, momentum, and energy.
The validity of the continuum assumption is typically evaluated through the Knudsen number, defined as the ratio between the molecular mean free path λ and a characteristic length scale L of the flow:

$$Kn = \frac{\lambda}{L} \tag{2.2}$$

For sufficiently small values of the Knudsen number ($Kn < 0.2$), the flow can be accurately described using continuum fluid mechanics. In this regime, Computational Fluid Dynamics (CFD) solvers based on the Navier–Stokes equations represent the most accurate tool for predicting the aerothermodynamic behaviour of hypersonic flows.
However, as altitude increases, air density decreases, thereby increasing the mean free path and reducing the validity of the continuum-hypothesis-based approaches.

The first impact on the equations occurs for $0.03 < Kn < 0.2$, where, in the low-density regime, slip conditions arise for the velocity and temperature at the surface, and the no-slip condition cannot be applied. In this case, the wall flow velocity is nonzero, while the temperature no longer coincides with the wall temperature.
As the Knudsen number (Kn) increases, after a transitory period, the free-molecular flow regime (Kn close to 1) is reached, where the classic CFD approach is no longer valid and approaches based on kinetic theory, such as Direct Simulation Monte Carlo (DSMC), must be used. This limits the applicability of CFD analysis based on the Navier-Stokes equations for high-altitude analysis of various hypersonic aircraft, particularly for "relatively small" configurations, where the body's small characteristic dimension L already anticipates this limitation at lower altitudes. On the other hand, it is unclear whether different ROMs have limits on applicability and accuracy as a function of altitude, but rapid, ad hoc models exist for the free-molecular flow regime.

Final Remarks The physical phenomena discussed in this chapter highlight the strong coupling between fluid dynamics, thermodynamics, and gas chemistry that characterizes hypersonic flows and makes high-fidelity CFD simulations computationally expensive and complex.
Although viscous and real-gas effects can significantly influence the detailed pressure distribution and surface heat fluxes, the global aerodynamic forces are largely governed by pressure loads generated by the shock layer.
These considerations motivate the use of reduced-order models based on local surface inclination methods, which provide an efficient tool for the rapid preliminary aerodynamic analysis of hypersonic configurations and whose formulation is presented in the following chapter.

Chapter 3

Reduced Order Models (ROMs)

3.1 Local Surface Inclination Methods

The local surface inclination methods provide a means for estimating the surface pressure distribution over hypersonic bodies in order to determine the aerodynamic forces and their decomposition into lift, drag, and momentum components.
In these methods, the body surface is discretized into a finite number of triangular or quadrilateral elements. For each panel, the local pressure coefficient is evaluated as a function of the inclination angle between the surface tangent and the free-stream direction.
The primary advantage of these methods is their low computational cost, which enables rapid aerodynamic evaluations. However, this simplification reduces accuracy and limits their use in modern practice to preliminary design stages and early verification activities.
Before the advent of computational fluid dynamics (CFD), local inclination methods were the only practical tools for predicting hypersonic aerodynamic characteristics. They were extensively used in the design of the first hypersonic vehicles during the 1950s.
Beginning in the 1970s, these methods were implemented in computer programs such as the *Hypersonic Arbitrary Body Program (HABP)*, developed by Gentry et al. [3] at the Douglas Aircraft Company in 1964, which includes the estimation of surface pressure, aerodynamic forces and moments, skin friction, and heat transfer over arbitrary body shapes.
Subsequent improvements were made in the *Aerodynamic Preliminary Analysis System (APAS)* [4] in the late 1980s and, more recently, in the *Supersonic Hypersonic Arbitrary Body Program (SHABP)* [5], which computes aerodynamic coefficients for

arbitrary geometries over a wide Mach range, including transitional flow regimes. Last but not least, CBAERO, developed by Kinney at the NASA Ames Research Center [5], incorporates real-gas effects and both radiative and convective heat transfer.
This section presents a selection of reduced-order models employed in the numerical tools presented above for the inviscid treatment of hypersonic flow regimes.
These models are implemented in the MATLAB code presented in Chapter 4 and are summarized in Table 3.1.

Impact Flow – Windward Side	**Shadow Flow – Leeward Side**
1. Newtonian	1. Newtonian ($C_p = 0$)
2. Modified Newtonian	2. Modified Newtonian + Prandtl–Meyer
3. Modified Newtonian + Prandtl–Meyer	3. OSU empirical
4. Tangent Wedge	4. Van Dyke Unified
5. Tangent Wedge Empirical	5. Prandtl–Meyer from free stream
6. Tangent Cone	6. High-Mach base pressure
7. Tangent Cone Empirical	7. Shock Expansion
8. Inclinated Cone	
9. Delta Wing Empirical	
10. OSU Empirical	
11. Hankey Empirical	
12. Dahlem–Buck Empirical	
13. Van Dyke Unified	
14. Shock Expansion	

Table 3.1: Local surface inclination methods for impact and shadow flow regions

3.1.1 Newtonian Flows

In 1687, in the *Philosophiae Naturalis Principia Mathematica*, Isaac Newton presented a simplified model for estimating the pressure exerted by a fluid on an inclined surface.
The model treats the flow as a stream of non-interacting particles that strike the surface. After impact, each particle is redirected tangentially along the plane, generating a force that acts only in the normal direction of the wall. An example is illustrated in Fig 3.1.

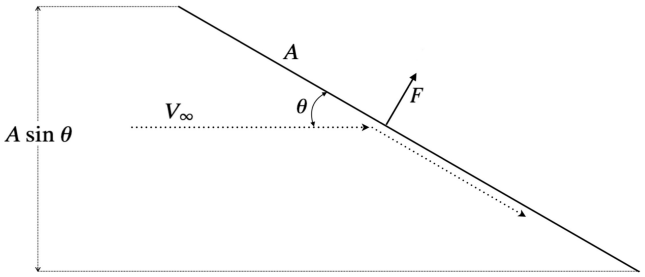

Figure 3.1: Schematic representation of the Newtonian model.

From the second law of dynamics, the force F is defined as the time rate of change of the mass flux, which can be expressed as the difference between the pressure and the free stream static pressure, multiplied by the impact area A:

$$F = (\rho_\infty V_\infty A sin(\theta))(V_\infty sin(\theta)) = A(p - p_\infty) \tag{3.1}$$

which, starting from the pressure-coefficient formulation, can be rewritten as:

$$C_p = \frac{p - p_\infty}{\frac{1}{2}\rho_\infty V_\infty^2} = 2sin^2(\theta) \tag{3.2}$$

where V_∞ and θ represent respectively the velocity vector of the free stream and the local angle between the surface tangent and the free stream direction.
This simplified expression, known as the *sine-square law* (3.2), is inaccurate for low-speed applications. However, it becomes rigorous in the analysis of high-speed hypersonic flows, in accordance with the Mach-number independence principle. It enables an approximate estimation of aerodynamic forces based only on the local angle θ without the need to know any other flow parameters or quantities.
The use of Newton's law for hypersonic applications can be justified, as proposed by Anderson [1], through the analogy between the Newtonian flow model and the phenomenology of the oblique shock wave illustrated in Fig. 3.2:

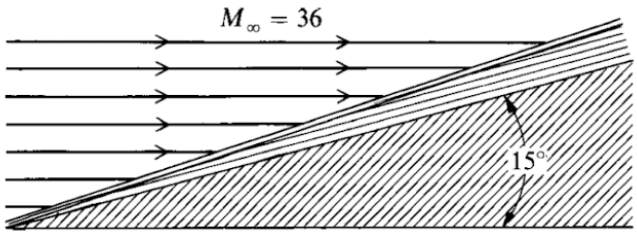

Figure 3.2: Oblique-shock structure adapted from Anderson [1].

In this representative case, a 15° wedge in a Mach 36 stream creates an oblique shock that deflects the flow, making it almost parallel to the surface while the shock comes very close to the body, as predicted by thin shock layer theory. From a distance perspective, the flowfield looks similar to the Newtonian model, providing a macroscopic analogy.
Within this framework, Eq. (3.2) provides the local evaluation of the pressure coefficient Cp at a generic point P on a two-dimensional body, as illustrated in Fig. 3.3a. This relation can be generalised to an arbitrary three-dimensional configuration (Fig. 3.3b) by introducing the local normal vector $\vec{n}$ and the angle ϕ_2 between the free stream direction and $\vec{n}$, as follows:

$$\begin{cases} \theta = \phi_2 - \frac{\pi}{2} = \frac{\pi}{2} - \phi_1 \\ \frac{\vec{V_\infty}}{|V_\infty|} \cdot \vec{n} = cos(\phi_2) = -sin(\theta) \\ C_p = 2sin^2(\theta) \end{cases} \Rightarrow C_p = 2sin^2(\frac{\pi}{2} - \phi_1) = 2\left(\frac{\vec{V_\infty}}{|V_\infty|} \cdot \vec{n}\right)^2 \quad (3.3)$$

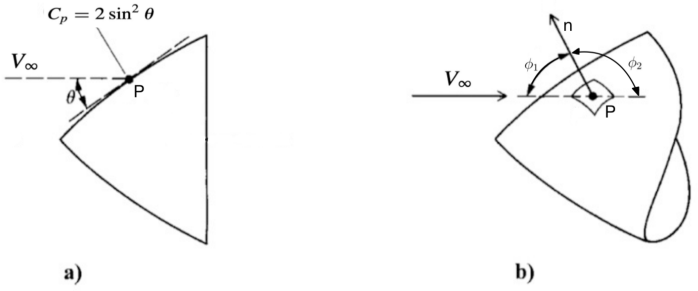

Figure 3.3: Newtonian flow schematic: a) two-dimensional body, b) three-dimensional body.

In this context, it is important to distinguish the flow-exposed region from the **Shadow Region**. Newtonian theory accounts only for surface elements directly impacted by incoming flow particles, while those shielded from the flow don't receive any momentum transfer. Consequently, the pressure coefficient within the shadow

region is conventionally set to zero. Fig. 3.4 illustrates this behavior, showing that only elements satisfying $\vec{V_\infty} \cdot \vec{n} < 0$ contribute to the aerodynamic load.

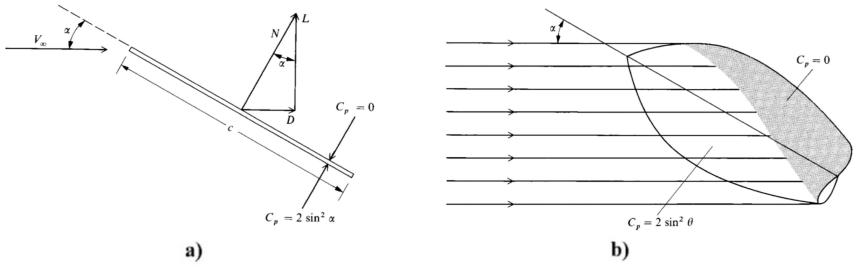

Figure 3.4: Shadow Region adapted from [1]: a) two-dimensional body, b) three-dimensional body.

$\vec{N}$[1] represents the resultant aerodynamic force acting on the surface element, and it can be decomposed into lift $\vec{L}$ and drag $\vec{D}$ components as shown in Fig. 3.4a.

3.1.2 Modified Newtonian Law

A more accurate and refined version of the Newtonian model was developed by Lester Lees to predict the pressure distribution over blunted body configurations. The formulation is expressed in the *Modified Newtonian Law*:

$$C_p = C_{p,max} sin^2(\theta) \tag{3.4}$$

where $C_{p,max}$ denotes the maximum pressure coefficient at the stagnation point downstream of a normal shock wave. This quantity can be determined from the exact normal shock relations as follows:

$$\begin{cases} C_{p,max} = \frac{p_2^0 - p_\infty}{0.5\rho_\infty V_\infty^2} \\ 0.5\rho_\infty V_\infty^2 = 0.5\gamma p_\infty M_\infty^2 \\ \frac{p_2^0}{p_\infty} = [\frac{(\gamma+1)^2 M_\infty^2}{4\gamma M_\infty^2 - 2(\gamma-1)}]^{\frac{\gamma}{\gamma-1}} [\frac{1-\gamma+2\gamma M_\infty^2}{\gamma+1}] \end{cases} \Rightarrow C_{p,max} = \frac{2}{\gamma M_\infty^2} \left[\frac{p_2^0}{p_\infty} - 1 \right] \tag{3.5}$$

where p_2^0 is the stagnation pressure downstream of the shock wave.
As expressed in Eq. (3.5), the pressure coefficient evaluated over a surface element is no longer independent of the Mach number. Instead, it incorporates the ratio of specific heats, γ, which, in the hypersonic regime, is no longer constant but varies

[1]The resultant force is always perpendicular to the flat plate, since the flow is treated as inviscid and the only stresses acting on the surface are the pressure forces, which are normal to the plate.

with temperature.
The modified Newtonian law can be reduced to the sine-square law (3.2) only in the limit in which $M \to \infty$ and $\gamma \to 1$ where $C_{p,max} \to 2$. However, its dependence on the two flow variables, derived from the exact normal–shock theory, suggests more accurate predictions.

3.1.3 Modified Newtonian + Prandtl-Meyer

Another improvement to the modified Newtonian mode was proposed by Kaufman for the analysis of detached shock waves over blunt bodies and subsequently incorporated into the formulation reported in the Gentry code[3].
This method combines the modified Newtonian method in the compression region with Prandtl-Meyer expansion theory in the expansion region. The former is located downstream of the detached bow shock and includes the subsonic flow, while the latter represents the supersonic one.
To distinguish the subsonic–supersonic transition, a matching point is identified along the body surface with the slope δ_q .
For this method, as well as for the subsequent local inclination approaches discussed in this work, the surface inclination angle with respect to the free-stream direction is evaluated from the x-component of the outward surface normal vector, under the assumption that the free-stream velocity vector $\vec{V}_\infty$ is aligned with the x-axis of the reference frame, as detailed in the following:

$$\delta = \frac{\pi}{2} - \arccos(-n_x) \tag{3.6}$$

The procedure used to determine the matching point between the compression and expansion regions is outlined below:

1. Assume the interval of the matching Mach numbers $M_q = [1.35,1.7]$ for $\gamma = 1.4$;

2. Evaluate both functions in the interval defined by the two matching Mach numbers, and determine the matching-point Mach number[2] by solving $P_c(M_q) = 0$ for M_q within this interval:

$$Q = \frac{P_q}{P_0} = \left[\frac{2}{2+(\gamma-1)M_q^2}\right]^{\frac{\gamma}{\gamma-1}}, \quad P_c = Q\left[1 - \frac{\gamma^2 M_q^4 Q}{4(M_q^2-1)(1-Q)}\right] \tag{3.7}$$

   respectively the free-stream static pressure ratio and the free-stream static to stagnation pressure rateo;

[2]The Mach number at the matching point corresponds to the Mach number at the onset of the expansion region.

3. Evaluate the functions Q and P_c at the Mach number corresponding to the matching point M_q;

4. The surface inclination angle δ_q is evaluated at the matching point, defining the surface slope that separates the compression and expansion regions as $sin(\delta_q)^2 = \frac{Q-P}{1-P}$;

5. Use the Prandtl-Meyer expansion theory below to find the Mach number on the surface element M_δ:

$$\begin{cases} \nu(M) = \sqrt{\dfrac{\gamma+1}{\gamma-1}}\arctan\left(\sqrt{\dfrac{\gamma-1}{\gamma+1}\left(M^2-1\right)}\right) - \arctan\left(\sqrt{M^2-1}\right) \\ \delta_i = \delta - \delta_q \\ \nu(M_\delta, \gamma) = \nu(M_q, \gamma) + |\delta_i| \end{cases} \tag{3.8}$$

6. Calculate the surface pressure ratio: $\frac{P_\delta}{P_0} = \eta_c[1 + 0.5(\gamma-1)M_\delta]^{-\frac{\gamma}{\gamma-1}}$ where η_c is as an empirical correction factor supposed to be 1 and P_δ is the pressure on the element of interest;

7. Calculate the element pressure coefficent Cp_δ as:

$$\begin{cases} C_{p,\delta} = \dfrac{2}{\gamma M_\infty^2}\left(\dfrac{P_\delta}{P_0}\dfrac{P_0}{p_\infty} - 1\right) & \delta_i > 0 \\ C_{p,\delta} = C_{p,\max}\,\sin^2\delta & \delta_i \leq 0 \end{cases} \tag{3.9}$$

Compared to classical Newtonian approaches, this method, by incorporating Prandtl-Meyer expansion theory, provides a more realistic representation of the flow in the expansion region and enables the evaluation of surface pressure on elements located in the shadow region.

3.1.4 Tangent Wedge

The tangent-wedge method is a local surface inclination technique suitable for two-dimensional hypersonic configurations. The method is valid if the local surface inclination angle is smaller than the maximum allowable flow deflection angle $\delta_{\max}(M_\infty)$ corresponding to an attached oblique shock at the freestream Mach number.
Each surface element is locally approximated by an equivalent wedge with half-angle $\delta_i = \theta_i$, where θ_i is the local inclination angle of the surface with respect to the freestream direction, as shown in Fig. 3.5.

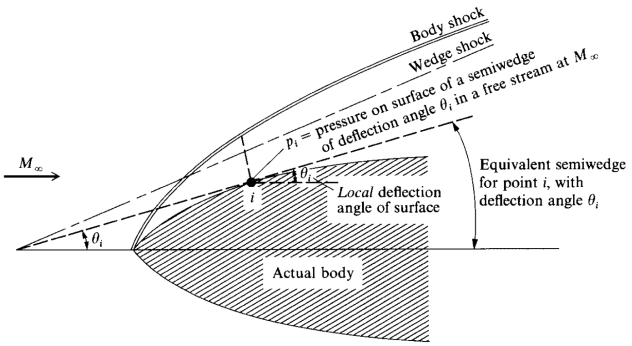

Figure 3.5: Schematic representation of the Tangent Wedge Method adapted from [1].

The main assumption of the method is that the pressure acting on the surface element is equal to the pressure on the surface of the equivalent wedge immersed in a uniform freestream at Mach number M_∞. For surface compression elements ($\delta_i > 0$), the local pressure p_i is obtained by solving the exact oblique shock relations for a deflection angle δ_i and freestream Mach number M_∞. In particular, the shock angle β_i is determined from the θ–β–M relation:

$$\tan \delta_i = 2 \cot \beta_i \frac{M_\infty^2 \sin^2 \beta_i - 1}{M_\infty^2 \left(\gamma + \cos 2\beta_i\right) + 2}, \tag{3.10}$$

Once the shock angle is known, the post-shock pressure p_i is computed using the oblique shock pressure ratio

$$\frac{p_i}{p_\infty} = 1 + \frac{2\gamma}{\gamma + 1} \left(M_\infty^2 \sin^2 \beta_i - 1\right), \tag{3.11}$$

from which the local pressure coefficient follows as

$$C_{p,\text{wedge}}(i) = \frac{2}{\gamma M_\infty^2} \left[\left(\frac{p_i}{p_\infty} \right)_i - 1 \right], \tag{3.12}$$

The Tangent - Wedge method is generally suitable for slender body configurations with attached shock waves, even if it is not derived from a rigorous theoretical flow model, such as Newtonian theory.
The applicability of this method is also limited to exposed regions where the shock remains attached. In particular, when $\delta_i > \delta_{\max}(M_\infty)$), the method becomes invalid, and alternative approaches, such as modified Newtonian theory, are necessary.

Tangent-Wedge, Tangent-Cone and Delta-Wing Empirical Methods

A faster empirical version of the tangent-wedge and tangent-cone methods, implemented in the Gentry code, is formulated through simplified shock relations suitable for rapid engineering calculations. The shock angle θ_s is related to the local wedge or cone deflection, respectively δ_w and δ_c, under the thin shock-layer assumption by

$$\begin{cases} \sin\theta_s = \dfrac{\sin\delta_w}{(1-\epsilon)\cos(\theta_s-\delta_w)} & \text{(wedge)} \\ \sin\theta_s = \dfrac{\sin\delta_c}{\left(1-\frac{\epsilon}{2}\right)\cos(\theta_s-\delta_c)} & \text{(cone)} \end{cases} \qquad \epsilon = \frac{\rho_1}{\rho_2} = \frac{\gamma-1}{\gamma+1}\left[1+\frac{2}{(\gamma-1)M_{ns}^2}\right]. \tag{3.13}$$

In the hypersonic limit, as $M_\infty \to \infty$, the parameter ϵ approaches the asymptotic value $\epsilon_{\lim} = \frac{\gamma-1}{\gamma+1}$ and the shock-angle relation reduces to

$$\begin{cases} \sin\theta_s = \dfrac{\gamma+1}{2}\,\sin\delta_w & \text{(wedge)} \\ \sin\theta_s = \dfrac{2(\gamma+1)}{\gamma+3}\,\sin\delta_c & \text{(cone)} \end{cases} \tag{3.14}$$

The exact shock relations formally depend on three variables, θ_s, δ_w or δ_c, and ϵ, but it is observed that for constant γ, the parameter ϵ depends only on the normal-shock Mach number M_{ns}. As a consequence, the governing relations may be rewritten in terms of only the two variables M_{ns} and $M_\infty \sin\delta$, yielding

$$\begin{cases} M_{ns} = \dfrac{M_\infty \sin\delta_w}{(1-\epsilon)\cos(\theta_s-\delta_w)} & \text{(wedge)} \\ M_{ns} = \dfrac{M_\infty \sin\delta_c}{\left(1-\frac{\epsilon}{2}\right)\cos(\theta_s-\delta_c)} & \text{(cone)} \end{cases} \tag{3.15}$$

where $(\theta_s - \delta)$ [3] is considered approximately constant and independent from the free stream Mach number except near the shock detachment.
Under this hypothesis, the normal Mach number behind the shock can be expressed as a function of the reduced Mach number

$$M' = M_\infty \sin\delta, \tag{3.16}$$

where δ denotes the local surface inclination angle.
The empirical formulation is constructed to satisfy the following requirements:

[3] Here δ denotes either δ_w or δ_c.

- shock detachment effects are neglected;
- $M_{ns} = 1$ for $M' = 0$;
- the solution asymptotically approaches the $M = \infty$ line;
- have the correct slope: $\frac{dM_{ns}}{dM_\infty sin(\delta)}$ at $M_\infty sin(\delta) = 0$.

These constraints lead to the empirical expression

$$\begin{cases} M_{ns} = K_w M' + e^{-\frac{K_w}{2}M'}, & K_w = \dfrac{\gamma+1}{2} \quad \text{(wedge)} \\ M_{ns} = K_c M' + e^{-K_c M'}, & K_c = 2\,\dfrac{\gamma+1}{\gamma+3} \quad \text{(cone)} \end{cases} \tag{3.17}$$

Once the normal Mach number behind the shock is determined, the pressure coefficient on the wedge or cone surface is computed as

$$\begin{cases} C_p = \dfrac{4}{\gamma+1}\dfrac{M_{ns}^2-1}{M_\infty^2} & \text{(wedge)} \\ C_p = 2\sin^2(\delta_c)\left[1 - \dfrac{(\gamma-1)M_{ns}^2+2}{4(\gamma+1)M_{ns}^2}\right] & \text{(cone)} \end{cases} \tag{3.18}$$

An analogous formulation will subsequently be adopted for the empirical delta-wing method, under the same underlying assumptions, combining the expressions discussed above.
According to experimental tests, the pressure distribution along the centerline of a delta wing is evaluated using the two-dimensiona wedge theory for low similarity parameters ($M' \lesssim 3$), while the conical flow theory is used for larger ones. The resulting relationships are given below.

$$\begin{cases} M_{ns} = K_c M' + e^{-(K_c - \frac{K_w}{2})M'} \\ C_p = \left(\dfrac{4}{\gamma+1}(M_{ns}^2-1)\right)\dfrac{1}{M_\infty^2}. \end{cases} \qquad \text{(Delta - Wing)} \tag{3.19}$$

3.1.5 Tangent Cone

The tangent-cone method is a local surface inclination technique applicable to axisymmetric and three-dimensional hypersonic configurations. The method is valid provided that the local surface inclination angle is smaller than the maximum allowable flow deflection angle $\delta_{\max}(M_\infty)$ corresponding to an attached conical

shock at the freestream Mach number.
Each surface element is locally approximated by an equivalent cone with half-angle $\delta_i = \theta_i$, where θ_i is the local inclination angle of the surface with respect to the freestream direction, as shown in Fig. 3.6. The fundamental assumption of the method is that the pressure acting on the surface element is equal to the pressure on the surface of the equivalent cone immersed in a uniform freestream at Mach number M_∞, as determined from conical flow theory.

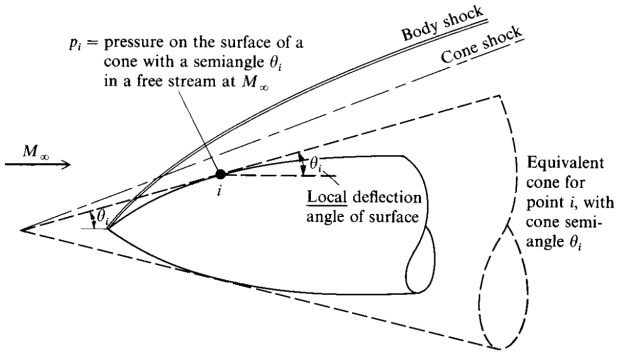

Figure 3.6: Schematic representation of the Tangent Cone Method from [1].

The local pressure p_i is obtained, for compression surface elements ($\delta_i > 0$), by solving the Taylor-Maccoll equation over a cone.
In particular, this equation provides the flowfield variation between the conical shock and the cone surface, giving an evaluation of the surface elements' Mach numbers M_c for a given freestream Mach number M_∞ and cone half-angle δ_i.
Once M_c is obtained, the wall pressure is computed assuming isentropic flow between the post-shock region and the cone surface, while the total pressure loss across the conical shock and the pressure recovery from the post-shock state to the wall are evaluated, respectively, using oblique-shock and isentropic relations as follows:

$$\begin{cases} \dfrac{p_c}{p_{02}} = \left(1 + \dfrac{\gamma-1}{2} M_c^2\right)^{-\frac{\gamma}{\gamma-1}}, & \text{(isentropic flow from region 2 to the wall)} \\ \dfrac{p_2}{p_1} = 1 + \dfrac{2\gamma}{\gamma+1}\left(M_{n1}^2 - 1\right), & \text{(oblique shock pressure ratio)} \\ \dfrac{p_{02}}{p_2} = \left(1 + \dfrac{\gamma-1}{2} M_2^2\right)^{\frac{\gamma}{\gamma-1}}, & \text{(total pressure ratio in region 2)} \end{cases} \tag{3.20}$$

The resulting pressure ratio between thecone surface and the freestream is given by

$$\frac{p_c}{p_\infty} = \left(\frac{p_{02}}{p_2}\right)\left(\frac{p_2}{p_\infty}\right)\left(\frac{p_c}{p_{02}}\right), \tag{3.21}$$

where subscripts 2 and c denote the post-shock and wall conditions, respectively and $M_{n1} = M_\infty sin(\beta)$.
Finally, the local pressure coefficient for the tangent-cone method is evaluated as

$$C_p = \frac{2}{\gamma M_\infty^2}\left[\left(\frac{p_c}{p_\infty}\right) - 1\right]. \tag{3.22}$$

As in the tangent-wedge approach, the pressure coefficient C_p is corrected using the modified Newtonian method in regions where the shock becomes detached, that is, when the local flow deflection angle exceeds the maximum value associated with an attached shock.

Inclined Cone

The inclined cone method, implemented in the Gentry code, is based on the CP-792 approach proposed by the British Hypersonic Research for evaluating the pressure distribution over cones inclined at angles of attack α.
This method follows an impact-type relation but computes the local pressure coefficient as a function of the cone half-angle θ, the angle of attack α, and the circumferential angle ϕ, measured from the most windward generator, as follows:

$$C_p = C_{pA} + C_{pN} + C_{pX}, \tag{3.23}$$

with

$$C_{pA} = K \sin^2\theta \cos^2\alpha, \tag{3.24}$$
$$C_{pN} = K \cos^2\theta \sin^2\alpha \cos^2\phi, \tag{3.25}$$
$$C_{pX} = 2K \sin\theta \cos\theta \sin\alpha \cos\alpha \cos\phi. \tag{3.26}$$

where C_{pA} is the contribution associated with the axial component of the freestream velocity, C_{pN} arises from the transverse component induced by the angle of attack, and C_{pX} represents a cross-term that accounts for the interaction between axial and normal flow components.
In this work, the cone half-angle and circumferential angle are determined from the surface geometry, and the impact coefficient K is set equal to the maximum pressure coefficient $C_{p,\max}$. The pressure coefficient is calculated exclusively for windward surface elements, while it is set to zero for leeward ones according to the impact theory.

3.1.6 Shock - Expansion

The shock-expansion method is an approximate technique applicable to slender, sharp-nosed bodies, for which the shock wave at the leading edge remains attached. The method assumes that, at the leading edge, a positive local flow deflection produces an attached oblique shock, while a negative one follows the Prandtl-Meyer expansion from the freestream, as illustrated in Figure 3.7.

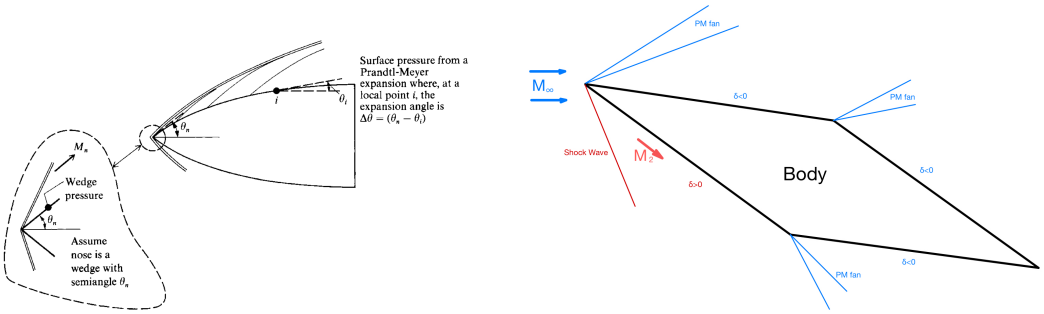

Figure 3.7: Schematic representation of the Shock-Expansion Method.

Once the phenomenon at the leading edge is determined, the flow is treated over the body surface as an isentropic expansion. As a consequence, the Mach number on the surface element i, M_i, is obtained following the Prandtl-Meyer relation:

$$\nu(M_i) = \nu(M_{\text{ref}}) + \delta_i, \tag{3.27}$$

where M_{ref} coincides with the freestream Mach number in the case of a pure expansion, or with the post-shock Mach number M_2 when an attached oblique shock is present at the leading edge.
Then, assuming that the downstream expansion is locally two-dimensional, the pressure ratio between the local state and the freestream can be computed as

$$\frac{p_i}{p_\infty} = \left(\frac{1 + \frac{\gamma-1}{2} M_i^2}{1 + \frac{\gamma-1}{2} M_\infty^2} \right)^{-\frac{\gamma}{\gamma-1}}. \tag{3.28}$$

The corresponding pressure coefficient follows as

$$C_p(i) = \frac{2}{\gamma M_\infty^2} \left[\left(\frac{p_i}{p_\infty} \right) - 1 \right]. \tag{3.29}$$

In accordance with Anderson's treat, reflection effects are neglected in the present formulation, and that is because the expansion waves reflected by the oblique shock propagate away from the body and therefore do not interact with the near-wall

flow field.
This assumption significantly improves the accuracy of the shock-expansion method in hypersonic conditions, making it more suitable for hypersonic flows than for supersonic ones, as shown in Fig. 3.8.

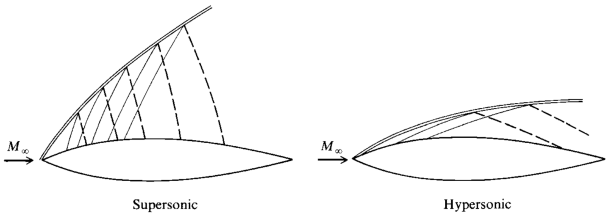

Figure 3.8: Schematic representation of expansion wave reflection from [1]

The validity of the method is therefore restricted when that shock detachment does not occur. When this condition is violated, the method loses physical significance and must be replaced by alternative approaches more suitable for blunt bodies.

3.1.7 Prandtl - Meyer from Free-Stream

The Prandtl-Meyer from free-stream approach is employed to model the leeward (shadow) regions, where the local surface deflection angle is negative ($\delta_i < 0$) and the flow is assumed to undergo an isentropic expansion starting directly from the freestream Mach number M_∞. Under this assumption, the local Mach number is obtained by applying the Prandtl-Meyer function

$$\nu(M) = \sqrt{\frac{\gamma+1}{\gamma-1}}\arctan\left(\sqrt{\frac{\gamma-1}{\gamma+1}\left(M^2-1\right)}\right) - \arctan\left(\sqrt{M^2-1}\right), \tag{3.30}$$

so that the target Prandtl-Meyer angle at the i-th surface element is

$$\nu(M_i) = \nu(M_\infty) + |\delta_i|. \tag{3.31}$$

Since the Prandtl-Meyer function admits an upper bound as $M \to \infty$,

$$\nu_{\max} = \frac{\pi}{2}\left(\sqrt{\frac{\gamma+1}{\gamma-1}} - 1\right), \tag{3.32}$$

the maximum physically admissible expansion starting from the freestream is

$$|\delta|_{\max} = \nu_{\max} - \nu(M_\infty). \tag{3.33}$$

If $|\delta_i| \geq |\delta|_{\max}$, the expansion is saturated to the vacuum limit ($p_i \to 0$), which corresponds to the minimum achievable pressure coefficient

$$C_{p,\min} = -\frac{2}{\gamma M_\infty^2}. \tag{3.34}$$

For admissible expansions ($|\delta_i| < |\delta|_{\max}$), the local Mach number M_i is obtained by inverting the Prandtl-Meyer relation. The corresponding static pressure ratio follows from isentropic relations is:

$$\frac{p_i}{p_\infty} = \left(\frac{1 + \frac{\gamma-1}{2} M_i^2}{1 + \frac{\gamma-1}{2} M_\infty^2} \right)^{-\frac{\gamma}{\gamma-1}}, \tag{3.35}$$

and the local pressure coefficient is finally computed as

$$C_p(i) = \frac{2}{\gamma M_\infty^2} \left[\left(\frac{p_i}{p_\infty} \right) - 1 \right]. \tag{3.36}$$

In the current implementation, the Prandtl-Meyer free-stream correction is applied exclusively to panels classified as leeward based on the geometric shadow criterion. For windward panels, $C_p$is set to zero.

3.1.8 Hankey Flat-Surface Empirical

The Hankey flat-surface empirical method is based on another empirical correlation included in the Gentry code developed to estimate surface pressure distributions on blunted flat plates. At small impact angles, the formulation reproduces the behavior of the tangent-wedge approach, while for larger impact angles it approaches the Newtonian impact method.
The pressure coefficient is expressed as

$$C_p = 1.95 \sin^2 \delta + 0.21 \cos \delta \, \sin \delta, \tag{3.37}$$

where δ denotes the local flow deflection angle.

3.1.9 OSU Blunt Body Empirical

An additional empirical approach implemented for blunt configurations proposed by Gentry is the OSU (Ohio State University) blunt-body method. This formulation was originally developed to describe the pressure distribution around circular cylinders in supersonic flow. The method provides an empirical relation for the surface pressure expressed as

$$\frac{p_1}{p_{t\infty}} = 0.32 + 0.455 \cos\theta + 0.195 \cos(2\theta) + 0.035 \cos(3\theta) - 0.005 \cos(4\theta), \tag{3.38}$$

where θ denotes the peripheral angle measured from the stagnation point ($\theta = 0$ at stagnation), p_1 is the local surface pressure, and $p_{t\infty}$ is the total pressure rise through normal shock.
The local pressure coefficient is then obtained from the definition

$$C_p = \frac{2}{\gamma M_\infty^2}\left[\left(\frac{p_1}{p_{t\infty}}\right)\left(\frac{p_{t\infty}}{p_\infty}\right) - 1\right], \tag{3.39}$$

where the total-to-static pressure ratio across a normal shock is approximated as

$$\frac{p_{t\infty}}{p_\infty} = 1 + \frac{\gamma K M_\infty^2}{2}. \tag{3.40}$$

Here K denotes the stagnation pressure coefficient $C_{p,\max}$.

3.1.10 Dahlem-Buck Empirical

The Dahlem-Buck method is an empirical formulation that approximates tangent-cone pressures at low impact angles and Newtonian impact theory at larger deflections.
The original Dahlem-Buck formulation expresses the pressure coefficient for windward surface elements as a function of the local impact angle δ as

$$C_{p,\mathrm{DB}} = \begin{cases} \left[\dfrac{1.0}{\sin^{3/4}(4\delta)} + 1.0\right]\sin^2\delta, & \delta \le 22.5^\circ, \\ 2\sin^2\delta, & \delta > 22.5^\circ, \end{cases} \tag{3.41}$$

The original Dahlem-Buck formulation has been shown to provide good agreement for highly swept configurations at large hypersonic Mach numbers.

Modified Dahlem-Buck

The modified Dahlem-Buck method extends the original formulation to lower Mach number regimes by introducing a Mach-dependent correction where the pressure coefficient is obtained by scaling the original Dahlem-Buck coefficient in the following way:

$$C_{p,\mathrm{MDB}} = C_{p,\mathrm{DB}}\frac{C_{p,\mathrm{cone}}(M_\infty < 20)}{C_{p,\mathrm{cone}}(M_\infty = 20)}, \tag{3.42}$$

where the modified Dahlem–Buck pressure coefficient $C_{p,\mathrm{MDB}}$ is assumed to follow a silmilar trend observed for cones.
The ratio of cone pressure coefficients is approximated by the analytical relation

$$\frac{C_{p,\mathrm{cone}}(M_\infty < 20)}{C_{p,\mathrm{cone}}(M_\infty = 20)} - 1 = a\,\delta^n, \tag{3.43}$$

where δ is expressed in degrees and the coefficients a and n depend on the freestream Mach number according to

$$a = (6.0 - 0.3M_\infty) + \sin\left(\frac{\ln(M_\infty) - 0.568}{1.20}\,\pi\right), \tag{3.44}$$

$$n = -\left(1.15 + 0.5\sin\left(\frac{\ln(M_\infty) - 0.916}{3.29}\,\pi\right)\right). \tag{3.45}$$

3.1.11 Van Dyke Unified

The Van Dyke unified method is a pressure estimation technique based on a unified small-disturbance theory, making it particularly suitable for thin aerodynamic configurations.
The relations, based on the hypersonic similarity concept, are obtained by manipulating the oblique shock relations under the assumptions of small flow deflection angles [4] and large Mach numbers. For a compression surface, the resulting expression for the pressure coefficient takes the form

$$C_p = \delta^2 \left[\frac{\gamma+1}{2} + \sqrt{\left(\frac{\gamma+1}{2}\right)^2 + \frac{4}{H^2}}\right], \tag{3.46}$$

where δ denotes the local flow deflection angle and H is the hypersonic similarity parameter.
In the original hypersonic similarity formulation, the parameter H is defined as $H = M_\infty\,\delta$. The unified formulation extends this definition to the supersonic regime by introducing the modified similarity parameter

$$H = \sqrt{M_\infty^2 - 1}\,\delta, \tag{3.47}$$

which is employed in practical implementations of the method.
An analogous formulation is used for expansion regions where no leading edge shock is present, such as on the leeward side of an airfoil. In this case, the pressure coefficient is given by

$$C_p = \delta^2 \frac{2}{\gamma H^2}\left[\left(1 - \frac{\gamma-1}{2}H\right)^{\frac{2\gamma}{\gamma-1}} - 1\right], \tag{3.48}$$

where the same unified similarity parameter $H = \sqrt{M_\infty^2 - 1}\,\delta$ is adopted.

[4] In the present work, the Van Dyke formulation is corrected for large deflection angles ($\delta > 1$) by replacing this method with a Prandtl–Meyer expansion from the freestream for shadow surface elements. In this regime, the similarity parameter H becomes excessively large, leading to nonphysical pressure predictions if the original formulation is applied without correction.

3.1.12 High Mach Base Pressures

The High Mach Base Pressures model is a corrective method for the evaluation of the pressure in the base region, included in the *APAS* [4] program and derived from experimental observations.
For a body immersed in a high-speed flow, it may be assumed that the base regions experience conditions of total vacuum, leading to $p_{\text{base}} = 0$.
Under this ideal assumption, the base pressure coefficient is given by

$$C_p = -\frac{1}{\gamma M_\infty^2/2}. \tag{3.49}$$

However, due to viscous effects in real gases, experimental data reveal that a certain level of pressure is recovered in the base region, limiting the pressure coefficient for air to

$$C_p = -\frac{1}{M_\infty^2}. \tag{3.50}$$

3.2 Aerodynamic Coefficient

The estimation of aerodynamic force coefficients within the framework of inviscid hypersonic analysis can be carried out starting from the local pressure coefficients, evaluated by means of one or more of the local surface inclination methods described above.
Based on the surface pressure coefficient distribution and the formulation proposed by Huang et aI. [6], the global aerodynamic force coefficient C and its decomposition into axial, lateral, and normal force coefficients, as well as moment coefficients, can be obtained by integrating the contributions of each surface element. In particular, the force coefficients expressed in the body-fixed reference frame are defined as

$$\begin{cases} C_x = \sum \dfrac{C_p\, n_x\, \Delta A}{S_{\text{ref}}}, \\ C_y = \sum \dfrac{C_p\, n_y\, \Delta A}{S_{\text{ref}}}, \\ C_z = \sum \dfrac{C_p\, n_z\, \Delta A}{S_{\text{ref}}}, \end{cases} \tag{3.51}$$

where C_p denotes the local pressure coefficient, n_x, n_y, and n_z are the components of the outward unit normal vector associated with each surface element, ΔA is the surface element area, and S_{ref} is the reference surface area of the vehicle.

Lift Coefficient

The lift coefficient is obtained by projecting the aerodynamic force components onto the aerodynamic reference frame. For a given angle of attack α, it is defined as

$$C_L = -C_x \sin\alpha + C_z \cos\alpha. \tag{3.52}$$

Drag Coefficient

The aerodynamic drag coefficient is computed as the projection of the total aerodynamic force along the freestream direction. In the presence of a sideslip angle β, assumed to be 0 in this work, it is expressed as

$$C_D = C_x \cos\alpha \sin\beta + C_y \sin\beta + C_z \sin\alpha \cos\beta. \tag{3.53}$$

Pitch Moment Coefficient

The pitch moment coefficient, evaluated about the vehicle center of gravity, is obtained by integrating the moments generated by the pressure forces acting on the surface elements. It is defined as

$$C_M = \frac{\sum C_p(x - x_{CG})n_z \Delta A - \sum C_p(z - z_{CG})n_x \Delta A}{S_{\text{ref}}\, b_{\text{ref}}}, \tag{3.54}$$

where (x_{CG}, z_{CG}) denote the coordinates of the center of gravity [5] and b_{ref} is the reference wingspan of the vehicle.

[5] In the present analysis, the actual mass center of gravity of the vehicle is not available. Therefore, the geometric centroid of the configuration is adopted as the reference point for pitch moment evaluation.

Chapter 4

Numerical Implementation of the Aerodynamic Models in MATLAB

4.1 MATLAB Console and User Interface

The Aerodynamic Characterisation of an STL (Standard Triangulation Language) file is implemented via an interactive MATLAB console that appears in the Command Window. The console is designed to guide a user through a computational pipeline organised into seven sequential stages, where at each stage the user is prompted to provide the required inputs or select from available modelling options, while checks and visual feedback are provided.
Subsequent sections describe the main input stages of the console and their roles within the computational pipeline. The process begins with the definition of freestream conditions and continues through geometry selection, method assignment, aerodynamic performance evaluation, and the benchmarking process with external data.

4.1.1 Freestream Input Conditions

At the first stage, the user is prompted to specify the flight altitude h necessary for the evaluation of the free-stream condition, the free-stream Mach number M_∞, and the angle of attack α. The altitude is limited to 80 000 m according to both the validity range of `atmosisa(h)` routine, which provides tabulated standard atmosphere properties (T_∞, a_∞, p_∞ ρ_∞), and the continuum flow assumption adopted for the subsequent computational fluid dynamics analysis.

Starting from M_∞, the freestream velocity magnitude is computed as

$$\boldsymbol{V}_\infty = M_\infty \, a_\infty \begin{bmatrix} 1 & 0 & 0 \end{bmatrix}. \tag{4.1}$$

and the velocity vector is defined consistently with the global reference frame.
Under the assumption of a calorically perfect gas with constant ratio of specific heats $\gamma = 1.4$[1], the total-to-static pressure ratio downstream of a normal shock at the stagnation point, $p_{0,2}/p_\infty$, is evaluated according to normal shock relations as

$$\frac{p_{0,2}}{p_\infty} = \left(\frac{(\gamma+1)^2 M_\infty^2}{4\gamma M_\infty^2 - 2(\gamma-1)} \right)^{\frac{\gamma}{\gamma-1}} \left(\frac{1-\gamma+2\gamma M_\infty^2}{\gamma+1} \right). \tag{4.2}$$

Then, the maximum pressure coefficient at the stagnation point, $C_{p,\max}$, is then computed by assuming a normal shock at the stagnation point as

$$C_{p,\max} = \frac{2}{\gamma M_\infty^2} \left(\frac{p_{0,2}}{p_\infty} - 1 \right), \tag{4.3}$$

where $p_{0,2}$ denotes the total pressure immediately downstream of the shock.
The resulting value of $C_{p,\max}$ is used as a reference upper bound for consistency checks during the application of windward pressure models. As an example, Figure 4.1 illustrates the corresponding section of the MATLAB console.

```
============================================================
   ROMS - Reduced Order Models for Hypersonic configuration
        ( Mini Daniele - Politecnico di Torino / MBDA )
============================================================


--- Definizione condizioni di freestream ---
--------------------------------------------
Quota (m) [default 0] < 80000: 10000
Numero di Mach M_∞ >5 [default 10]: 8
Angolo di incidenza α (deg) [default 0]: 0

>> Condizioni impostate:
   h         = 10000.0 m
   M_∞       = 8.000
   V_∞       = 2395.7 m/s
   α         = 0.00 deg
   T_∞       = 223.1 K
   p_∞       = 26436.243 Pa
   ρ_∞       = 0.41271 kg/m^3
   γ         = 1.40
   Cpmax       = 1.82735
   p^0_2/p_∞  = 82.86547
```

Figure 4.1: MATLAB console, Section 1 : Freestream Conditions.

[1]The ratio of specific heats is assumed constant in the present work. but future developments may include temperature-dependent models to account high-temperature effects.

4.1.2 Geometry Selection and Properties

This section describes the selection and preprocessing of surface geometry from the working directory that contains the main MATLAB script and associated functions. After selecting the STL file, the outward normal vectors for each mesh surface element are computed, and the geometric centre of gravity is determined. This preprocessing stage also involves identifying the base region and evaluating the main geometric characteristics of the body, including characteristic lengths and reference dimensions.

Geometry Normals & Exposed/Shadow Regions

After selecting the STL surface mesh, in the present implementation, the geometry is rotated to match the prescribed angle of attack α, rather than modifying the freestream velocity vector, to ensure a consistent definition of surface normal orientation and, consequently, of the windward and leeward regions.

The rotation is performed about the Y axis by applying the standard rotation matrix:

$$\mathbf{R}_y(\alpha) = \begin{bmatrix} \cos\alpha & 0 & \sin\alpha \\ 0 & 1 & 0 \\ -\sin\alpha & 0 & \cos\alpha \end{bmatrix}. \tag{4.4}$$

As a consequence, each vertex $\mathbf{x}$ of the original triangulation is mapped to the rotated position $\mathbf{x}' = \mathbf{R}_y(\alpha)\,\mathbf{x}$.
This approach allows the aerodynamic analysis to be performed on the rotated surface while keeping the freestream velocity vector fixed as $\mathbf{V}_\infty = V_\infty[1\ 0\ 0]$[2].
Within this choice, the local inclination information is entirely contained in the surface normals, and the scalar product simplifies to

$$\mathbf{n}_i \cdot \mathbf{V}_\infty = |\mathbf{n}_i|\,|\mathbf{V}_\infty| \cos\theta_i = n_{x,i}\,V_\infty,$$

so that both the exposed/shadow classification and the evaluation of local inclination angles are obtained directly from the x-component of the normal vector, reducing the overall computational complexity.
Once the rotated triangulation T_R is constructed, the outward unit normal vector associated with each triangular face is obtained through the MATLAB routine `faceNormal(TR)` and represented at the face centroids. Denoting by $\mathbf{P}_{1,i}$, $\mathbf{P}_{2,i}$ and

[2]To ensure the correct behaviour of the preprocessing routine, the original (unrotated) STL geometry is supposed oriented with the nose pointing towards the negative x direction, i.e. opposite to the freestream velocity direction.

$\mathbf{P}_{3,i}$ the vertices of the i-th triangle, the centroid location is evaluated as

$$\mathbf{C}_i = \frac{\mathbf{P}_{1,i} + \mathbf{P}_{2,i} + \mathbf{P}_{3,i}}{3}. \tag{4.5}$$

In addition, the sign of the x-component of each normal vector, $n_{x,i}$, is used to distinguish between faces directly exposed to the freestream and faces located in the shadow region. Introducing a threshold `shadow_limit`, the classification is performed as

$$\text{exposed: } n_{x,i} < \texttt{shadow\_limit}, \qquad \text{shadow: } n_{x,i} \geq \texttt{shadow\_limit}. \tag{4.6}$$

In the present work, the `shadow_limit` is not set to zero, but rather to a small positive value(`shadow_limit` $= 0.04$) to mitigate numerical noise arising from the triangulation of curved surfaces, for which locally misaligned facets may yield n_x close to zero even in regions exposed to the freestream[3]. A comparison between the two classifications is shown in Fig. 4.2, while an example of the resulting normal-field visualization for a test geometry is reported in Fig. 4.3b.

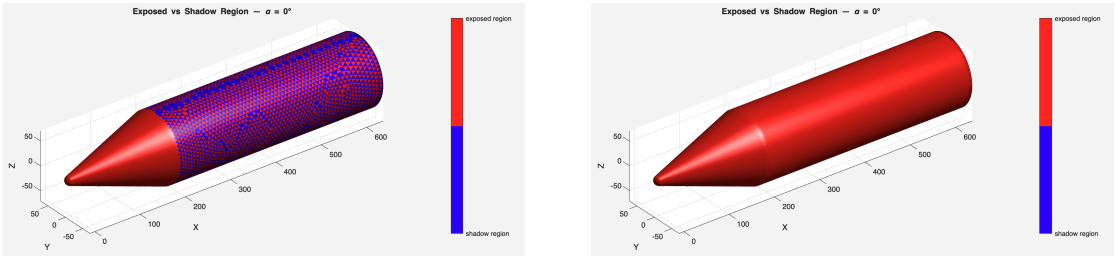

(a) `shadow_limit` $= 0$ **(b)** `shadow_limit` $= 0.04$

Figure 4.2: Effect of the `shadow_limit` parameter on the exposed/shadow classification for a curved surface. (a) `shadow_limit` $= 0$, numerical noise. (b) `shadow_limit` $= 0.04$.

Geometric Centre of Gravity & Momentum Reference Point

Once the rotated triangulation T_R is available, the geometric centre of gravity of the body is evaluated, and it can be as the reference point for the computation of aerodynamic moments . Since the actual mass distribution of the vehicle is not known, a purely geometric definition of the centre of gravity is adopted.
For a solid occupying a volume V, the barycentre is defined as $\mathbf{r}_G = \frac{1}{M}\int_V \rho(\mathbf{r})\,\mathbf{r}\,dV$,

[3]Surface elements' outward normal that satisfies $n_x = 0$ are classified as exposed to the freestream.

where $\rho(\mathbf{r})$ denotes the mass density and $M = \int_V \rho(\mathbf{r})\, dV$ is the total mass. In the present work, the density is assumed to be uniform, so that the barycentre coincides with the geometric centre of the volume and the expression reduces to

$$\mathbf{r}_G = \frac{1}{V} \int_V \mathbf{r}\, dV. \tag{4.7}$$

The total volume of the solid is then obtained by decomposing the closed triangulated surface into tetrahedra obtained by connecting the vertices of each triangular face to the origin of the reference frame. For the i-th triangular face with vertices $\mathbf{P}_{1,i}$, $\mathbf{P}_{2,i}$ and $\mathbf{P}_{3,i}$, the location of the centroid tetrahedron is evaluated as

$$\mathbf{r}_i = \frac{\mathbf{P}_{1,i} + \mathbf{P}_{2,i} + \mathbf{P}_{3,i} + \mathbf{O}}{4}, \tag{4.8}$$

where $\mathbf{P}_{1,i}$, $\mathbf{P}_{2,i}$, $\mathbf{P}_{3,i}$ and the origin $\mathbf{O} = (0,0,0)$ denote the position vectors of the tetrahedron vertices.
Then, the volume of each tetrahedron is computed with the algebric formulation

$$V_i = \frac{1}{6}\, \mathbf{P}_{1,i} \cdot (\mathbf{P}_{2,i} \times \mathbf{P}_{3,i}) = \frac{1}{6} \begin{vmatrix} P_{1,i,x} & P_{1,i,y} & P_{1,i,z} \\ P_{2,i,x} & P_{2,i,y} & P_{2,i,z} \\ P_{3,i,x} & P_{3,i,y} & P_{3,i,z} \end{vmatrix}, \tag{4.9}$$

Equation (4.7) can be rewritten in discrete form as a summation over the tetrahedral elements composing the volume. In particular, the geometric centre of gravity components are given by

$$\begin{cases} x_G = \dfrac{\sum_i V_i\, x_i}{\sum_i V_i}, \\ y_G = \dfrac{\sum_i V_i\, y_i}{\sum_i V_i}, \\ z_G = \dfrac{\sum_i V_i\, z_i}{\sum_i V_i}, \end{cases} \qquad \Rightarrow \qquad \mathbf{r}_G = (x_G, y_G, z_G) = \frac{\sum_i V_i\, \mathbf{r}_i}{\sum_i V_i}, \tag{4.10}$$

The triangulated surface mesh and the corresponding geometric centre of gravity are shown in Fig. 4.3a.
A possible extension of the present implementation could include the use of the real centre of gravity of the vehicle, once the mass distribution is known. The location of the center of gravity is verified against that computed in FreeCAD.
At this stage, the user is prompted to use the geometric center of gravity as a reference point for the momentum or to manually input the coordinates of the point he prefers, as shown in Fig 4.4a.

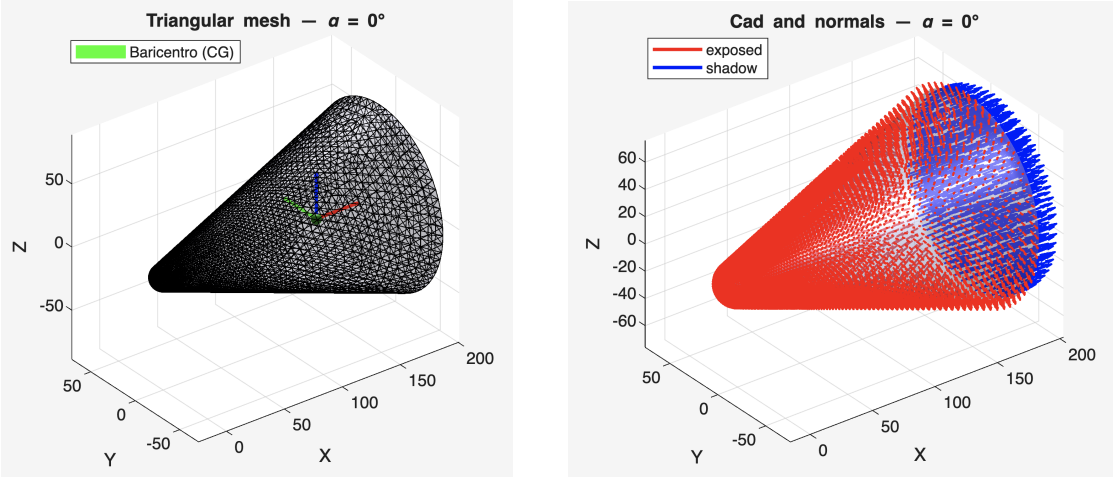

(a) Surface mesh **(b)** Surface normals

Figure 4.3: MATLAB console, Section 2: Mesh and surface normals. (a) Surface mesh and geometric centre of gravity. (b) Exposed and shadow-region normals.

Base Identification

The base region of the body is identified using a visual–geometric criterion based on two user-defined parameters: the percentage of the total body length and a positive threshold value for the magnitude of the outward normal vector component.
Once these parameters are defined, after a diagnostic visualization is generated, the user is prompted to visually inspect the resulting identification and to provide feedback on its correctness.
For the correct identification, the triangulated surface is re-rotated with the angle α using the following matrix:

$$\mathbf{R}_{inv}(\alpha) = \begin{bmatrix} \cos -\alpha & 0 & \sin -\alpha \\ 0 & 1 & 0 \\ -\sin -\alpha & 0 & \cos -\alpha \end{bmatrix}. \tag{4.11}$$

An example of this procedure is shown in Fig 4.4.

Geometrical Properties

Once the triangulated surface mesh is available, the main geometrical properties of the body are evaluated and stored for subsequent aerodynamic analyses. In particular, the following reference quantities are identified.

- The **Body length** L is defined as the extent of the geometry along the streamwise direction. It is computed as the distance between the minimum

and maximum x-coordinates of the mesh vertices,

$$L = x_{\max} - x_{\min}. \tag{4.12}$$

- The **Spanwise dimension** b is defined as the total extent of the geometry along the y-direction and is evaluated as

$$b = y_{\max} - y_{\min}, \tag{4.13}$$

with $y_{\min}$ and $y_{\max}$ representing the minimum and maximum y-coordinates of the triangulated surface.

- The **Reference surface** S_{ref} required for the subsequent evaluation of aerodynamic force coefficients can either coincide with the base area of the body, as typically adopted for missile-like configurations, or be specified manually by the user.

The geometrical properties section of the MATLAB console is shown in Fig 4.4.

```
--- Seleziona un file STL dalla cartella corrente ---
------------------------------------------------------
  1) bluntedcone.stl
  2) hgv.stl
  3) proiettile.stl
  4) sphere_test.stl
Seleziona la geometria (1-4)[default 1]: 1

>> Geometria selezionata: bluntedcone.stl


--- Definizione Punto di Riferimento per il calcolo dei Momenti ---
--------------------------------------------------------------------------------
Si preferisce inserire il riferimento manualmente (m)
 o utilizzare il baricentro geometrico (g, default)? [g/m]: m

Inserire coordinate del riferimento (prima della rotazione)[mm]:
ATTENZIONE: Xr è la distanza dal punto più avanzato
Xr = 50

Yr = 0

Zr = 0


--- Identificazione della BASE ---
----------------------------------
Criteri correnti per definizione BASE:
Percentuale lunghezza corpo [default 90.0]: 90

Soglia normale n_x [default 0.85]: 0.85

La base va bene [default yes]? [y/n] y

>> Base confermata.


---Caratteristiche geometriche:---
-----------------------------------
Superficie di base S_ref = 15900.552 mm^2
Lunghezza corpo L= 196.79 mm
Apertura alare b = 142.40 mm

La superficie di riferimento coincide con la superficie di base?
  1 - Si  (default)
  2 - No, inserisci manualmente la superficie di riferimento Sref
Scelta (1-2): 1

>> Sref = S_base = 15900.552405 mm^2
```

(a)

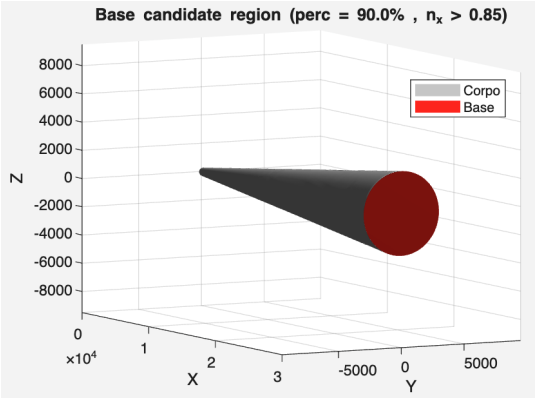

(b)

Figure 4.4: MATLAB console, Section 2: Geometrical Properties. (a) MATLAB Command Window. (b) Base candidate region for base identification criteria.

4.1.3 Body-Wing Separation Option

The body-wing separation option allows the user to treat the entire body as a single body or split it into two components respectively the wing and the fuselage:

- In the **full-body** option two distinct methods can be applied to the exposed and shadow regions of the entire surface.
- In the **Body-Wing Separation Option** the geometry is decomposed into wing and fuselage surfaces, and different aerodynamic methods can be independently assigned to the exposed and shadow regions of each component.

The separation procedure is based on a visual-geometric inspection, in which the user is asked to specify a percentage value (`perc`) of the semi-span $\frac{b}{2}$ or the phisical lenght dy.
Then a diagnostic plot is generated, and the user can iteratively adjust `perc` or dy until a satisfactory separation is achieved. When the separation is performed, the mesh triangles are classified into two groups according to the position of their centroids along the semi-span[4].
This option is introduced to account for the fact that the aerodynamic methods implemented in the present framework are known to perform differently on blunt and slender surfaces, which are typically associated with fuselage and wing-like geometries.
An example of the body-wing separation procedure is shown in Fig. 4.5.

```
Vuoi usare metodi diversi per ala e fusoliera [default no]? [y/n] y

--- Separazione ala / fusoliera tramite percentuale in |y| ---
------------------------------------------------------------------------
Come preferisci definire la soglia laterale?
  1 - Percentuale della distanza laterale massima (default)
  2 - Lunghezza fisica dy [mm]
Scelta (1-2): 1
Inserisci soglia percentuale (0-100) [default 20]:
>> Soglia laterale: 20.00 %  →  dy = 0.600000 mm
Soglia effettiva dy  = 0.59 mm
La separazione va bene [default yes]? [y/n] n
Come preferisci definire la soglia laterale?
  1 - Percentuale della distanza laterale massima (default)
  2 - Lunghezza fisica dy [mm]
Scelta (1-2): 2
Inserisci lunghezza dy [mm]: 0.6
>> Soglia laterale: dy = 0.600000 mm  →  20.00 % della semiapertura
Soglia effettiva dy  = 0.59 mm
La separazione va bene [default yes]? [y/n]
```

(a)

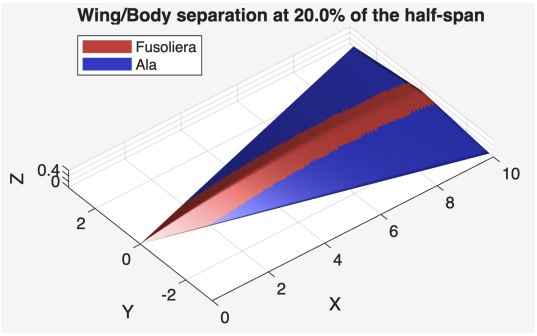

(b)

Figure 4.5: MATLAB console, Section 3: Body-wing separation option. (a) MATLAB Command Window. (b) Candidate wing and fuselage regions based on the spanwise separation criterion.

A possible future development of the code could include the implementation of a machine-learning algorithm capable of automatically identifying and classifying the different geometric components, or the direct import of STL geometries already segmented into distinct parts at the CAD level.

[4]For the correct operation of the option, the axis of symmetry of the body must be aligned with the x-axis of the adopted reference frame.

4.1.4 Method Selection

Once the separation option has been selected, the user is guided through the choice of the aerodynamic models to be applied to the exposed and shadow regions, according to the characteristics of the geometry, as illustrated in Figures 4.6 and 4.7. When a windward surface method is selected, the pressure coefficient is preliminarily evaluated and compared with $C_{p,\max}$ computed in Eq. (4.3). This general criterion warns the user if the selected method produces potentially non-physical results and allows the user to choose another model.
Once a method has been selected, additional verification criteria and specific diagnostic plots are implemented. These are discussed in detail in the corresponding section on reduced-order aerodynamic models (see Section 4.2).

```
Vuoi usare metodi diversi per ala e fusoliera [default no]? [y/n] n
>> Geometria trattata come corpo unico .

--- Metodo per Regione Esposta ---
-----------------------------------
|
=============== EXPOSED REGION METHODS ===============
 1) Newtonian ..................... Suitable for blunt-nosed bodies
 2) Modified Newtonian .......... Newtonian + Cp correction
 3) Mod.Newton + Prandtl-Meyer... Mod. Newtonian + Exspansion Surface Correction
 4) Tangent Wedge ................ Suitable for 2-D sharp-nosed bodies with attached shock waves
 5) Tangent Wedge Empirical ..... More stable for small local inclination angle
 6) Tangent Cone ................. Suitable for 3-D sharp-nosed bodies with attached conical shock waves
 7) Tangent Cone Empirical ...... Faster than pure, not require Taylor-Macoll solution
 8) Inclinated Cone .............. Suitable for inclinated cone, extension of Newtonia
 9) Delta Wing Empirical ........ Suitable for Delta Wing design, combine Tang. Wedge and Cone
10) OSU Empirical ............... Suitable for blunt-body , developed for circular cilinders analysis
11) Hankey Empirical ............ Developed for blunted flat plates,incorporate Tan.Wedge at small impact angle while Newtonian
12) Dahlem-Buck ................. Suitable for highly swept configurations - The modified solution icludes a Mach dependent cor
13) Van Dyke Unified ............ Suitable for thin aerodynamic configurations, valid for small flow deflection angle
14) Shock Exspansion ............ Suitable for sharp-nosed bodies with attached oblique shock waves
=======================================================
```

(a)

```
Scegli metodo:
  1) Newtonian
  2) Modified Newtonian
  3) Modified Newtonian + Prandtl-Meyer
  4) Tangent Wedge
  5) Tangent Wedge empirical
  6) Tangent Cone
  7) Tangent Cone empirical
  8) Inclinated Cone
  9) Delta Wing empirical
 10) OSU empirical
 11) Hankey flat-surface
 12) Dahlem-Buck
 13) Van Dyke Unified
 14) Shock Exspansion
Metodo (1-14): 1
|
  ATTENZIONE: Cp_max = 1.993 > Cp_stagnazione = 1.832
Vuoi scegliere un altro metodo [default no]? [y/n] n
```

(b)

Figure 4.6: MATLAB console, Section 4: Method selection. (a) Exposed region guide. (b) Exposed region choice and Cp control.

```
--- Metodo per Regione D'Ombra ---
-----------------------------------

================ SHADOW REGION METHODS ================
 1) Cp = 0 (Newtonian) ..........
 2) OSU Empirical ............... Suitable for blunt-body , developed for circular cilinders analysis
 3) Mod.Newton + PM ............. PM Expansion from subsonic bowl / blunt-body configuration with deteached shock waves
 4) Van Dike Unified ............ Suitable for thin aerodynamic configurations, valid for small flow deflection angle - f
 5) Pradtl-Meyer Expansion from free stream
 6) Shock Exspansion ............ PM Expansion from leading edge  / sharp-nosed bodies with attached oblique shock waves
=======================================================
  1) Newtonian ( Cp = 0 )
  2) OSU blunt body empirical
  3) Modified Newtonian + Prandtl - Meyer
  4) Van Dike Unified
  5) Prandtl-Meyer from free stream
  6) Shock Expansion
Scegli metodo (1-6): 1
```

Figure 4.7: MATLAB console, Section 4: Method selection: Shadow region guide and choice.

High Mach Base Pressures (HMBP) Option

An additional option is provided for the assignment of the pressure coefficient to the triangular base elements identified in Section 4.1.2. In particular, the user is prompted to choose to apply the High Mach Base Pressure (HMBP) correction or to use the pressure coefficients previously evaluated using the selected leeward-surface method.
An illustration of thsee MATLAB Command Window interaction is shown in Fig. 4.8.

```
--- Metodo per la REGIONE DI BASE  ---
----------------------------------------
  Vuoi usare HIGH MACH BASE PRESSURES (HMBP) per la base?
   1) Sì, usa HMBP
   2) No, usa il metodo scelto per la regione d'ombra
Scelta (1-2)[default HMBP]: 1
>> Metodo base selezionato: HMBP
```

Figure 4.8: MATLAB console, Section 4: HMBP option.

Methods Choice Visualization

Finally, after the methods have been selected, a summary visualization is provided to the user to show which methods will be applied and to which regions of the geometry.
An example of the proposed visualization is shown in Fig. 4.9.

```
--- Visualizzazione metodi selezionati (ala + fusoliera)---
------------------------------------------------------------
I metodi selezionati sono corretti [default yes]? [y/n]
```

(a)

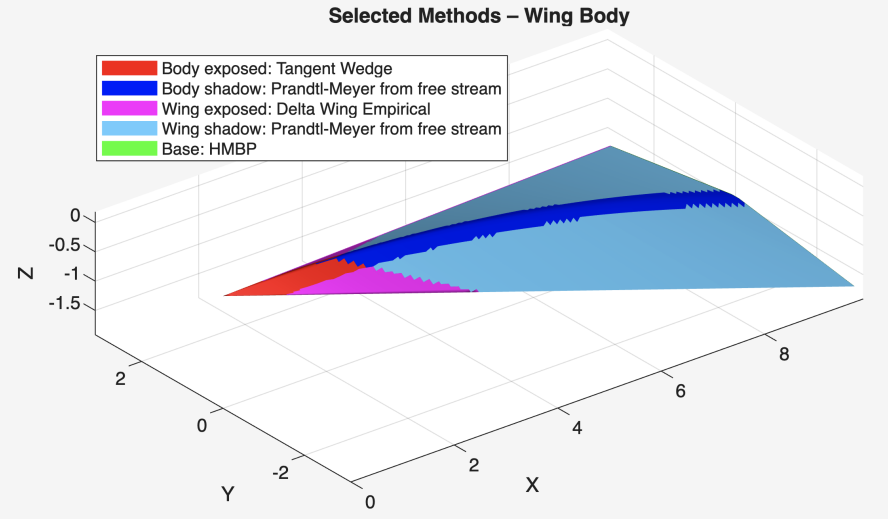

(b)

Figure 4.9: MATLAB console, Section 4: Methods choice and regions visualization. (a) Command Window. (b) Assignment of the selected methods to the different geometric regions.

At this point, the user can choose whether to proceed with the calculation of the pressure coefficients or select the methods again.

4.1.5 Pressure Coefficient Evaluation Cp

Once the aerodynamic methods have been selected, the pressure coefficients are calculated and subsequently assembled. Each selected method evaluates a pressure distribution over the entire body, and the resulting pressure coefficients are then assembled into the geometric subdivisions defined in the previous sections[5].
The pressure coefficients associated with the exposed surfaces are not calculated again, as they have already been evaluated during the comparison with $C_{p,\max}$, while those for the shadow and base regions are calculated at this stage.
An example of the pressure coefficient assembly procedure is shown in Fig. 4.10.

[5]The surface element indices are grouped according to their region (exposed, shadow, and base regions).

```
--- Visualizzazione metodi selezionati (corpo unico) ---
------------------------------------------------------------
I metodi selezionati sono corretti [default yes]? [y/n]

>> Calcolo exposed region...
>> Calcolo shadow region...
>> Calcolo base region...
   Metodo HMBP applicato: Cp_base = -0.0100

>> Assemblaggio Cp completato.
```

(a)

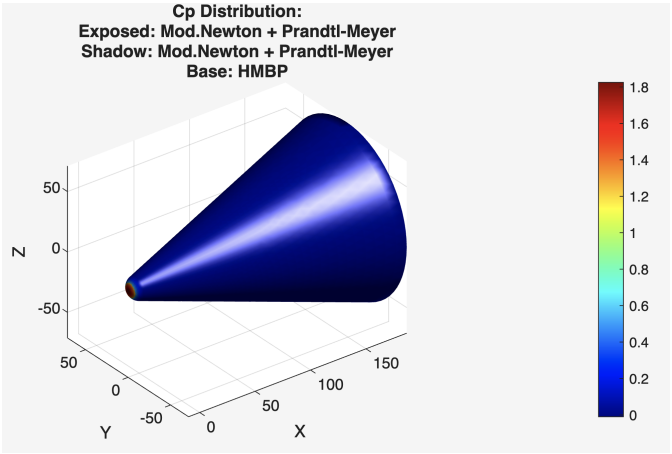

(b)

Figure 4.10: MATLAB console, Section 5: Pressure coefficient evaluation. (a) Command Window. (b) Cp distribution over a blunted cone at $\alpha = 0$.

A possible future development of the code could include blending functions to reduce pressure discontinuities at the interfaces between regions where different aerodynamic methods are applied.

4.1.6 Aerodynamic Coefficients and Performance Curves

Starting from the pressure coefficient distribution previously evaluated over the surface, the lift, drag, and moment coefficients are computed for each surface element according to the formulations introduced in Section 3.2.
In particular, the aerodynamic force coefficient acting on the i-th surface element is defined as

$$\boldsymbol{C}_{F,i} = -\, C_p(i)\, \boldsymbol{n}(i)\, \frac{A_i}{S_{\text{ref}}}, \tag{4.14}$$

where $\boldsymbol{n}(i)$ denotes the outward unit normal vector associated with the element, A_i is the area of the triangular surface element, S_{ref} is the reference surface, and the vector notation $\boldsymbol{C}_{F,i}$ is subsequently used to extract the local lift, drag and pitching-moment contributions.

The area of each triangular element is computed as

$$A_i = \frac{1}{2} \left\| (\mathbf{p}_{2,i} - \mathbf{p}_{1,i}) \times (\mathbf{p}_{3,i} - \mathbf{p}_{1,i}) \right\|, \tag{4.15}$$

where $\mathbf{p}_{1,i}$, $\mathbf{p}_{2,i}$ and $\mathbf{p}_{3,i}$ are the vertices of the i-th triangle.
The local lift, drag, and pitching moment coefficients are calculated assuming the side slip angle $\beta = 0$ and that the angle of attack information is already contained in the surface normals as follows:

$$\begin{cases} C_{L,i} = -\,C_p(i)\, n_y(i)\, \dfrac{A_i}{S_{\text{ref}}}, \\ C_{D,i} = -\,C_p(i)\, n_x(i)\, \dfrac{A_i}{S_{\text{ref}}}, \\ C_{M,i} = \;C_p(i)\, \dfrac{[(x_i - x_G)\, n_z(i) - (z_i - z_G)\, n_x(i)]\, A_i}{S_{\text{ref}}\, b}, \end{cases} \tag{4.16}$$

where (x_i, z_i) denote the coordinates of the i-th surface element centroid and (x_G, z_G) are the corresponding coordinates of the geometric centre of gravity.
The global lift, drag, and pitching-moment coefficients at a given α are finally obtained by superposition of the local contributions over all N surface elements:

$$\begin{cases} C_L = \displaystyle\sum_{i=1}^{N} C_{L,i}, \\ C_D = \displaystyle\sum_{i=1}^{N} C_{D,i}, \\ C_M = \displaystyle\sum_{i=1}^{N} C_{M,i}, \end{cases} \tag{4.17}$$

Performance Curves

The user is then prompted to define an angle of attack range $[\alpha_{\min},\, \alpha_{\max}]$ and the corresponding increment $\Delta\alpha$. For each prescribed incidence, the code applies the aerodynamic methods selected in the previous sections and computes the global coefficients C_L, C_D, C_M, and the aerodynamic efficiency

$$E = \frac{C_L}{C_D}.$$

The resulting quantities are then used to build the performance curves reported in Fig. 4.11.
In addition, the overall computational time required to evaluate the full set of angles and generate the curves is measured. This metric is later used for comparison against the time associated with the corresponding high-fidelity CFD analyses.

```
--- COEFFICIENTI AERODINAMICI ---
--------------------------------
CL = -0.00152
CD = 0.05522
E = -0.02746
CM = -0.00132  (attorno a CG)

Vuoi plottare le distribuzioni di CL, CD, CM e E?[default no] [y/n] n

--- Definizione range di incidenza ---
---------------------------------------
Alpha minimo (deg) [default 0]:
Alpha massimo (deg) [default 20]:
Passo alpha (deg) [default 5]:
>> Range alpha: [0, 20] deg | passo = 5 deg
>> Calcolo Cp = Cp(α)...

Vuoi plottare le curve CL-α, CD-α, CM-α, CL-CD, E-α?[default no] [y/n] y
>> Costruisco curve...
>> Curve costruite

Numero di angoli testati : 5
Numero di elementi di superfice : 22904
Tempo impiegato : 0.466 s
```

(a)

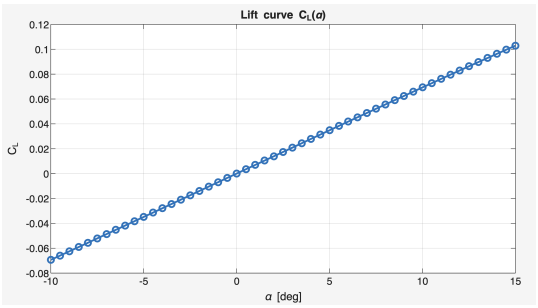

(b)

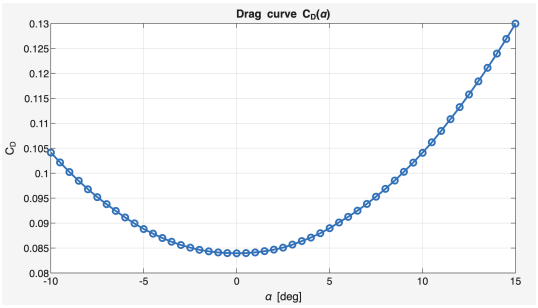

(c)

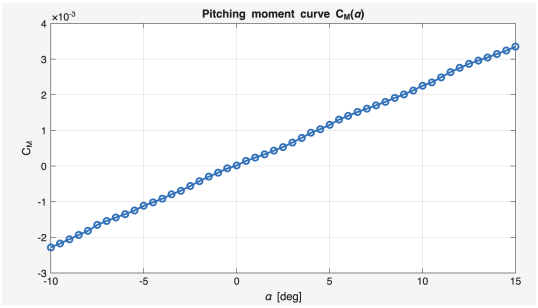

(d)

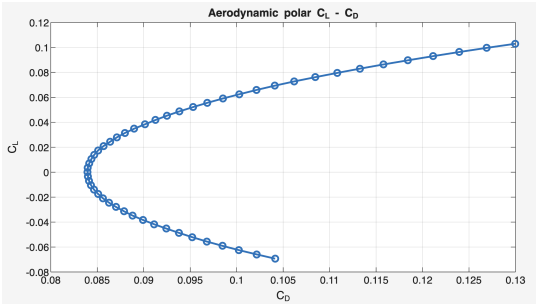

(e)

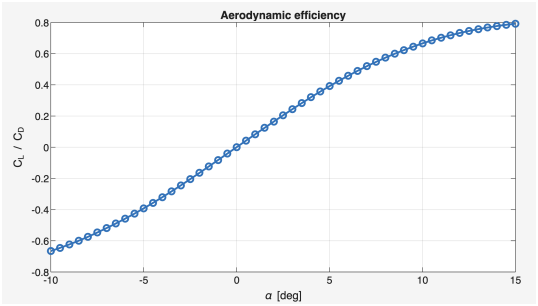

(f)

Figure 4.11: MATLAB console, Section 6: Aerodynamics curves for a blunted cone. (a) Command widow. (b) $C_L(\alpha)$. (c) $C_D(\alpha)$. (d) $C_M(\alpha)$. (e) $C_L(C_D)$. (f) $E = \frac{C_L}{C_D}$.

Data Saving Option

Once the aerodynamic characterization has been carried out, the user has the possibility to save and export the results and features of the simulation carried out in a struct type file, as proposed in Fig. 4.12 and Fig. 4.13.

```
Vuoi salvare i risultati delle curve? [default no] [y/n] y
Inserisci il nome del file: r0101

>> Salvato: /Volumes/SSD/tesi/CODICE TESI /risultati/r0101_M6.00.mat
```

Figure 4.12: MATLAB console, Section 6: Data saving option Command widow.

results ×

1×1 struct with 3 fields

Field	Value	Size	Class
data	*5×5 double*	5×5	double
label	*1×5 cell*	1×5	cell
features	*1×1 struct*	1×1	struct
h_m	75000	1×1	double
M_inf	6	1×1	double
gamma	1.4000	1×1	double
T_inf_K	206.6500	1×1	double
p_inf_Pa	2.0679	1×1	double
rho_inf_kgm3	3.4860e-05	1×1	double
alpha_min_deg	0	1×1	double
alpha_max_deg	20	1×1	double
alpha_step_deg	5	1×1	double
Sref_mm2	2.8218e+07	1×1	double
b_mm	5.9970e+03	1×1	double
L_mm	30000	1×1	double
CG_mm	[2.0464e+04,0.4381,-7.4481e+03]	1×3	double
use_body_wing	0	1×1	logical
method_exposed	'Newtonian'	1×9	char
method_shadow	'Cp = 0 (Newtonian)'	1×18	char
method_base	'HMBP'	1×4	char
exe_time	0.4657	1×1	double

Figure 4.13: MATLAB console, Section 6: Struct type results

4.1.7 Comparison with External Data

The last section of the console allows comparison of the aerodynamic results with known data, for example, CFD or experimental results. The comparison is made by estimating the relative percentage errors for the CL, CD, CM, and E results obtained on the same α incidences.[6]

[6]It is possible to evaluate a number of angles such that $N_{\text{ROM}} > N_{\text{CFD}}$. However, for a correct error evaluation, each angle imported from the external dataset must lie within the angle-of-attack range defined in Section 4.1.6.

For each angle of attack α_i, the relative error is defined as

$$e_r(\alpha_i) = \frac{|X_{\text{ROM}}(\alpha_i) - X_{\text{CFD}}(\alpha_i)|}{|X_{\text{CFD}}(\alpha_i)|} \cdot 100\,. \tag{4.18}$$

The quantity X may represent the lift coefficient C_L, the drag coefficient C_D, the pitch moment coefficient C_M, or the aerodynamic efficiency E.
For the configuration tested, the relative error is set to zero for C_L, E, and C_M whenever the corresponding coefficient obtained from the CFD analysis is close to zero, in order to avoid numerical issues .
For the comparison, the external data must be available in the same directory as the code and provided in the following MATLAB matrix format:

$$[\alpha(:)\,[\text{deg}],\ C_D(:),\ C_L(:),\ C_M(:),\ E(:)].$$

Subsequently, the user is prompted to select the comparison file from the available options, as shown in Fig. 4.14.

```
Vuoi confrontare il metodo con CFD data? [default yes] [y/n]
ATTENZIONE il file deve essere una matrice tipo [α(:)[deg], CD(:) , CL(:)]
ATTENZIONE per il corretto calcolo dell'errore tutti gli angoli α_CFD devono essere contenuti negli angoli testati α_range_ROM

--- Confronto CFD ---
------------------------------
Geometria testata: r0101.stl a M=6.0
File Disponibili
  1) r0101M4
  2) r0101M6
  3) r0102M6
  4) r0104M6
  5) r0108M6
  6) r0301M6
  7) r0302M6
  8) r0304M6
  9) r0308M6
  10) r0501M6
  11) r0502M6
  12) r0504M6
  13) r0508M6
  14) r07501M6
  15) r07502M6
  16) r07504M6
  17) r07508M4
  18) r07508M6
Seleziona la tabella CFD (1–18) [default 1]: 2
>> Tabella selezionata: r0101M6
```

Figure 4.14: MATLAB console, Section 7: Command widow.

When the comparison process starts, several curves are generated to highlight the deviation of the ROM results from the external data. An example is provided in Fig. 4.15.
At the same time, the console displays the maximum errors associated with a specific incidence angle $\alpha(e_{r,max})$, and the average error evaluated over all incidences. The latter will be used as a validation parameter in subsequent analyses.
Finally, to speed up the comparison process, the user can choose whether to select new methods on the same geometry or import a new one and restart the process. An example of this procedure is reported in Fig. 4.16.

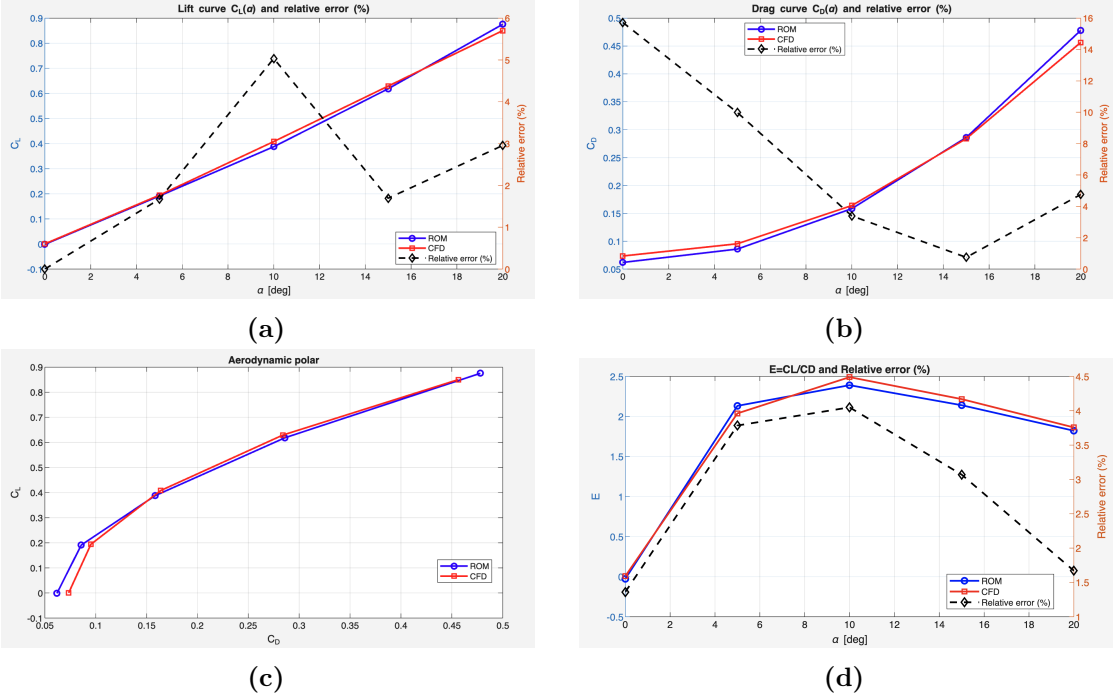

Figure 4.15: MATLAB console, Section 7: Aerodynamics curves and relative errors for a blunted cone using Newtonian Method. (a) $C_L(\alpha)$. (b) $C_D(\alpha)$. (c) $C_L(C_D)$. (d) $E = \frac{C_L}{C_D}$

.

```
Errori relativi percentuali massimi :
>> err_max_CL =  5.04% ottenuto a α = 10.00
>> err_max_CD =  15.73% ottenuto a α = 0.00
>> err_max_E =  9.24% ottenuto a α = 5.00

Errori relativi  percentuali medi [e_CL e_CD e_E] :
>> err_mean_rms = [ 2.27 6.92 3.02 ]

--- Caratteristiche Simulazione ---
-----------------------------------

>> Metodi ROM utilizzati:
   Exposed: Tangent Cone
   Shadow: Cp = 0 (Newtonian)
   Base: HMBP
   Numero di elementi di superfice : 22904
   Numero di angoli testati : 5
   Tempo impiegato : 1.191 s

Vuoi fare un test con un altro metodo sulla stessa geometria [default yes]? [y/n] n

Vuoi lanciare un'altra configurazione [default no]? [y/n] n

==========================================
  ROMS terminato. Fine sessione.
==========================================
```

Figure 4.16: MATLAB console, Section 7: Command widow, last option.

4.2 ROMs Implementation in MATLAB

This section describes how the reduced-order aerodynamic methods have been implemented in the MATLAB code and which checks and graphical outputs are employed to characterize their behavior and validity.
In particular, the functions implementing the various models share the following common features:

- All methods exploit the information on the local inclination angle δ, evaluated on each surface element as a function of the local outward normal. The angle δ is computed through Eq. (3.6) and is distributed in the interval $[-\pi/2,\ \pi/2]$, as illustrated in Fig. 4.17.

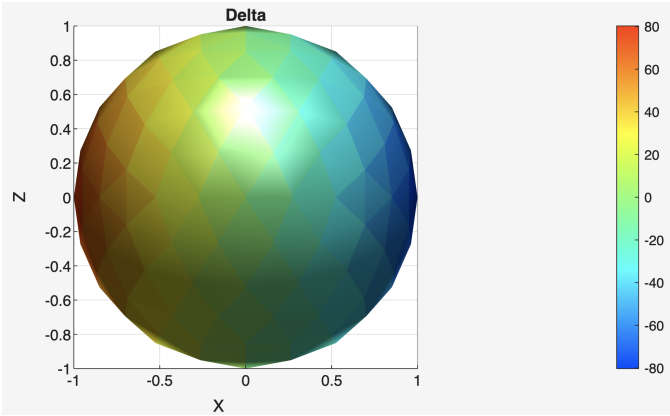

Figure 4.17: Distribution of the local inclination angle δ over the surface elements of a spherical geometry.

- All methods evaluate the pressure coefficient C_p on each surface element over the entire body surface. For methods applicable only to the exposed (windward) region, $C_p = 0$ is assigned to all elements belonging to the shadow region. Conversely, the shadow (leeward) region methods assign $C_p = 0$ to the exposed surfaces. Methods that are valid for both windward and leeward regions do not apply this selective masking.

- A physical consistency check enforcing $C_p \leq C_{p,\max}$ is applied to all methods. Depending on the specific formulation, additional method-dependent applicability checks are performed. These checks may generate warnings when the selected aerodynamic model is used outside its intended range of validity.

- The functions implementing the aerodynamic models classify the surface triangles into groups by storing their corresponding indices. Logical arrays are commonly employed for this purpose (e.g. `is_shadow =` $n_{x,i} \geq$ `shadow_limit`),

together with the `find` routine (e.g. `idx_PM = find(is_PM)`) to identify and operate on specific subsets of surface elements, such as expansion and compression regions.

In the following, the main characteristics and implementation details of some of the individual methods are presented, with reference to the formulations introduced in Section 3.1.[7]

4.2.1 Modified Newtonian + Prandtl-Meyer

Once the method is selected, following the procedure postulated by Gentry [3] in Section 3.1.3, a figure is generated to visualize the different regions of applicability over the reference surface, namely the Prandtl-Meyer formulation for expansion regions and the Modified Newtonian model for compression surfaces. An example of this classification is shown in Fig. 4.18.

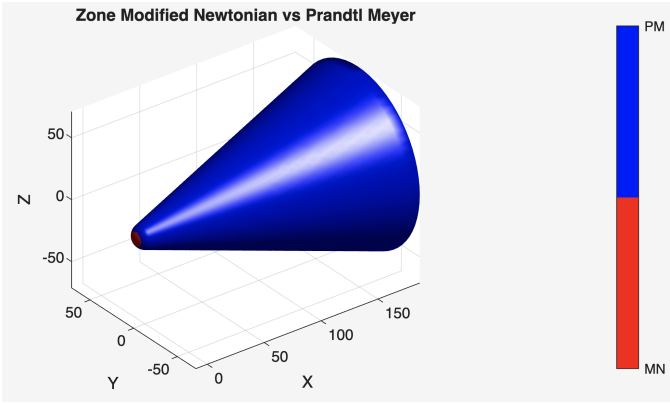

Figure 4.18: MATLAB console, Section 4: MN+PM option: Surface classification for compression and expansion regions.

The inclination angle at the matching point, $\delta_q = 35.4185°$, and the corresponding Mach number at the onset of the Prandtl-Meyer expansion, $M_{q,c} = 1.3524$, are determined as

$$\delta_q = \arcsin\left(\sqrt{\frac{Q_{q,c} - P_{q,c}}{1 - P_{q,c}}}\right), \qquad M_{q,c} = \texttt{interp1}(P_q, M_q, 0, \texttt{'linear'}).$$

The Mach number on each surface element belonging to an expansion region is then evaluated by inverting the Prandtl-Meyer function through a numerical root-finding

[7] Not all methods are discussed again, since several of them consist of a direct evaluation of an analytical expression as a function of the local inclination angle δ. Instead, this section focuses on specific cases where particular implementation choices or additional treatments were required.

procedure based on the `fzero` routine.
For this case, and for all subsequent methods involving the Prandtl-Meyer formulation, specific precautions were adopted to handle strong over-expansions associated with highly inclined regions, such as the base area. In particular, a wide search interval was prescribed for the `fzero` solver, namely $[1+10^{-6}, 6000]$[8] , and the maximum Prandtl-Meyer angle was limited to its physical upper bound corresponding to $M \to \infty$,

$$\nu_{\max} = \frac{\pi}{2}\left(\sqrt{\frac{\gamma+1}{\gamma-1}} - 1\right). \tag{4.19}$$

For over-expanded surface elements, a generic sufficiently large Mach number is assigned, set in this work to $M = 200$. This choice results in a pressure coefficient that is effectively close to zero in those regions. More physically representative values can be imposed by selecting the High Mach Base Pressure (HMBP) method for the base region and the Prandtl-Meyer from Free Stream formulation for shadow regions, which use an analogous routine for the evaluation of the Mach number on each surface element and prescribe that the pressure coefficient in over-expanded areas be set to

$$C_{p,\min} = -\frac{2}{\gamma M_\infty^2}. \tag{4.20}$$

4.2.2 Tangent Wedge

Once the method is selected, a check on the local inclination angle δ is performed over all surface elements. In particular, for given values of γ and M_∞, the local inclination angle is compared with the maximum allowable deflection angle $\delta_{\max}$, obtained by solving the oblique shock relations.
Two distinct regions are therefore identified:

$$\begin{cases} \delta_i < \delta_{\max} & \Rightarrow \text{Weak-shock region}, \\ \delta_i > \delta_{\max} & \Rightarrow \text{Strong-shock region}. \end{cases} \tag{4.21}$$

For surface panels belonging to the strong shock region the Tangent Wedge formulation is not physically valid and the Modified Newtonian model is proposed as an alternative. For the remaining panels in the exposed region, where an attached oblique shock is possible, the Tangent Wedge method is applied. An example of this classification is shown in Fig. 4.19.

[8]Here, 6000 represents an arbitrarily large Mach number. This upper bound can be increased or reduced, provided that the root of the Prandtl-Meyer inversion function lies within the selected interval.

```
Scegli metodo:
  1) Newtonian
  2) Modified Newtonian
  3) Modified Newtonian + Prandtl-Meyer
  4) Tangent Wedge
  5) Tangent Wedge empirical
  6) Tangent Cone
  7) Tangent Cone empirical
  8) Inclinated Cone
  9) Delta Wing empirical
 10) OSU empirical
 11) Hankey flat-surface
 12) Dahlem-Buck
 13) Van Dyke Unified
 14) Shock Exspansion
Metodo (1-14): 4

ATTENZIONE: sono stati individuati alcuni pannelli (rosso) con δ > δ_max.
 In queste regioni la teoria del cuneo tangente NON è fisicamente valida.
 Si consiglia l'uso del metodo newtoniano modificato in tali zone.

Vuoi applicare il Modified Newtonian solo ai pannelli con δ > δ_max? [default: y] [y/n]:
>> Applicazione del Modified Newtonian ai  pannelli non validi...
```

(a)

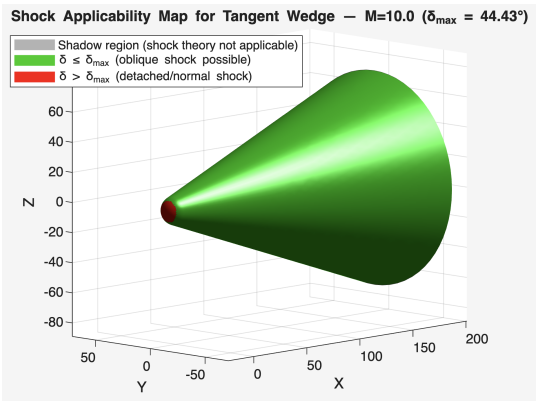

(b)

Figure 4.19: MATLAB console, Section 4: Tangent Wedge option. (a) Command Window. (b) Shock Map for tangent wedge method

To obtain the value of $\delta_{\max}$ and the shock angle β, the δ–β–M diagram is constructed starting from the freestream Mach number M_∞, following the equations described in [7]:

1. The domain of the shock angle β is defined in the interval $[\arcsin(\frac{1}{M_\infty}),\ \frac{\pi}{2}]$, and a vector of equally spaced points is generated within this range.

2. The corresponding deflection angle δ is computed for each value of β as

$$\delta = atan\left(2\cot(\beta)\,\frac{M_\infty^2\sin^2(\beta)-1}{M_\infty^2(\gamma+\cos(2\beta))+2}\right), \tag{4.22}$$

   and the maximum deflection angle $\delta_{\max}$ and the corresponding peak angle β_{peak} are identified.

3. For the attached-shock region, the solution for the shock angle β is obtained using the `fzero` routine applied to the function

$$f = \tan(\delta) - 2\cot(\beta)\,\frac{M_\infty^2\sin^2(\beta)-1}{M_\infty^2(\gamma+\cos(2\beta))+2},$$

   where, for each local deflection angle δ_i, the solution is found as

$$\beta = \texttt{fzero}(f,\,[\beta_{\min},\,\beta_{\text{peak}}]).$$

   The search interval is restricted to $[\beta_{\min},\,\beta_{\text{peak}}]$ in order to retain only the weak-shock solution.

4. The pressure ratio on each surface element is then evaluated as

$$\frac{p_i}{p_\infty} = 1 + \frac{2\gamma}{\gamma+1}\left(M_\infty^2 \sin^2\beta - 1\right).$$

5. In the case $\delta < 2°$, as proposed in the Gentry code [3], Eq. (4.23) is employed to avoid numerical errors in the solution:

$$\sin^2\beta = \frac{1}{M_\infty^2} + \frac{\gamma+1}{2}\frac{\delta}{\sqrt{M_\infty^2 - 1}}. \tag{4.23}$$

6. Finally, the Mach number downstream of the oblique shock is evaluated as

$$M_2 = \sqrt{\frac{1}{\sin^2(\beta-\delta)}\frac{2+(\gamma-1)M_\infty^2\sin^2\beta}{2\gamma M_\infty^2\sin^2\beta - (\gamma-1)}}.$$

4.2.3 Tangent Cone

Once the method is selected, a check is performed on each local inclination angle δ_i by comparing it with the maximum allowable deflection angle $\delta_{\max,TM}$, obtained by solving the Taylor–Maccoll ordinary differential equation for the given freestream Mach number M_∞.
As in the previous case, the applicability regions of the method are identified as

$$\begin{cases} \delta_i < \delta_{\max,TM} & \Rightarrow \text{Weak-shock region,} \\ \delta_i > \delta_{\max,TM} & \Rightarrow \text{Strong-shock region.} \end{cases} \tag{4.24}$$

Since the applicability of the Tangent Cone method requires the presence of an attached shock, the method is not valid in the strong shock region. Consequently, for surface panels belonging to the strong shock region, the Modified Newtonian model is adopted. An example is shown in Fig. 4.20.
To implement the method, the solution of the governing differential equation obtained through a MATLAB function developed to study supersonic flow over a cone was employed [8], which numerically solves the Taylor-Maccoll equation.
This function was modified and adapted to the present code, allowing the construction of the δ–β–M diagram and of a conical-shock table for the selected freestream Mach number M_∞.

```
------------------------------------------------------
Scegli metodo:
  1) Newtonian
  2) Modified Newtonian
  3) Modified Newtonian + Prandtl-Meyer
  4) Tangent Wedge
  5) Tangent Wedge empirical
  6) Tangent Cone
  7) Tangent Cone empirical
  8) Inclinated Cone
  9) Delta Wing empirical
 10) OSU empirical
 11) Hankey flat-surface
 12) Dahlem-Buck
 13) Van Dyke Unified
 14) Shock Exspansion
Metodo (1-14): 6

[TANGENTCONE] ATTENZIONE URTO STACCATO - CORPO BLUNT:
  delta_max locale = 86.536 deg
  delta_c_max Taylor-Maccoll = 56.859 deg
  Nella regione di urto staccato verrà usato il metodo Newtoniano Modificato.
```

Figure 4.20: MATLAB console, Section 4 :Tangent cone method applied to a blunted cone at $M_\infty = 10$.

The procedure is summarized as follows:

1. A vector of 200 shock angles β is generated in the interval $[\arcsin(1/M_\infty),\ \pi/2]$. The oblique-shock relation (4.22) is then used to estimate an initial vector of deflection angles δ.

2. For each value of β, the oblique shock is solved and the post-shock conditions are evaluated as

$$\begin{cases} M_{n1} = M_\infty \sin\beta, \\ M_{n2} = \sqrt{\dfrac{1 + \dfrac{\gamma-1}{2} M_{n1}^2}{\gamma M_{n1}^2 - \dfrac{\gamma-1}{2}}}, \\ M_2 = \dfrac{M_{n2}}{\sin(\beta - \delta)}. \end{cases} \tag{4.25}$$

3. Using the solution of the Taylor-Maccoll equation provided by the MATLAB function described in [8] and reported in Appendix A, the vectors δ_{cone} and $M_{2,c}$ are constructed as functions of the β vector[9] . These correspond, respectively, to the cone surface inclination angles generating a given β and to the Mach number of the flow on the corresponding surface element downstream of the conical shock.

[9]The function reported in Appendix A evaluates the solution for a single cone angle. In the present code, it has been embedded within a `for` loop in order to generate a vector of angles.

4. Using the isentropic and oblique-shock relations, the pressure coefficient C_p is computed for each δ_{cone}–β–Mach combination as follows:

$$\begin{cases} \dfrac{p_c}{p_{02}} = \left(1 + \dfrac{\gamma-1}{2} M_{2,c}^2\right)^{-\frac{\gamma}{\gamma-1}} \\ \dfrac{p_2}{p_1} = 1 + \dfrac{2\gamma}{\gamma+1}\left(M_{n1}^2 - 1\right) \\ \dfrac{p_{02}}{p_2} = \left(1 + \dfrac{\gamma-1}{2} M_2^2\right)^{\frac{\gamma}{\gamma-1}} \\ \dfrac{p_c}{p_\infty} = \left(\dfrac{p_{02}}{p_2}\right)\left(\dfrac{p_2}{p_\infty}\right)\left(\dfrac{p_c}{p_{02}}\right), \end{cases} \quad \Rightarrow \quad C_p = \frac{2}{\gamma M_\infty^2}\left[\left(\frac{p_c}{p_\infty}\right) - 1\right]. \tag{4.26}$$

5. Then a lookup table is constructed using the previously computed quantities. An example of this table is shown in Fig. 4.21.

TangentConeTable ×

1×1 struct with 8 fields

Field	Value	Size	Class
M_inf	10	1×1	double
gamma	1.4000	1×1	double
delta_c	*200×1 double*	200×1	double
beta	*200×1 double*	200×1	double
M2	*200×1 double*	200×1	double
Mc	*200×1 double*	200×1	double
p_ratio	*200×1 double*	200×1	double
Cp	*200×1 double*	200×1	double

Figure 4.21: MATLAB console, Section 4: Tangent cone table at $M_\infty = 10$.

6. The maximum value of δ_{cone}, $\delta_{\max,TM}$, is identified and assumed as the limit for an attached shock. The corresponding index $i_{\delta,\max}$ in the vector $\vec{\delta}_{\text{cone}}$ is then found, and the tabulated vectors are restricted to the range $[1,\ i_{\delta,\max}]$ in order to retain only the weak shock solution.

7. Each surface inclination angle $\delta_i < \delta_{\max,TM}$ is compared with the δ_{cone} values associated with the weak-shock solution. A linear interpolation is then performed to obtain the corresponding pressure coefficient C_p:

$$\begin{cases} \delta(i) \in [\delta_{cone}(j),\ \delta_{cone}(j+1)] \\ Cp(i) \in [C_{p,cone}(j),\ C_{p,cone}(j+1)] \end{cases} \tag{4.27}$$

$$C_p(i) = C_{p,cone}(j) + \frac{\delta(i) - \delta_{cone}(j)}{\delta_{cone}(j+1) - \delta_{cone}(j)}(C_{p,cone}(j+1) - C_{p,cone}(j)) \quad (4.28)$$

The table constructed using only the knowledge of M_∞ and γ, together with the subsequent linear interpolation, allows the solution of the differential equation to be avoided for each surface element, and therefore leads to a significant reduction in computational cost. In particular, the numerical error introduced by the linear interpolation decreases as the number of elements N_β of the shock-angle vector β used in the table construction increases.
This method is extremely advantageous from a computational point of view, since the Taylor–Maccoll equation is solved only N_β times, independently of the angle-of-attack range prescribed in the console. Without interpolation, the equation would instead be solved $N_\mathrm{e} \times N_\alpha$ times, where N_e denotes the number of surface elements and N_α represents the number of tested angles of attack.

4.2.4 Shock - Expansion

When the Shock-Expansion method is selected, the user is asked to define the number of horizontal strips used to subdivide the surface. An illustrative figure is then plotted, and the user is prompted to decide whether to modify this number or not. The procedure is illustrated in Fig. 4.22.

```
Scegli metodo:
  1) Newtonian
  2) Modified Newtonian
  3) Modified Newtonian + Prandtl-Meyer
  4) Tangent Wedge
  5) Tangent Wedge empirical
  6) Tangent Cone
  7) Tangent Cone empirical
  8) Inclinated Cone
  9) Delta Wing empirical
 10) OSU empirical
 11) Hankey flat-surface
 12) Dahlem-Buck
 13) Van Dyke Unified
 14) Shock Exspansion
Metodo (1-14): 14
Numero di strisce lungo l'apertura totale [default = 20]:
La separazione delle strisce va bene [default yes]? [y/n]: y
```

(a)

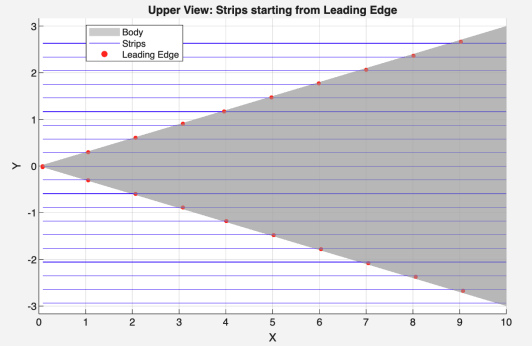

(b)

Figure 4.22: MATLAB console, Section 4: Shock-Expansion option. (a) Command Window. (b) Stirip Map for S-E method.

Starting from the diamond-shaped profile problem shown in Fig. 3.7 and described in greater detail in [9], the strip solution allows the originally two-dimensional problem to be extended to a three-dimensional configuration.
In particular, according to the Shock–Expansion theory, for each strip the leading edge is identified and, starting from it, the upper and lower surface regions are treated separately by applying, where possible, either the oblique-shock solution or

the free-expansion solution from the freestream. In the case of an oblique shock, the solution involves an expansion starting from the leading edge.
The procedure is described in the following:

1. To construct the strips, the centroids of the triangular elements and their corresponding coordinates $(X_c,\ Y_c)$ are identified. A set of equally spaced lines is then generated as

   $$\texttt{y\_edges} = \texttt{linspace}(y_{\min},\ y_{\max},\ N_{\text{strip}} + 1).$$

   Using the MATLAB `find` routine, the indices of the triangles belonging to each strip are grouped as

   ```
   in_strip = (Yc_s >= y_edges(s)) & (Yc_s < y_edges(s+1));
   idx_local = find(in_strip);
   ```

   A second grouping is then performed, using the same approach, within each strip according to the sign of the z-component of the surface normal:

   $$\begin{cases} n_z > 0 & \text{upper surface,} \\ n_z < 0 & \text{lower surface.} \end{cases}$$

2. For each strip, the most forward triangle (minimum x coordinate, $x_{\min}$) is identified separately for the upper and lower surface regions[10].

3. Since the information on the angle of attack α is already embedded in the surface normals, the local inclination angle δ is evaluated for the triangles identified as leading-edge elements, both on the upper and lower surfaces. Depending on its sign, either a free-expansion or an oblique-shock solution is applied:

   $$\begin{cases} \delta_{\text{LE,upper}}(i) > 0 \ \Rightarrow\ \text{upper surface of strip } i \text{ in compression } \Rightarrow\ \text{OSW relations,} \\ \delta_{\text{LE,upper}}(i) < 0 \ \Rightarrow\ \text{upper surface of strip } i \text{ in free expansion } \Rightarrow\ \text{PM relations,} \\ \delta_{\text{LE,lower}}(i) > 0 \ \Rightarrow\ \text{lower surface of strip } i \text{ in compression } \Rightarrow\ \text{OSW relations,} \\ \delta_{\text{LE,lower}}(i) < 0 \ \Rightarrow\ \text{lower surface of strip } i \text{ in free expansion } \Rightarrow\ \text{PM relations.} \end{cases} \tag{4.29}$$

[10] In this method, for simplicity, the leading edge of each strip is identified by a single triangular element, whereas in a more accurate representation it should consist of multiple triangles. The accuracy of the method therefore increases with the number of strips, at the expense of a higher computational cost.

4. Two different solutions are adopted for compression and expansion strips:

   - **Compression strip**:
     An oblique shock is assumed at the triangle corresponding to the leading edge, and the oblique-shock relations (4.22) and (4.25) are applied using δ_{LE}, M_∞, and γ to evaluate the pressure ratio p_2/p_1, the maximum deflection angle $\delta_{\max,\mathrm{LE}}$, and the post-shock Mach number M_2.
     Starting from the leading edge, all subsequent triangles along the strip are assumed to undergo an expansion process. The Prandtl–Meyer formulation is therefore applied starting from M_2, using the same numerical routine adopted in Section 4.2.1. In particular,

$$\begin{cases} \Delta\delta(i) = |\delta(i) - \delta_{\mathrm{LE}}|\,, \\ \nu(M_i) = \nu(M_2) + \Delta\delta(i), \end{cases} \tag{4.30}$$

     where $\nu(M)$ denotes the Prandtl–Meyer function.
     The pressure coefficient is then evaluated as

$$C_p(i) = \frac{2}{\gamma M_\infty^2}\left[\left(\frac{1+\dfrac{\gamma-1}{2}M_i^2}{1+\dfrac{\gamma-1}{2}M_\infty^2}\right)^{-\frac{\gamma}{\gamma-1}} - 1\right], \qquad \text{for } \delta_i \neq \delta_{\mathrm{LE}}, \tag{4.31}$$

     while the pressure coefficient at the leading edge is given by

$$C_{p,\mathrm{LE}} = \frac{2}{\gamma M_\infty^2}\left(\frac{p_2}{p_1} - 1\right). \tag{4.32}$$

     For each evaluated pressure coefficient C_p, an additional check is performed. Based on the quantities obtained from the oblique-shock relations, if either

$$(M_2 \leq 1) \quad \text{or} \quad (|\delta_{\mathrm{LE}}| \geq \delta_{\max,\mathrm{LE}}),$$

     the method is no longer valid, since the body is identified as blunt and a detached shock is expected.
     In this case, the user is prompted to modify the selected method, as illustrated in Fig. 4.23.

```
Scegli metodo:
  1) Newtonian
  2) Modified Newtonian
  3) Modified Newtonian + Prandtl-Meyer
  4) Tangent Wedge
  5) Tangent Wedge empirical
  6) Tangent Cone
  7) Tangent Cone empirical
  8) Inclinated Cone
  9) Delta Wing empirical
 10) OSU empirical
 11) Hankey flat-surface
 12) Dahlem-Buck
 13) Van Dyke Unified
 14) Shock Exspansion
Metodo (1-14): 14
Numero di strisce lungo l'apertura totale [default = 20]:
La separazione delle strisce va bene [default yes]? [y/n]:

[SHOCK-EXPANSION] Urto STACCATO al bordo d'attacco.
Metodo non applicabile (corpo blunt), scegli un altro metodo:

Scegli metodo:
```

Figure 4.23: MATLAB console, Section 4: Shock–Expansion option warning for a blunted cone configuration.

- **Expansion strip**:
  For expansion strips, the same solution as the Prandtl-Meyer method from the free stream is proposed:

$$\nu(M_i) = \nu(M_\infty) + |\delta(i)|, \tag{4.33}$$

  The Pressure Coefficient evaluation is the same as that proposed by (4.31) for all δ_i.

4.2.5 Dahlem-Buck

Once the method is selected, the user is prompted to choose whether to use the original version or a modification of the method. The latter introduces the Mach-dependent correction proposed in Section 3.1.10. An example is shown in Fig. 4.24

```
 12) Dahlem-Buck
 13) Van Dyke Unified
 14) Shock Exspansion
Metodo (1-14): 12

Scegli il modello di Dahlem-Buck da utilizzare:
  1) Dahlem-Buck empirico (originale)
     - Funziona bene a Mach elevati (M > 8-10)
     - Approssima tangent-cone a piccoli angoli e Newtoniano a grandi

  2) Dahlem-Buck modificato (Gentry)
     - Introdotto per includere la dipendenza dal Mach
     - Valido per 5 <= Mach <= 20

Inserisci la scelta (1-2): 2
```

Figure 4.24: MATLAB console, Section 4 : Dahlem-Buck option.

4.2.6 Inclined Cone

This section presents the evaluation of the circumferential angle ϕ, measured from the most windward generatrix, which is required for the correct application of the inclined cone method. Starting from the centroids C of each triangular surface element and the corresponding vertices P, the x-coordinate of the most advanced point is identified as $x_{\text{vertex}} = \min(P_x)$. In order to account for the cone inclination angle α[11], a local reference frame is defined with its origin located at the cone vertex. As a consequence, the centroid coordinates are translated according to:

$$\begin{cases} C_{x,\text{new}} = C_x - x_{\text{vertex}} \\ C_{y,\text{new}} = C_y - y_{\text{vertex}} \\ C_{z,\text{new}} = C_z - z_{\text{vertex}} \end{cases} \tag{4.34}$$

The circumferential angle ϕ represents the angular position of each triangular element around the cone axis and is defined in the plane orthogonal to the cone axis. The position of a centroid in this plane can be expressed in algebraic form as

$$C_{y,\text{new}} = r \sin\phi, \quad C_{z,\text{new}} = r \cos\phi. \tag{4.35}$$

In order to correctly identify ϕ over the interval $[-\pi, \pi]$, the MATLAB function `atan2(C_y,new, -C_z,new)` is employed. With this definition, $\phi = 0$ corresponds to the $-z$ direction[12] , and the resulting angular distribution is shown in Fig. 4.25.

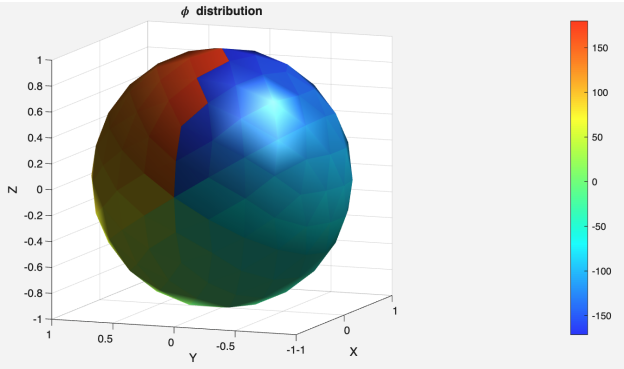

Figure 4.25: MATLAB console, Section 4 : Inclinated cone - ϕ distribution.

[11]The information of α is already included in the normals, so regardless of the incidence in eq. (3.23) , α is set to zero.

[12]Several tests were performed by varying the angular position $\phi = 0$ and analyzing the resulting C_p distributions. The most physically consistent result was obtained for $\phi = 0$ oriented in the $-z$ direction.

4.3 Numerical Tests and Validation Against Literatures

In this section, the main tests and validation activities conducted on different types of conical configurations are presented, referring to the results obtained from high-fidelity inviscid CFD analyses (Euler model) developed by Federica Portis et al.[10] at an altitude of 75 km and a free-stream Mach number $M_\infty = 6$.
In particular, the construction methods of the considered geometries are proposed, and the behavior of the different methods in terms of accuracy and computational cost is analyzed.

4.3.1 Geometrical Definition and CAD Generation in FreeCAD

Following the same geometrical characteristics proposed in [10], sixteen different blunted cone configurations, all sharing the same base radius $R_b = 3\,\text{m}$, were generated using *FreeCAD*.
All the blunted configurations were parameterized using two nondimensional ratios $\frac{R_b}{L}$, $\frac{R_c}{R_b}$, where R_c and L denote the nose curvature radius and the axial length of the cone, respectively. The geometrical properties of the sixteen different cone configurations are reported in Table 4.1.

Table 4.1: Geometrical parameters of the sixteen blunted cone configurations.

Geometry Name	R_b/L	R_c/R_b	L [m]	R_c [m]	R_b [m]
r0101	0.10	0.10	30	0.3	3.0
r0301	0.30	0.10	10	0.3	3.0
r0501	0.50	0.10	6	0.3	3.0
r07501	0.75	0.10	4	0.3	3.0
r0102	0.10	0.20	30	0.6	3.0
r0302	0.30	0.20	10	0.6	3.0
r0502	0.50	0.20	6	0.6	3.0
r07502	0.75	0.20	4	0.6	3.0
r0104	0.10	0.40	30	1.2	3.0
r0304	0.30	0.40	10	1.2	3.0
r0504	0.50	0.40	6	1.2	3.0
r07504	0.75	0.40	4	1.2	3.0
r0108	0.10	0.80	30	2.4	3.0
r0308	0.30	0.80	10	2.4	3.0
r0508	0.50	0.80	6	2.4	3.0
r07508	0.75	0.80	4	2.4	3.0

The solids were constructed as a revolution of a sketch about the symmetry axis (x-axis), and the mesh was generated using the *Netgen* option[13]. The procedure is shown in Fig. 4.26.

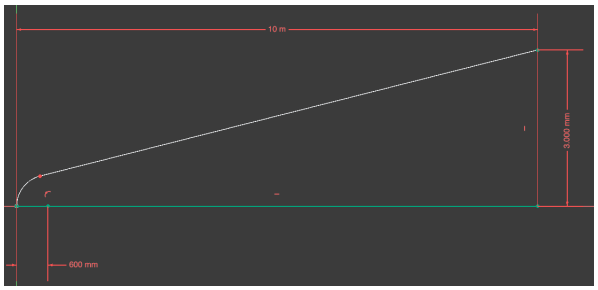

(a) 2D Sketch

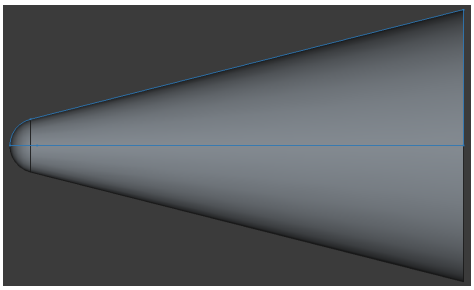

(b) Solid of revolution

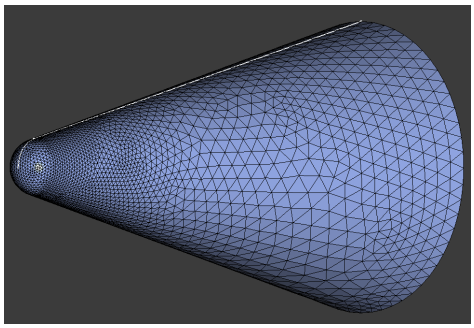

(c) Mesh

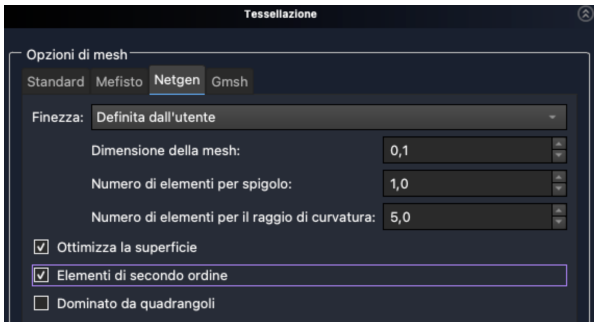

(d) Mesh generation option

Figure 4.26: Procedure adopted for geometry construction and mesh generation in *FreeCAD*.

For completeness, all the geometries tested and generated with this procedure are reported in Section 4.3.3.

4.3.2 Fast MATLAB Console

To test all the methods on the previously defined blunted cone configurations, a faster MATLAB console was developed in order to reduce the overall computational time.
Starting from the MATLAB console presented in Section 4.1, and after the selection of the full-body option, an automated loop tests all the available windward methods against the reference results obtained from external analyses for the selected geometry.

[13]The *Netgen* meshing parameters shown in Fig. 4.26d are the same for all geometries.

In this console, the user is only required to define the range of angle of attack α, select the shadow and base methods to be tested, and specify the names of the output files in which the results are stored. The selected configuration is then automatically evaluated for all the available windward methods.
A representative example of the console is shown in Fig. 4.27 and in Fig. 4.28.

```
============================================================
   ROMS - Reduced Order Models for Hypersonic configuration
        ( Mini Daniele - Politecnico di Torino / MBDA )
                      Fast Console
============================================================


--- Definizione condizioni di freestream ---
-------------------------------------------
Quota (m) [default 75000] < 80000: 75000
Numero di Mach M_∞ >5 [default 6]: 6

--- Seleziona un file STL dalla cartella corrente ---
-----------------------------------------------------
  1) r0101.stl
  2) r0102.stl

Seleziona la geometria (1-2)[default 1]: 1
>> Geometria selezionata: r0101.stl

--- Definizione Punto di Riferimento per il calcolo dei Momenti ---
--------------------------------------------------------------------
Si preferisce inserire il riferimento manualmente (m)
 o utilizzare il baricentro geometrico (g, default)? [g/m]: G

--- Identificazione della BASE ---
----------------------------------
Criteri correnti per definizione BASE:
Percentuale lunghezza corpo [default 90.0]: 90
Soglia normale n_x [default 0.85]: 0.85
La base va bene [default yes]? [y/n] y
>> Base confermata.

---Caratteristiche geometriche:---
-----------------------------------
Superficie di base S_ref = 28218446.085 mm^2
Lunghezza corpo L= 30000.00 mm
Apertura alare b = 5996.97 mm

La superficie di riferimento coincide con la superficie di base?
  1 - Sì  (default)
  2 - No, inserisci manualmente la superficie di riferimento Sref
Scelta (1-2): 1
>> Sref = S_base = 28218446.084757 mm^2

--- Definizione range di incidenza ---
-------------------------------------
Alpha minimo (deg) [default 0]: 0
Alpha massimo (deg) [default 20]: 20
Passo alpha (deg) [default 5]: 5
>> Range alpha: [0, 20] deg | passo = 5 deg
```

Figure 4.27: Command Window: Fast Console, Part 1

```
--- Metodo per Regione D'Ombra ---
-----------------------------------

================ SHADOW REGION METHODS ================
 1) Cp = 0 (Newtonian) ..........
 2) OSU Empirical ................ Suitable for blunt-body , developed for circular cylinder
 3) Mod.Newton + PM .............. PM Expansion from subsonic bowl / blunt-body configuratio
 4) Van Dike Unified ............. Suitable for thin aerodynamic configurations, valid for s
 5) Prandtl-Meyer Expansion from free stream
 6) Shock Expansion............. PM Expansion from leading edge  / sharp-nosed bodies with a
=======================================================
  1) Newtonian ( Cp = 0 )
  2) OSU blunt body empirical
  3) Modified Newtonian + Prandtl - Meyer
  4) Van Dike Unified
  5) Prandtl-Meyer from free stream
  6) Shock Expansion
Scegli metodo (1-6): 1

--- Metodo per la REGIONE DI BASE  ---
---------------------------------------
  Vuoi usare HIGH MACH BASE PRESSURES (HMBP) per la base?
   1) Sì, usa HMBP
   2) No, usa il metodo scelto per la regione d'ombra
Scelta (1–2)[default HMBP]: 1

--- Confronto CFD ---
---------------------------
Geometria testata: r0101.stl a M=6.0
File Disponibili
  1) r0101M6
  2) r0102M6
Seleziona la tabella CFD (1-2) [default 1]: 1
>> Tabella selezionata: r0101M6

>>Inizio Calcolo…

----------- Metodi testati  -----------
---------------------------------------
>> Metodo 1: Exposed: Newtonian ; Shadow: Cp = 0 (Newtonian) ;  Base: HMBP
>> Metodo 2: Exposed: Modified Newtonian ; Shadow: Cp = 0 (Newtonian) ;  Base: HMBP
>> Metodo 3: Exposed: Mod.Newton + Prandtl-Meyer ; Shadow: Cp = 0 (Newtonian) ;  Base: HMBP
>> Metodo 4: Exposed: Tangent Wedge ; Shadow: Cp = 0 (Newtonian) ;  Base: HMBP
>> Metodo 5: Exposed: Tangent Wedge Empirical ; Shadow: Cp = 0 (Newtonian) ;  Base: HMBP
>> Metodo 6: Exposed: Tangent Cone  ; Shadow: Cp = 0 (Newtonian) ;  Base: HMBP
>> Metodo 7: Exposed: Tangent Cone Empirical ; Shadow: Cp = 0 (Newtonian) ;  Base: HMBP
>> Metodo 8: Exposed: Inclinated Cone ; Shadow: Cp = 0 (Newtonian) ;  Base: HMBP
>> Metodo 9: Exposed: Delta Wing Empirical ; Shadow: Cp = 0 (Newtonian) ;  Base: HMBP
>> Metodo 10: Exposed: OSU Empirical ; Shadow: Cp = 0 (Newtonian) ;  Base: HMBP
>> Metodo 11: Exposed: Hankey Empirical ; Shadow: Cp = 0 (Newtonian) ;  Base: HMBP
>> Metodo 12: Exposed: Dahlem-Buck ; Shadow: Cp = 0 (Newtonian) ;  Base: HMBP
>> Metodo 13: Exposed: Van Dyke Unified ; Shadow: Cp = 0 (Newtonian) ;  Base: HMBP
---------------------------------------
Inserisci il nome del file: s_Newtonian_base_HMBP
>> Salvato Asave in Rismedi/r0101_s_Newtonian_base_HMBP.mat
>> Salvato Bsave in Rislocali/r0101_s_Newtonian_base_HMBP.mat

Vuoi lanciare un'altra configurazione [default y]? [y/n] n

==========================================
  ROMS terminato. Fine sessione.
==========================================
```

Figure 4.28: Command Window: Fast Console, Part 2.

The results output are in the following matrix format :

$$Asave(i,:) = [\bar{e}_{CL,i}, \bar{e}_{CD,i}, \bar{e}_{E,i}, \bar{e}_{CM,i}, t(i)]$$

$$Bsave(i,:) = [\vec{e}_{CL,i}, \vec{e}_{CD,i}, \vec{e}_{E,i}, \vec{e}_{CM,i},]$$

where i is the method index, t is the computational time, $\vec{e}_j$ is the vector of relative errors for each angle of attack, and $\bar{e}_j$ is the mean error over all angles of attack.

Computational Cost

Using the Asave results, a plot of the computational cost (i.e., the number of elements per second) associated with the various configurations chosen in full-body mode was generated and reported in Fig. 4.29.

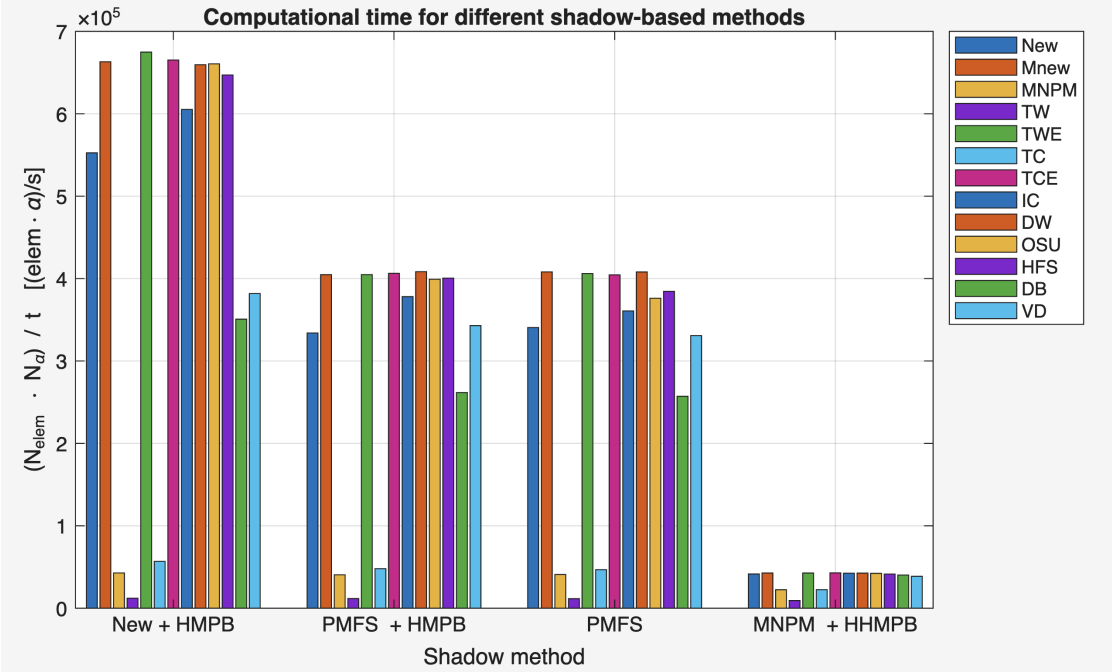

Figure 4.29: Fast Console: Computational Cost.

As shown in the graph, computation time depends strictly on the choice of shadow method and the implementation of the exposed ones; in particular, the Modified Newtonian plus Prandtl Meyer and the Tangent Wedge are the slowest shadow and exposed solutions, respectively. The reason may be related to the processing of the Prandtl-Meyer and oblique-shock relations applied to each surface element.
On the other hand, empirical methods, which consist of simple relations, yield results extremely quickly.
Nevertheless, to provide an estimate of the overall computational effort associated with this console, 16 conic geometries were tested, with mesh sizes ranging from 5000 to 55000 surface elements, using 13 different exposed methods, 4 shadow configurations, and 5 angles of attack, in less than 30 minutes.

4.3.3 Mean Relative Percentage Error Validation

A mean relative percentage error ($\bar{e}$) over the sixteen cones is first used to quantitatively assess the accuracy of the reduced-order aerodynamic models.
Using the Asave matrix data, different plots, as a function of the R_c/R_b ratio, for various lengths L and shadow methods, were generated to analyse C_L, C_D, and E separately[14].

Blunted Cone Geometries

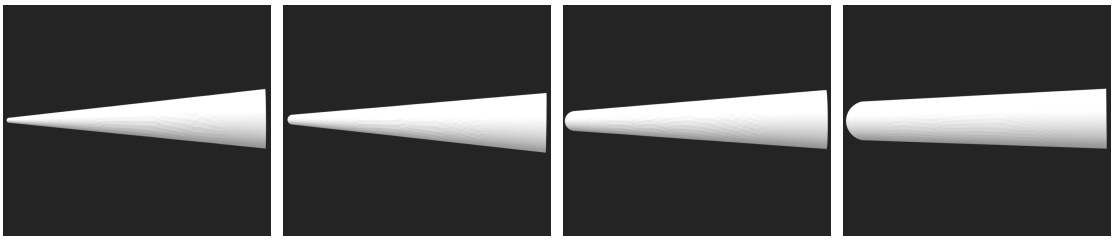

(a) r0101 **(b)** r0102 **(c)** r0104 **(d)** r0108

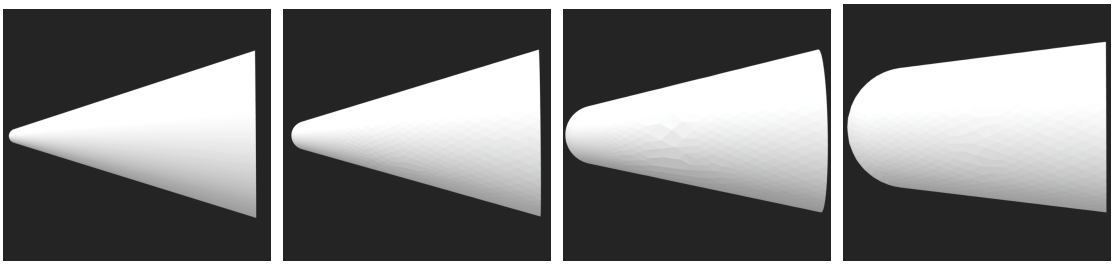

(e) r0301 **(f)** r0302 **(g)** r0304 **(h)** r0308

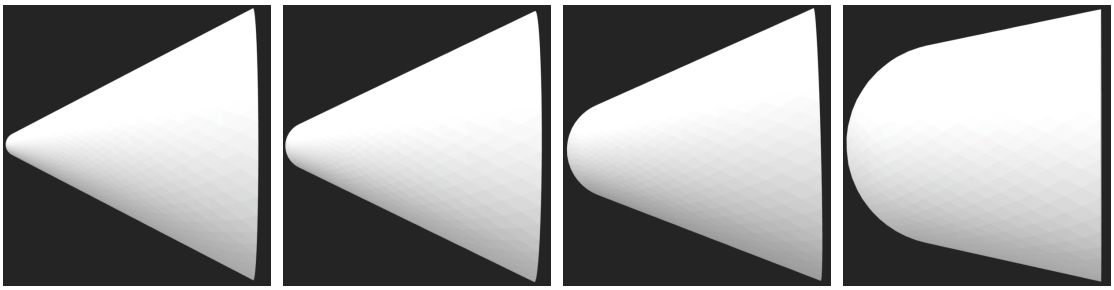

(i) r0501 **(j)** r0502 **(k)** r0504 **(l)** r0508

[14]Here, C_M is not covered because it is not available, and some methods are not analyzed. Shock-Expansion is not applicable to a blunted configuration; Inclined Cone is geometrically identical to Modified Newtonian, while Van Dike and OSU are known to perform on different configurations.

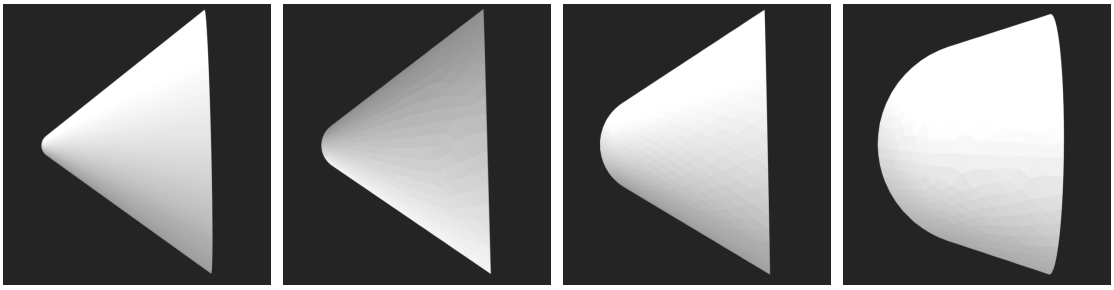

(a) r07501 **(b)** r07502 **(c)** r07504 **(d)** r07508

C_L Analysis

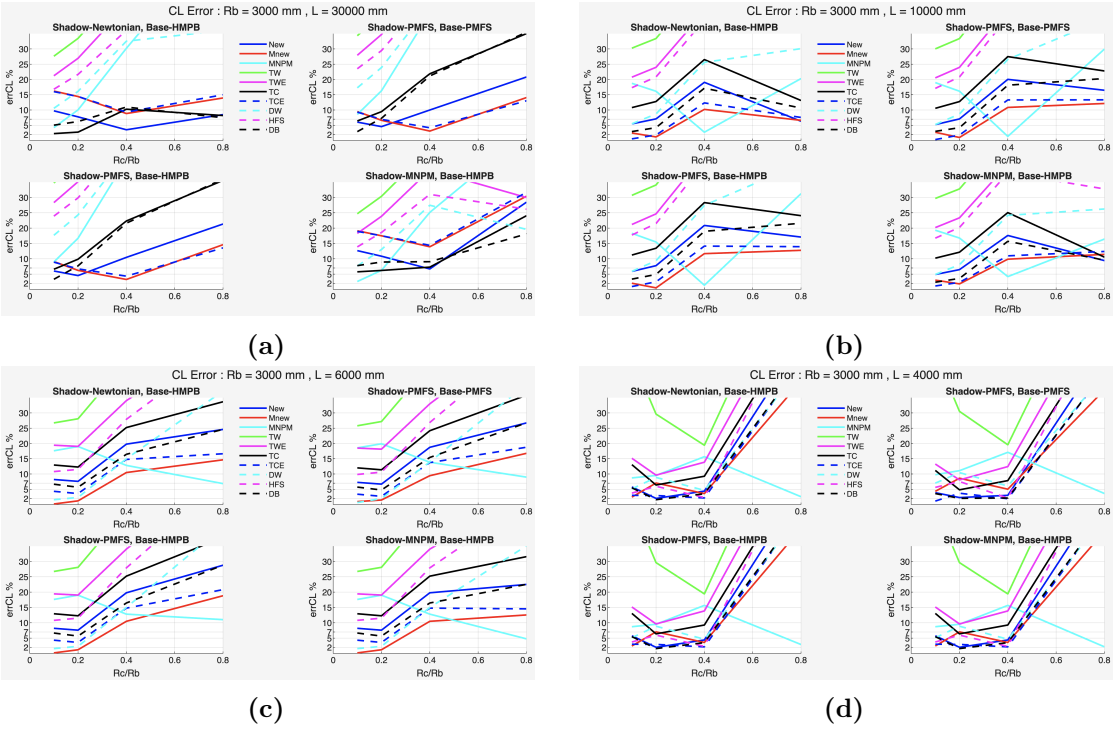

Figure 4.32: Mean Relative Percentage Error : C_L analysis. (a) L=30 m. (b) L=10 m. (c) L=6 m. (d) L=4 m.

As shown in Fig. 4.32, C_L is not influenced by the choice of the basic method, whereas it becomes more sensitive to the shadow method as the L/R_b ratio increases. This may be due to the increase in the shadow region for more elongated bodies as the incidence increases.
The methods developed for wedge-type bodies (tangent wedge and delta wing) tend to overestimate the coefficients for conical bodies; this is due to the use of an

oblique impact angle greater than the conical one, which is inappropriate in this treatment. On the other hand, the tangent cone and Dahlem-Buck methods are very precise for low R_c/R_b ratios, suggesting their applicability to cones with low local inclination angles.
Newtonian-type models suit the lift coefficient well, providing a good compromise across both exposed and shadow regions.

C_D Analysis

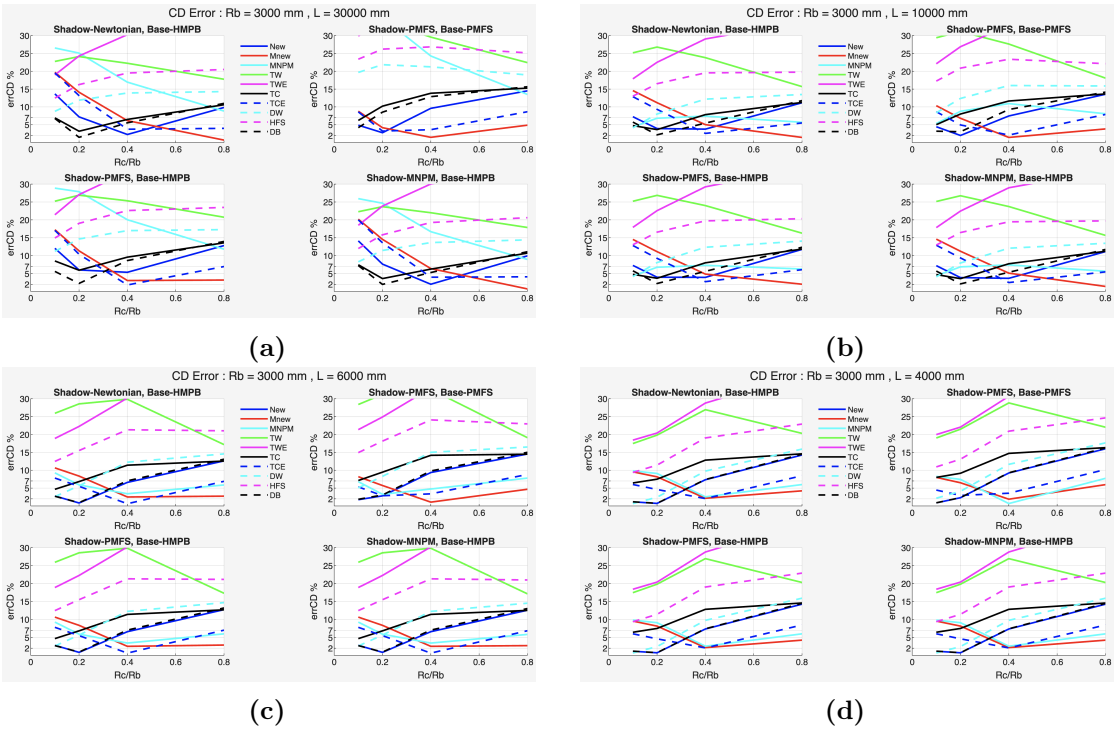

Figure 4.33: Mean Relative Percentage Error : C_D analysis. (a) L=30 m. (b) L=10 m. (c) L=6 m. (d) L=4 m.

As in the previous analysis, as the cone length decreases, the shadow methods converge towards a common trend for the individual methods presented. For high L/R_b ratios, the Newtonian and Modified Newtonian plus Prandtl–Meyer shadow solutions, together with the HMBP base solution, improve data convergence compared to the inviscid CFD results. Again, the exposed Tangent Cone and Dahlem–Buck methods provide the best agreement for low R_c/R_b ratios, while the Newtonian models approach the solution for higher values of this parameter.

E Analysis

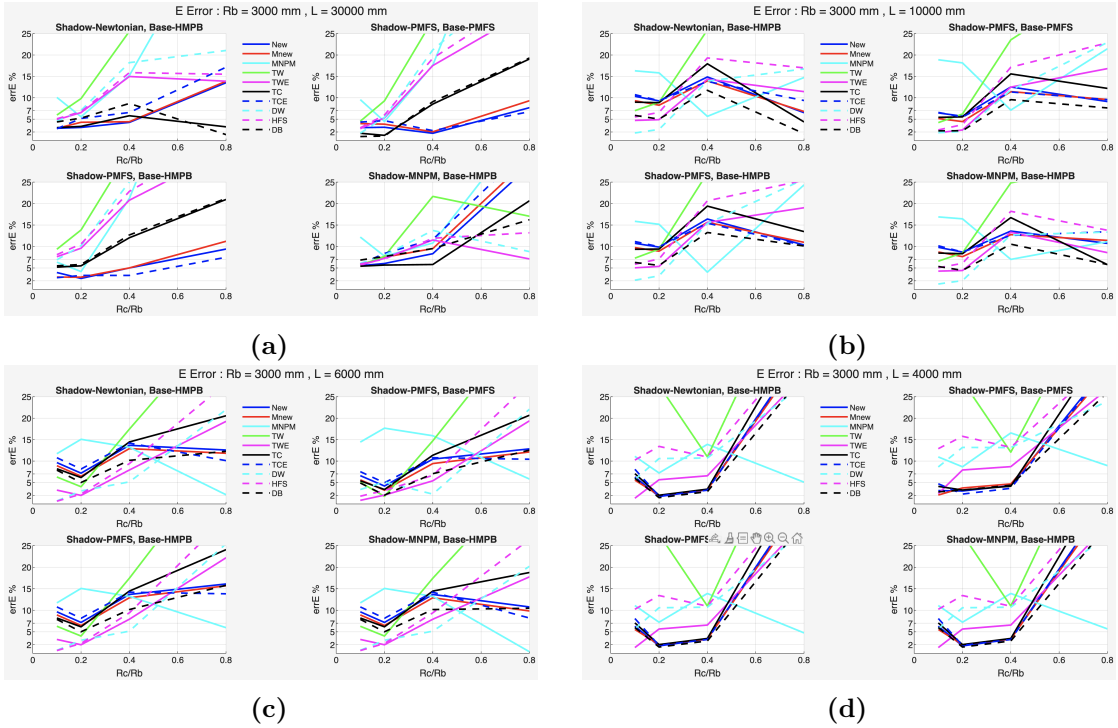

Figure 4.34: Mean Relative Percentage Error : E analysis. (a) L=30 m. (b) L=10 m. (c) L=6 m. (d) L=4 m.

Regarding efficiency, it is possible to observe that the choice of the basic method generally influences the accuracy of the results; in the cases tested, the Prandtl-Meyer free-stream (PMFS) method tends to improve the estimate as the R_c/R_b ratio decreases.
Again, the choice of the shadow method influences accuracy only as the L/R_b ratio increases, leading the PMFS method to be suitable for low R_c/R_b values, while the Newtonian model ($C_p = 0$) is recommended for higher ones.
Consistent with previous analyses, the tangent cone, Dahlem-Buck, and Newtonian models are the best exposed solutions for the preliminary aerodynamic characterization of conical geometries.

Best-Fitting Method Configurations

Fig. 4.35 presents, for completeness, the best-fitting method configurations for all the tested cones, reporting the best results for C_L, C_D , and the efficiency E.

```
>> Configurazione selezionata: R0101
Migliori configurazioni per CL:
1 : Tangent Cone + N + HBMP , MRAE = 2.271074 %
2 : Modified Newtonian plus Prandtl-Meyer + MNPM + HMBP , MRAE = 2.583860 %
3 : Dahlem-Buck + PMFS + PMFS , MRAE = 2.913211 %
Migliori configurazioni per CD:
1 : Dahlem-Buck + PMFS + PMFS , MRAE = 4.171184 %
2 : Newtonian + PMFS + PMFS , MRAE = 4.871266 %
3 : Dahlem-Buck + PMFS + HMBP , MRAE = 5.599327 %
Migliori configurazioni per E:
1 : Dahlem-Buck + PMFS + PMFS , MRAE = 0.933758 %
2 : Tangent Cone + PMFS + PMFS , MRAE = 1.694091 %
3 : Delta Wing empirical + PMFS + PMFS , MRAE = 1.719147 %
-------------------------------------------------------------------
>> Configurazione selezionata: R0102
Migliori configurazioni per CL:
1 : Tangent Cone + N + HBMP , MRAE = 2.753378 %
2 : Newtonian + PMFS + HMBP , MRAE = 4.518741 %
3 : Newtonian + PMFS + PMFS , MRAE = 4.551020 %
Migliori configurazioni per CD:
1 : Dahlem-Buck + N + HBMP , MRAE = 1.463131 %
2 : Dahlem-Buck + MNPM + HMBP , MRAE = 1.965370 %
3 : Dahlem-Buck + PMFS + HMBP , MRAE = 2.242444 %
Migliori configurazioni per E:
1 : Dahlem-Buck + PMFS + PMFS , MRAE = 1.049280 %
2 : Tangent Cone + PMFS + PMFS , MRAE = 1.217279 %
3 : Newtonian + PMFS + HMBP , MRAE = 2.564067 %
-------------------------------------------------------------------
>> Configurazione selezionata: R0104
Migliori configurazioni per CL:
1 : Modified Newtonian + PMFS + PMFS , MRAE = 3.096356 %
2 : Modified Newtonian + PMFS + HMBP , MRAE = 3.252437 %
3 : Newtonian + N + HBMP , MRAE = 3.524937 %
Migliori configurazioni per CD:
1 : Modified Newtonian + PMFS + PMFS , MRAE = 1.461293 %
2 : Tangent Cone empirical + PMFS + HMBP , MRAE = 1.808700 %
3 : Newtonian + MNPM + HMBP , MRAE = 2.012123 %
Migliori configurazioni per E:
1 : Newtonian + PMFS + PMFS , MRAE = 1.692171 %
2 : Modified Newtonian + PMFS + PMFS , MRAE = 2.042491 %
3 : Tangent Cone empirical + PMFS + PMFS , MRAE = 2.315728 %
-------------------------------------------------------------------
>> Configurazione selezionata: R0108
Migliori configurazioni per CL:
1 : Dahlem-Buck + N + HBMP , MRAE = 7.464553 %
2 : Tangent Cone + N + HBMP , MRAE = 8.187760 %
3 : Newtonian + N + HBMP , MRAE = 8.488032 %
Migliori configurazioni per CD:
1 : Modified Newtonian + N + HBMP , MRAE = 0.682136 %
2 : Modified Newtonian + MNPM + HMBP , MRAE = 0.701765 %
3 : Modified Newtonian + PMFS + HMBP , MRAE = 3.184915 %
Migliori configurazioni per E:
1 : Dahlem-Buck + N + HBMP , MRAE = 1.383211 %
2 : Tangent Cone + N + HBMP , MRAE = 3.203831 %
3 : Tangent Cone empirical + PMFS + PMFS , MRAE = 6.747009 %
-------------------------------------------------------------------
>> Configurazione selezionata: R0301
Migliori configurazioni per CL:
1 : Tangent Cone empirical + PMFS + PMFS , MRAE = 0.314840 %
2 : Tangent Cone empirical + N + HBMP , MRAE = 0.551009 %
3 : Tangent Cone empirical + PMFS + HMBP , MRAE = 0.946958 %
Migliori configurazioni per CD:
1 : Dahlem-Buck + PMFS + PMFS , MRAE = 3.186002 %
2 : Delta Wing empirical + MNPM + HMBP , MRAE = 4.090223 %
3 : Delta Wing empirical + N + HBMP , MRAE = 4.128317 %
Migliori configurazioni per E:
1 : Delta Wing empirical + MNPM + HMBP , MRAE = 1.263559 %
2 : Delta Wing empirical + N + HBMP , MRAE = 1.774829 %
3 : Tangent Wedge empirical + PMFS + PMFS , MRAE = 1.830554 %
-------------------------------------------------------------------
>> Configurazione selezionata: R0302
Migliori configurazioni per CL:
1 : Modified Newtonian + PMFS + HMBP , MRAE = 0.516556 %
2 : Modified Newtonian + PMFS + PMFS , MRAE = 0.996510 %
3 : Modified Newtonian + N + HBMP , MRAE = 1.180478 %
Migliori configurazioni per CD:
1 : Newtonian + PMFS + PMFS , MRAE = 1.980626 %
2 : Dahlem-Buck + MNPM + HMBP , MRAE = 2.107191 %
3 : Dahlem-Buck + N + HBMP , MRAE = 2.157426 %
Migliori configurazioni per E:
1 : Delta Wing empirical + MNPM + HMBP , MRAE = 2.062680 %
2 : Delta Wing empirical + PMFS + PMFS , MRAE = 2.118796 %
3 : Dahlem-Buck + PMFS + PMFS , MRAE = 2.287339 %
-------------------------------------------------------------------
>> Configurazione selezionata: R0304
Migliori configurazioni per CL:
1 : Modified Newtonian plus Prandtl-Meyer + PMFS + PMFS , MRAE = 1.353551 %
2 : Modified Newtonian plus Prandtl-Meyer + PMFS + HMBP , MRAE = 1.370981 %
3 : Modified Newtonian plus Prandtl-Meyer + N + HBMP , MRAE = 2.728460 %
Migliori configurazioni per CD:
1 : Modified Newtonian + PMFS + PMFS , MRAE = 1.431010 %
2 : Tangent Cone empirical + PMFS + PMFS , MRAE = 2.094111 %
3 : Tangent Cone empirical + MNPM + HMBP , MRAE = 2.482407 %

Migliori configurazioni per E:
1 : Modified Newtonian plus Prandtl-Meyer + PMFS + HMBP , MRAE = 4.026467 %
2 : Modified Newtonian plus Prandtl-Meyer + N + HBMP , MRAE = 5.654880 %
3 : Modified Newtonian plus Prandtl-Meyer + MNPM + HMBP , MRAE = 6.998564 %
-------------------------------------------------------------------
>> Configurazione selezionata: R0308
Migliori configurazioni per CL:
1 : Newtonian + N + HBMP , MRAE = 6.311363 %
2 : Modified Newtonian + N + HBMP , MRAE = 6.610109 %
3 : Tangent Cone empirical + N + HBMP , MRAE = 7.556962 %
Migliori configurazioni per CD:
1 : Modified Newtonian + MNPM + HMBP , MRAE = 1.400803 %
2 : Modified Newtonian + N + HBMP , MRAE = 1.429056 %
3 : Modified Newtonian + PMFS + HMBP , MRAE = 2.019752 %
Migliori configurazioni per E:
1 : Dahlem-Buck + N + HBMP , MRAE = 1.616846 %
2 : Tangent Cone + N + HBMP , MRAE = 4.348201 %
3 : Tangent Cone + MNPM + HMBP , MRAE = 5.778825 %
-------------------------------------------------------------------
>> Configurazione selezionata: R0501
Migliori configurazioni per CL:
1 : Modified Newtonian + N + HBMP , MRAE = 0.180682 %
2 : Modified Newtonian + PMFS + HMBP , MRAE = 0.180682 %
3 : Modified Newtonian + MNPM + HMBP , MRAE = 0.180682 %
Migliori configurazioni per CD:
1 : Newtonian + PMFS + PMFS , MRAE = 1.758073 %
2 : Dahlem-Buck + PMFS + PMFS , MRAE = 1.870328 %
3 : Delta Wing empirical + N + HBMP , MRAE = 2.611817 %
Migliori configurazioni per E:
1 : Hankey flat-surface + N + HBMP , MRAE = 0.649839 %
2 : Hankey flat-surface + PMFS + HMBP , MRAE = 0.649839 %
3 : Hankey flat-surface + MNPM + HMBP , MRAE = 0.649839 %
-------------------------------------------------------------------
>> Configurazione selezionata: R0502
Migliori configurazioni per CL:
1 : Modified Newtonian + N + HBMP , MRAE = 1.199697 %
2 : Modified Newtonian + PMFS + HMBP , MRAE = 1.199697 %
3 : Modified Newtonian + MNPM + HMBP , MRAE = 1.199697 %
Migliori configurazioni per CD:
1 : Newtonian + N + HBMP , MRAE = 0.836711 %
2 : Newtonian + PMFS + HMBP , MRAE = 0.836711 %
3 : Newtonian + MNPM + HMBP , MRAE = 0.836711 %
Migliori configurazioni per E:
1 : Tangent Wedge + PMFS + PMFS , MRAE = 1.767306 %
2 : Tangent Wedge empirical + N + HBMP , MRAE = 1.994988 %
3 : Tangent Wedge empirical + PMFS + HMBP , MRAE = 1.994988 %
-------------------------------------------------------------------
>> Configurazione selezionata: R0504
Migliori configurazioni per CL:
1 : Modified Newtonian + PMFS + PMFS , MRAE = 9.439397 %
2 : Modified Newtonian + N + HBMP , MRAE = 10.478268 %
3 : Modified Newtonian + PMFS + HMBP , MRAE = 10.478268 %
Migliori configurazioni per CD:
1 : Tangent Cone empirical + N + HBMP , MRAE = 0.628376 %
2 : Tangent Cone empirical + PMFS + HMBP , MRAE = 0.628376 %
3 : Tangent Cone empirical + MNPM + HMBP , MRAE = 0.628376 %
Migliori configurazioni per E:
1 : Delta Wing empirical + PMFS + PMFS , MRAE = 2.296343 %
2 : Delta Wing empirical + N + HBMP , MRAE = 5.154561 %
3 : Delta Wing empirical + PMFS + HMBP , MRAE = 5.154561 %
-------------------------------------------------------------------
>> Configurazione selezionata: R0508
Migliori configurazioni per CL:
1 : Modified Newtonian plus Prandtl-Meyer + MNPM + HMBP , MRAE = 4.758368 %
2 : Modified Newtonian plus Prandtl-Meyer + N + HBMP , MRAE = 6.849592 %
3 : Modified Newtonian plus Prandtl-Meyer + PMFS + PMFS , MRAE = 8.978377 %
Migliori configurazioni per CD:
1 : Modified Newtonian + MNPM + HMBP , MRAE = 2.711597 %
2 : Modified Newtonian + N + HBMP , MRAE = 2.747917 %
3 : Modified Newtonian + PMFS + HMBP , MRAE = 2.871442 %
Migliori configurazioni per E:
1 : Modified Newtonian plus Prandtl-Meyer + MNPM + HMBP , MRAE = 0.371094 %
2 : Modified Newtonian plus Prandtl-Meyer + N + HBMP , MRAE = 2.153265 %
3 : Modified Newtonian plus Prandtl-Meyer + PMFS + PMFS , MRAE = 5.813932 %
-------------------------------------------------------------------
>> Configurazione selezionata: R07501
Migliori configurazioni per CL:
1 : Tangent Cone empirical + PMFS + PMFS , MRAE = 1.127776 %
2 : Modified Newtonian + N + HBMP , MRAE = 2.436846 %
3 : Modified Newtonian + PMFS + HMBP , MRAE = 2.436846 %
Migliori configurazioni per CD:
1 : Delta Wing empirical + N + HBMP , MRAE = 0.663977 %
2 : Delta Wing empirical + PMFS + HMBP , MRAE = 0.663977 %
3 : Delta Wing empirical + MNPM + HMBP , MRAE = 0.663977 %
Migliori configurazioni per E:
1 : Tangent Wedge empirical + N + HBMP , MRAE = 1.345112 %
2 : Tangent Wedge empirical + PMFS + HMBP , MRAE = 1.345112 %
3 : Tangent Wedge empirical + MNPM + HMBP , MRAE = 1.345112 %
-------------------------------------------------------------------
>> Configurazione selezionata: R07502
Migliori configurazioni per CL:
1 : Dahlem-Buck + N + HBMP , MRAE = 1.584511 %
2 : Dahlem-Buck + PMFS + HMBP , MRAE = 1.584511 %
3 : Dahlem-Buck + MNPM + HMBP , MRAE = 1.584511 %
Migliori configurazioni per CD:
1 : Newtonian + N + HBMP , MRAE = 0.716436 %
2 : Newtonian + PMFS + HMBP , MRAE = 0.716436 %
3 : Newtonian + MNPM + HMBP , MRAE = 0.716436 %
Migliori configurazioni per E:
1 : Dahlem-Buck + N + HBMP , MRAE = 1.461785 %
2 : Dahlem-Buck + PMFS + HMBP , MRAE = 1.461785 %
3 : Dahlem-Buck + MNPM + HMBP , MRAE = 1.461785 %
-------------------------------------------------------------------
>> Configurazione selezionata: R07504

Migliori configurazioni per CL:
1 : Tangent Cone empirical + PMFS + PMFS , MRAE = 1.907152 %
2 : Hankey flat-surface + PMFS + PMFS , MRAE = 2.103347 %
3 : Tangent Cone empirical + N + HBMP , MRAE = 2.139880 %
Migliori configurazioni per CD:
1 : Modified Newtonian plus Prandtl-Meyer + PMFS + PMFS , MRAE = 0.681027 %
2 : Modified Newtonian + PMFS + PMFS , MRAE = 1.894119 %
3 : Tangent Cone empirical + N + HBMP , MRAE = 2.068920 %
Migliori configurazioni per E:
1 : Dahlem-Buck + N + HBMP , MRAE = 2.875254 %
2 : Dahlem-Buck + PMFS + HMBP , MRAE = 2.875254 %
3 : Dahlem-Buck + MNPM + HMBP , MRAE = 2.875254 %
-------------------------------------------------------------------
>> Configurazione selezionata: R07508
Migliori configurazioni per CL:
1 : Modified Newtonian plus Prandtl-Meyer + MNPM + HMBP , MRAE = 2.154840 %
2 : Modified Newtonian plus Prandtl-Meyer + N + HBMP , MRAE = 2.558931 %
3 : Modified Newtonian plus Prandtl-Meyer + PMFS + HMBP , MRAE = 2.909097 %
Migliori configurazioni per CD:
1 : Modified Newtonian + MNPM + HMBP , MRAE = 4.230211 %
2 : Modified Newtonian + N + HBMP , MRAE = 4.234839 %
3 : Modified Newtonian + PMFS + HMBP , MRAE = 4.237520 %
Migliori configurazioni per E:
1 : Modified Newtonian plus Prandtl-Meyer + PMFS + HMBP , MRAE = 4.753390 %
2 : Modified Newtonian plus Prandtl-Meyer + N + HBMP , MRAE = 5.083444 %
3 : Modified Newtonian plus Prandtl-Meyer + MNPM + HMBP , MRAE = 5.677473 %
-------------------------------------------------------------------
```

Figure 4.35: Best-Fitting Method Configurations

4.3.4 Relative Percentage Error Single Method Analysis

After the initial mean-error analysis, a more detailed comparison of the best-fitting models across the cones was carried out. Based on the results stored in the Bsave matrix, several plots were produced to examine the behaviour of the individual exposed models as functions of the angle of attack α, the length L, and the R_c/R_b ratio.

Dahlem-Buck

The solution proposed by the Dahlem-Buck model is among the best approximations for estimating the aerodynamic coefficients (particularly CD) of cones with low R_c/R_b ratios. Its empirical formulation, which combines the Newtonian and tangent cone approaches, makes it extremely versatile and stable even for various incidence angles α and lengths L, as shown in Fig. 4.36.

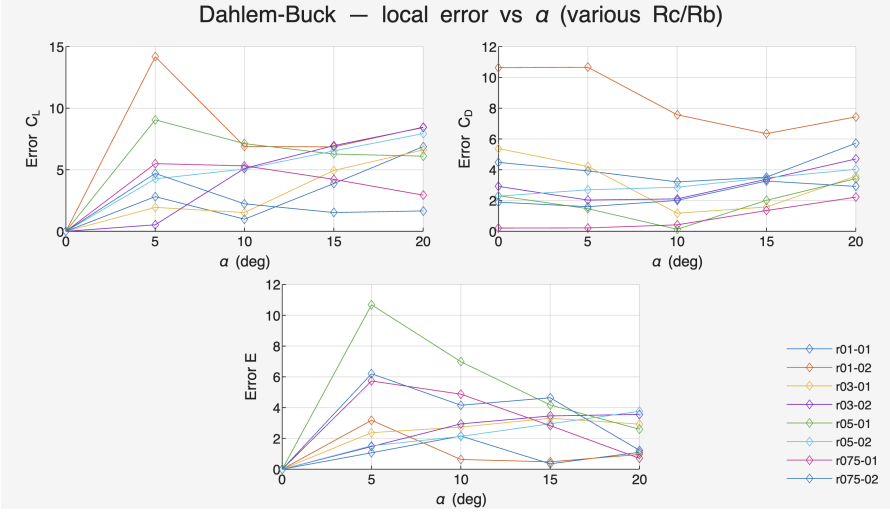

Figure 4.36: Relative Percentage Error : Dahlem-Buck & PMFS

Tangent Cone

The Tangent Cone model is also well suited to cones with low R_c/R_b ratios, although its accuracy tends to decrease as the angle of attack increases. This behaviour may be attributed to the loss of symmetry of the body when inclined with respect to the freestream. Nevertheless, the improved accuracy observed at higher incidence angles can be associated with the correction introduced by the Modified Newtonian method.

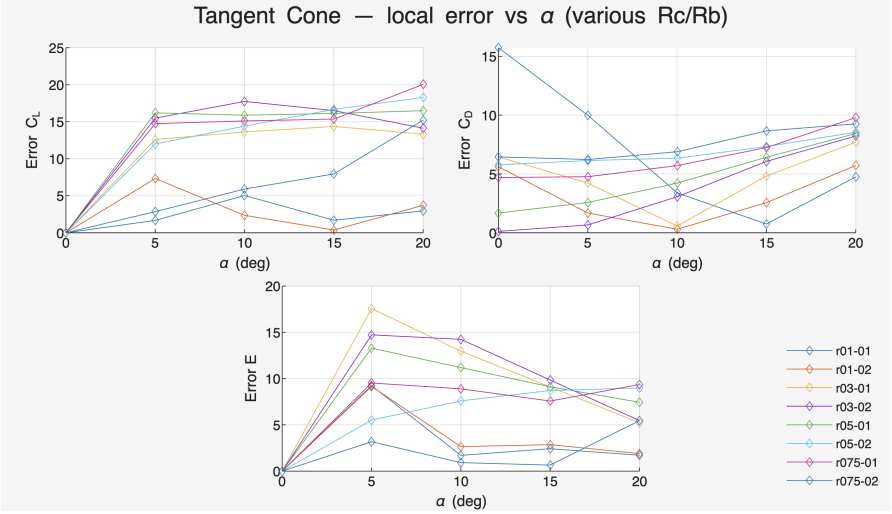

Figure 4.37: Relative Percentage Error : Tangent Cone & Newtonian & HMBP

Modified Newtonian

Newtonian models provide the best agreement for blunted cone configurations with high R_c/R_b ratios. In particular, they show an excellent fit for the C_D coefficient, while the accuracy of C_L and efficiency (E) appears to improve as the angle of attack increases. This suggests their suitability for configurations characterized by large local inclination angles.

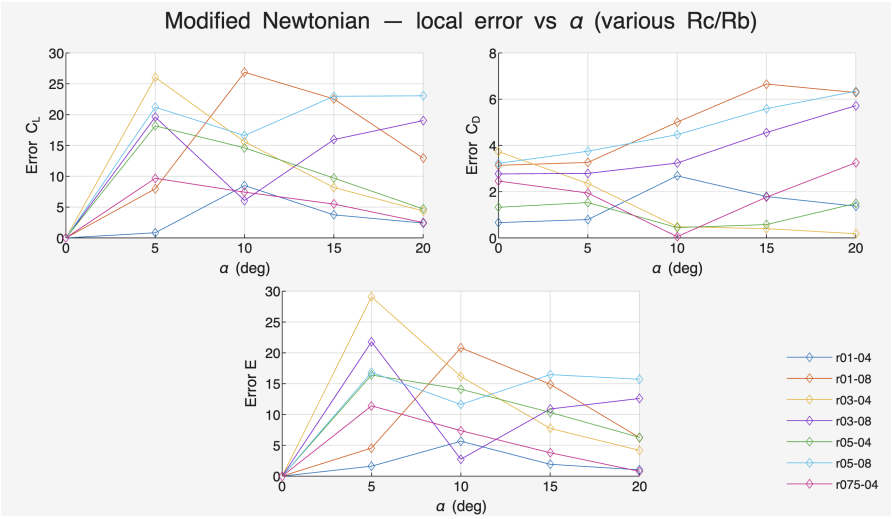

Figure 4.38: Relative Percentage Error : Modified Newtonian & PMFS

Chapter 5

CFD Analysis and Model Selection

This chapter describes the high-fidelity CFD analysis conducted on various hypersonic configurations and their comparison with the reduced-order models illustrated in Chapter 4.
In particular, the aerodynamic force and moment coefficients obtained from viscous simulations of the HB-2 and HGV-like configurations at different Mach numbers are analyzed, as well as the impact of high-temperature effects relative to the adopted physical models.
Starting with the main modeling and numerical choices (e.g., mesh discretization, turbulence models, and numerical schemes, ...), a comparative analysis is performed to identify the reduced-order model combinations that best reproduce the reference CFD results.
For confidentiality reasons, the geometric details and aerodynamic characteristics scale of the HGV configuration are not reported, nor is the name of the solver used for the high-fidelity simulations.

5.1 Tested Configurations

5.1.1 Hypervelocity Ballistic Model 2 (HB-2)

The HB-2 configuration, introduced in 1960, is an axisymmetric blunt cone-cylinder designed with a 25° nose-cone half-angle and a 10° tail flare. It serves as a standard model for correlating data from supersonic and hypersonic wind tunnel tests.
The original geometry shown in Fig. 5.1a was assumed with a 500 mm diameter and reconstructed as a solid of revolution from a 2D sketch about the symmetry axis (x-axis) in FreeCAD. The STEP file was then exported and processed in ANSA.

5.1.2 Hypersonic Glide Vehicle (HGV)

Hypersonic Glide Vehicles (HGVs) are maneuverable boost-glide systems that typically operate at altitudes up to 120 km and are generally unpowered.
The configuration is first accelerated to the designated release altitude and velocity using a booster. After separation, the vehicle re-enters the atmosphere and glides in a controlled manner, typically via a pull-up maneuver that stabilizes its trajectory. At this stage, the lift generated during the glide phase allows the vehicle to follow a maneuverable and adaptable trajectory that differs significantly from that of a conventional ballistic body.
In this analysis, a reference HGV-like geometry was provided by MBDA and subsequently processed in ANSA using the routine described in the following section.
For confidentiality reasons, the actual geometry used will not be shown; instead, a similar geometry (HTV-2), analyzed in 'Modeling the Performance of Hypersonic Boost-Glide Missiles' by Cameron L. Tracy and David Wright [11], will be presented (Fig. 5.1b).

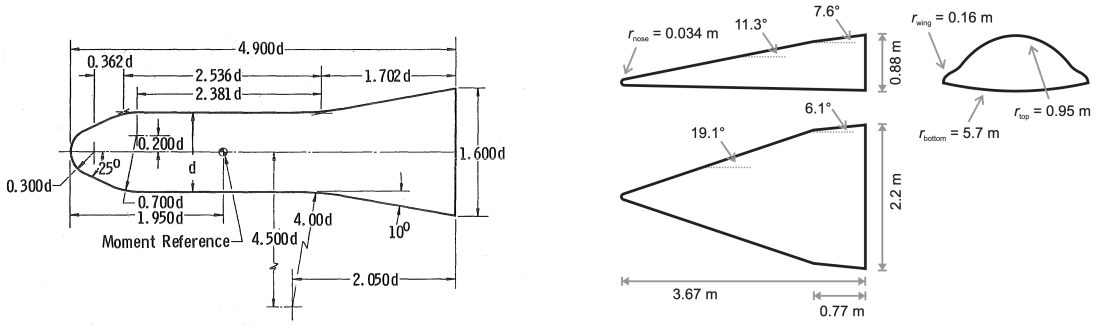

Figure 5.1: Tested Geometries. (a) HB2 Geometry. (b) HTV2 Geometry.

5.2 Computational Mesh Generation

The surface and volume mesh generation process was performed using BetaCAE's ANSA Tool and is identical across all analyzed configurations; consequently, only the HB-2 case will be presented.

5.2.1 Surface Mesh Generation

The STEP file is first imported into ANSA and, after surface cleaning, reconstructed using a multitude of triangular mesh elements. The distribution and size of the

elements are managed differently across the different PIDs (Property IDs; such as Base, Nose, and Body) through different distributions of Hot Points across the various Coons (in green, Fig.5.2). In particular, a refinement is applied to curved surfaces to improve mesh quality.

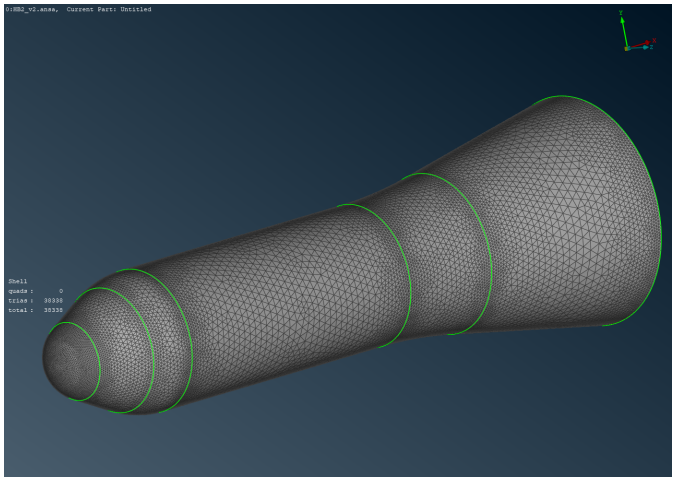

Figure 5.2: HB2 Surface Mesh.

To reduce simulation computational cost, the number of surface elements is reduced to approximately 40.000, even at the expense of analysis accuracy. The mesh is then exported in STL format for processing in the MATLAB Console.

5.2.2 Volume Mesh Generation

The external domain, provided by MBDA, is a blunted conical surface triangular mesh, with the half-opening angle of the inclined cone equal to the Mach cone angle obtained for M = 2.
By convention, the surface is scaled to ensure a distance of 20 body lengths between the body base and the domain bottom.
The volume mesh is built via the Tetrarapids routine, which discretizes the domain into a multitude of tetrahedral elements, with dimensions ranging from the size-box elements' lengths to the external surface triangles, with a growth rate of 1.2.
The Volume Mesh of the HB-2 configuration is reported in Fig.5.3.

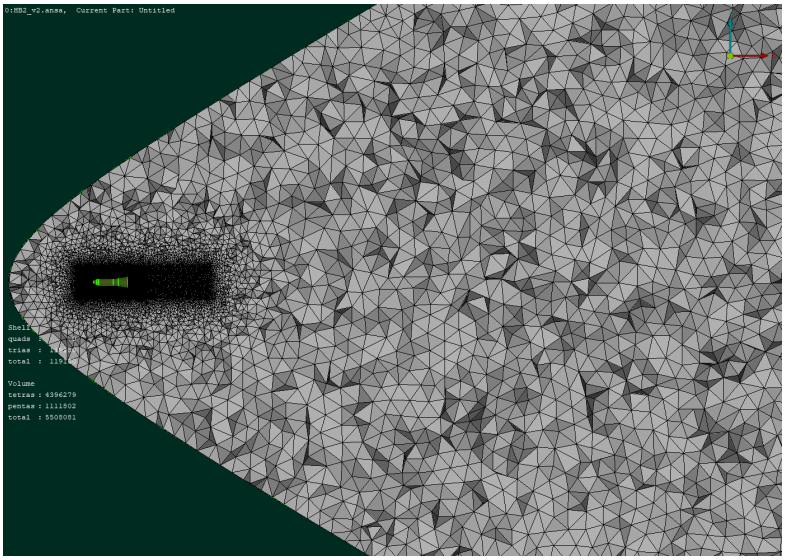

Figure 5.3: HB2 Volume Mesh.

Size Box

To better capture the flow phenomena around the body and in the wake region, two different Size-boxes were constructed. In particular, as illustrated in Fig.5.4, two different refinement laws were defined, with a greater refinement around the body to capture the shock wave.

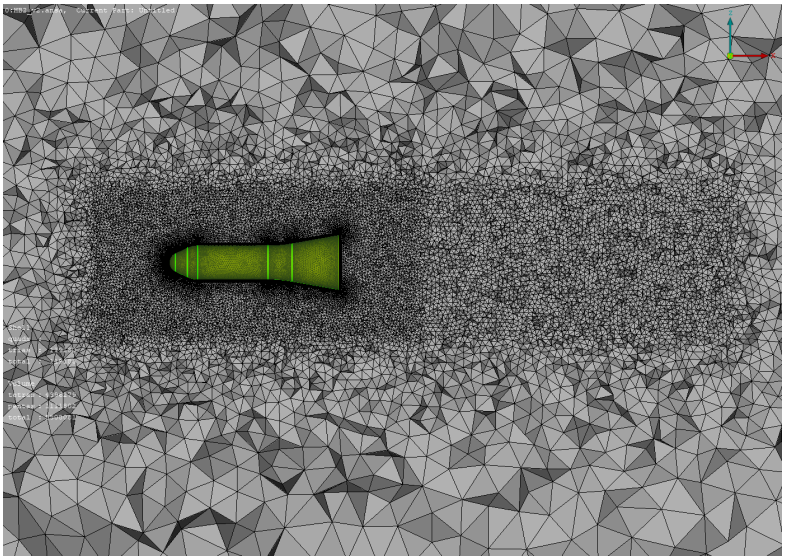

Figure 5.4: HB2 Size-Box.

Layers

To capture the gradients of the fluid-dynamic variables and the boundary-layer characteristics, several layers are constructed around the body volume, with refinement near the surface.
The height of the first cell, or first layer, and the general boundary layer height (total overall height of the layers) were defined through a target non-dimensional wall distance y^+, evaluated using a flat-plate boundary layer assumption as a function of freestream velocity, density, dynamic viscosity, reference length, and a target value of $y^+ = 1$.
The freestream properties are evaluated using the atomsisa routine and, as a consequence, different layer configurations were generated for different freestream Mach numbers.

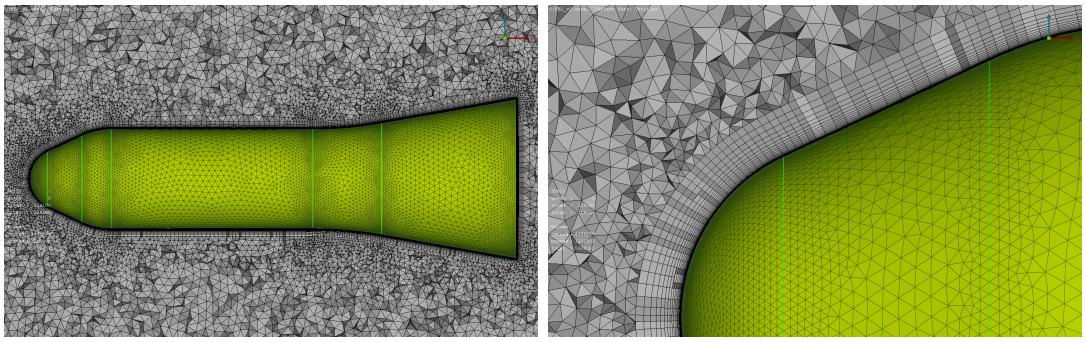

Figure 5.5: HB2 Layers.

5.3 Model Selection Process

The ROM selection process operates via the MATLAB Fast Console presented in Chapter 3.
Once the CFD results are available, all models are tested in both the full-body and body-wing configurations (for a defined body-wing separation rate), and a ranking of the best combination for each aerodynamic coefficient is generated.
Subsequently, an overall ranking is established by identifying the best combination of methods based on the average relative error computed across all aerodynamic coefficients, defined as

$$\bar{e}_i = \frac{\bar{e}_{CL,i} + \bar{e}_{CD,i} + \bar{e}_{CM,i} + \bar{e}_{E,i}}{4} \tag{5.1}$$

5.4 CFD Analysis (Without High-Temperature Effects)

A first analysis is performed under the assumption of a calorically and thermally perfect gas ($\gamma = 1.4$), neglecting thermochemical nonequilibrium effects and dissociation phenomena, on the HB-2 and HGV configurations for different Mach numbers at an altitude of 30 km.

5.4.1 Modeling & Numerical Choices

For this analysis, the following boundary conditions were adopted:

- **Domain Freestream** ⇒ Farfield, M_∞, ρ_∞, T_∞
- **Domain Bottom** ⇒ Supersonic outflow
- **Body** ⇒ Viscous wall, turbulent, T_∞

According to the solver's best practices, the k-ω turbulence model with SST formulation was employed, and an upwind scheme with first-order spatial accuracy was used for the spatial discretization of the flow steady-state equations, with a CFL number equal to 1.
After residual convergence was achieved, the C_L, C_D, and C_M coefficients were compared with ROMs results to select the best-fitting configuration methods.
For consistency with the CFD analysis the freestream conditions for the console were evaluated with the Matlab function atomoscoesa(h).

5.4.2 M_∞=6

HB-2

As shown in Table.5.1, Newtonian(N,MNPM,MN) and empirical models like the Tangent Cone(TC,TCE) and Dahlem-Buck(DB) best approximate CFD solutions for a blunt cone-cylinder at five angles of attack ($\alpha = 0°, 5°, 10°, 15°, 20°$). For shadow regions, Modified Newtonian + Prandtl-Meyer (MNPM), Prandtl-Meyer from freestream (PMFS), and the classical Newtonian approach (N) give the most accurate results, while the choice of base flow model mainly affects the drag coefficient C_D. Overall, the ROMs show good agreement with the high-fidelity CFD results, even in the absence of viscous corrections, since pressure forces dominate over viscous contributions. Figure 5.6 shows, as an example, the Newtonian method for exposed elements, the MNPM approach for shadowed regions, and HBMP for the base flow, yielding average errors of $\text{err}_{C_L} = 2.56\%$, $\text{err}_{C_D} = 2.88\%$, $\text{err}_E = 1.87\%$, and $\text{err}_{C_M} = 21.44\%$.

Table 5.1: HB-2: Best Methods for $M_\infty = 6$.

Rank	E-Body	S-Body	Base	$\bar{e}_{CL}\%$	$\bar{e}_{CD}\%$	$\bar{e}_{E}\%$	$\bar{e}_{CM}\%$
1)	TCE	N	HMBP	3.83	3.18	2.78	17.28
2)	N	MNPM	HMBP	2.56	2.88	1.87	21.44
3)	TCE	MNPM	HMBP	4.60	3.21	2.30	18.95
4)	TCE	MNPM	MNPM	5.21	1.93	4.90	18.95
5)	MN	N	HMBP	4.25	5.82	3.45	17.97
6)	DB	MNPM	HMBP	4.93	4.66	1.72	21.53
7)	N	MNPM	MNPM	2.32	6.11	3.02	21.44
8)	MN	MNPM	MNPM	6.67	2.54	4.33	19.64
9)	MN	PMFS	PMFS	7.93	1.41	8.76	15.51
10)	MN	MNPM	HMBP	6.06	5.85	2.23	19.64

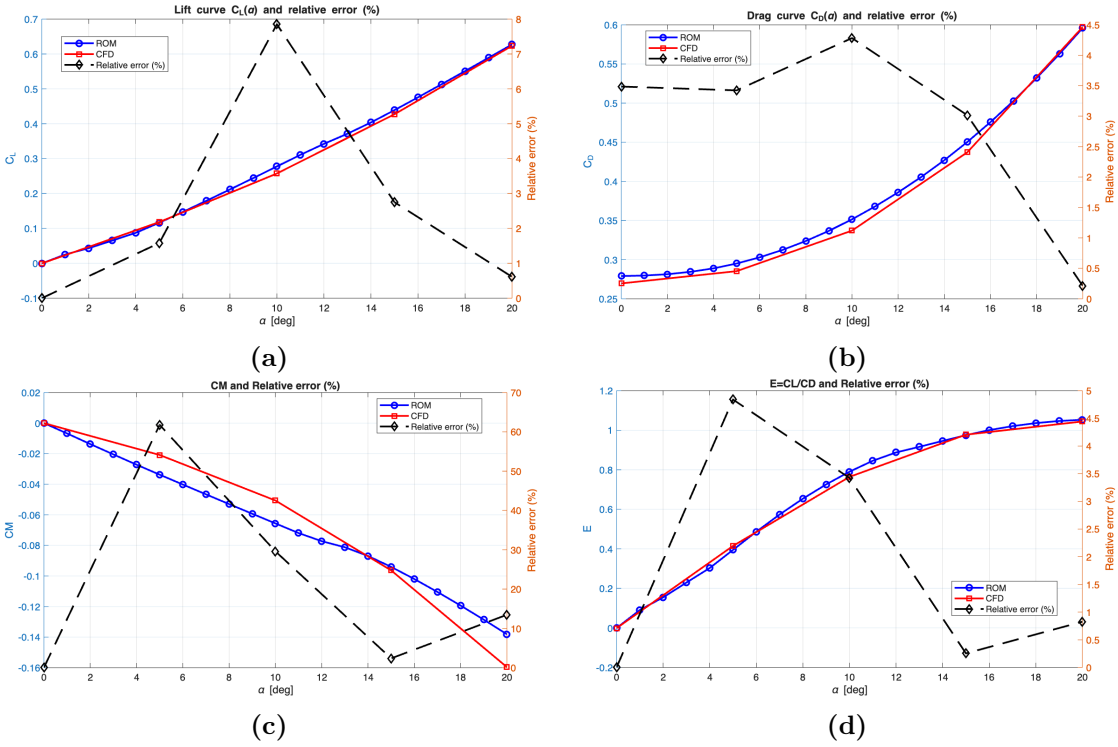

Figure 5.6: HB-2 Mean Relative Percentage Error : $M_\infty = 6$, 30 km. (a) CL. (b) CD. (c) CM. (d) $E = \frac{CL}{CD}$.

The relative error on C_M is higher for all combinations because the CFD reference values are near zero. However, the overall trend remains consistent with the high-fidelity solution.

HGV

For the HGV configuration, a parametric analysis was performed by varying the body-wing separation ratio to identify the optimal configuration.
The analysis revealed that using different models for the wing and fuselage components significantly improved solution accuracy, highlighting the influence of the body on method choice.
In particular, it was found that for the blunted-type fuselage bodies, the Tangent Cone(TC,TCE) and Newtonian-type (N,MNPM,MN)models provided the best solutions, while for the wing, the Delta Wing(DW), Van Dike(VD), Hankey flat(HFS), and Tangent Wedge(TW,TWE) models provided the best fits. For this configuration, a body-wing separation of 20% of the wingspan b was chosen.
The HGV best fitting method's rank is reported in Table 5.2.

Table 5.2: HGV: Best Methods for $M_\infty = 6$.

Rank	E-Wing	E-Body	S-Wing	S-Body	Base	$\bar{e}_{CL}\%$	$\bar{e}_{CD}\%$	$\bar{e}_E\%$	$\bar{e}_{CM}\%$
1)	DW	MNPM	PMFS	MNPM	MNPM	2.82	5.25	4.70	2.83
2)	DW	MNPM	PMFS	PMFS	PMFS	3.41	4.01	7.31	2.13
3)	HFS	MNPM	PMFS	MNPM	MNPM	2.86	2.75	4.41	7.54
4)	TWE	MNPM	N	MNPM	HMBP	2.21	7.03	5.69	3.23
5)	TWE	MNPM	N	N	HMBP	2.35	7.03	6.41	3.70
6)	TWE	MNPM	N	PMFS	HMBP	2.24	5.54	8.35	3.71
7)	VD	MNPM	N	N	HMBP	2.15	4.15	6.25	7.37
8)	DW	TWE	PMFS	MNPM	MNPM	3.07	5.91	7.62	4.00
9)	HFS	MNPM	N	PMFS	HMBP	1.97	7.99	7.32	3.41
10)	VD	MNPM	N	MNPM	HMBP	2.53	4.69	5.54	7.95

In this case, the best shadow solution for the wing element is provided by the PMFS model, while the body solution is obtained using MNPM. As in the previous cases, the base selection generally influences the Cd coefficient.
A representative case analysis is reported in Fig.5.7 where 9 different angles of attack ($\alpha = -20°, -15°, -10°, -5°, 0°, 5°, 10°, 15°, 20°$) were tested using Delta Wing and PMFS for the wing and MNPM for the body, yielding average errors of $\text{err}_{C_L} = 2.82\%$, $\text{err}_{C_D} = 5.25\%$, $\text{err}_E = 4.7\%$, and $\text{err}_{C_M} = 2.83\%$.
Despite the excellent accuracy of the methods for this simulation, a divergence between the two solutions is observed at large angles of attack in the estimation of CL and CD.

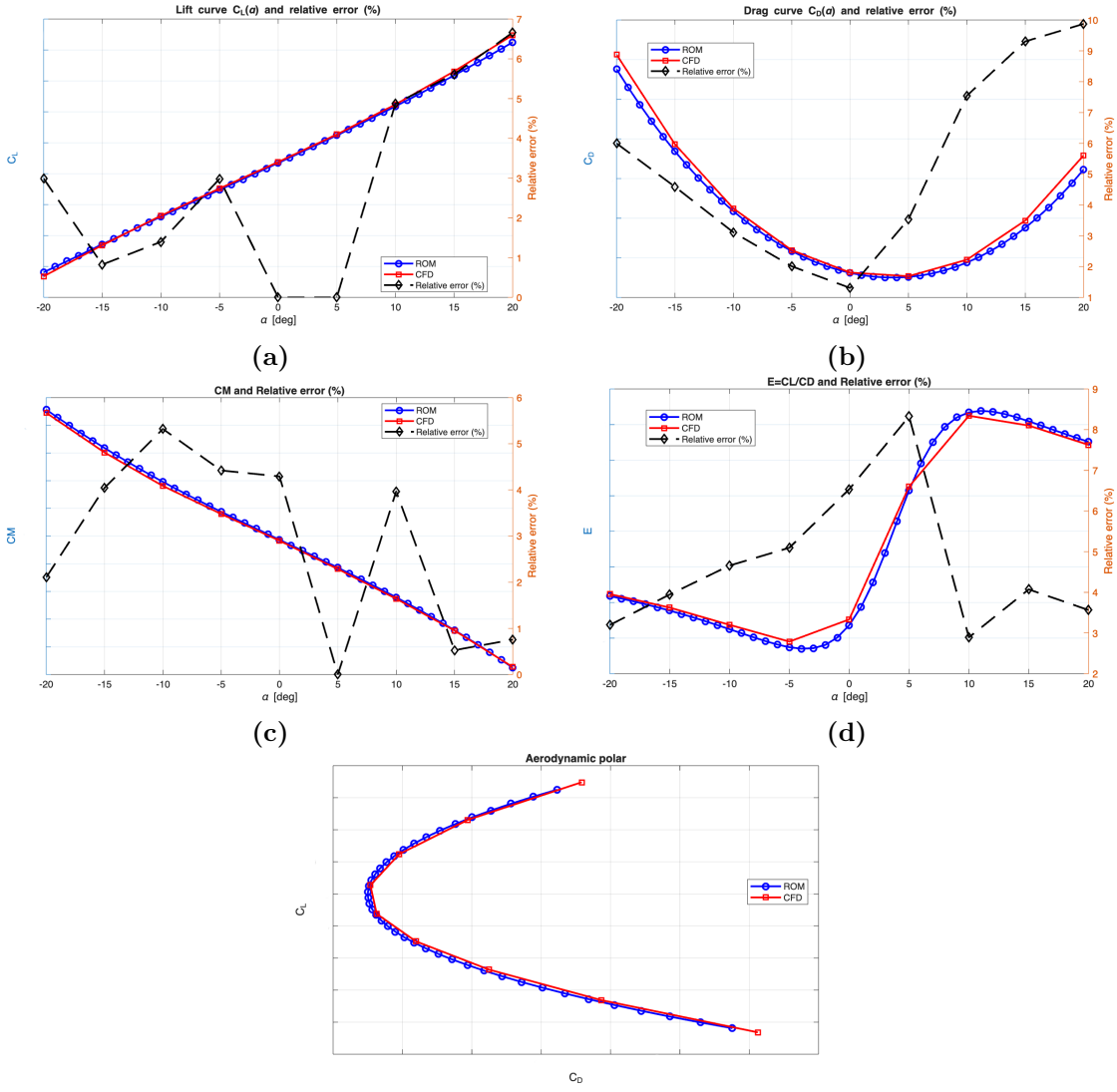

Figure 5.7: HGV Mean Relative Percentage Error : $M_\infty = 6$, 30 km. (a) CL. (b) CD. (c) CM. (d) $E = \frac{CL}{CD}$. (e) Polar CL-CD

5.4.3 M_∞=10

HB-2

A second ranking, for the CFD analysis at $M = 10$ on the HB-2 configuration, is shown in Table 5.3. The Newtonian and Tangent Cone models, as well as those empirically combining the two (such as DB), remain the best choice for exposed surfaces. In this case, the choice of the shadow method leans towards MNPM, which is the only method that estimates the position of the subsonic bowl and predicts a lower initial expansion Mach than that predicted by Prandtl-Meyer free expansion from M_∞ (PMFS).
It is also possible to note a limited influence of the base method on the coefficients; this can be justified because, as the free-stream Mach number increases, the Cp evaluated on the elements of the base region progressively tends to zero.

Table 5.3: HB2: Best Methods for $M_\infty = 10$.

Rank	E-Body	S-Body	Base	$\bar{e}_{CL}\%$	$\bar{e}_{CD}\%$	$\bar{e}_{E}\%$	$\bar{e}_{CM}\%$
1)	TCE	MNPM	HMBP	6.21	4.01	5.08	37.73
2)	MN	MNPM	HMBP	7.59	3.30	5.27	37.24
3)	MN	MNPM	MNPM	7.70	3.94	6.22	37.24
4)	TCE	MNPM	MNPM	6.33	5.07	6.09	37.73
5)	N	MNPM	HMBP	4.15	7.47	4.39	40.21
6)	MN	N	HMBP	11.42	3.28	10.21	32.63
7)	N	MNPM	MNPM	4.15	8.55	4.83	40.21
8)	DB	MNPM	HMBP	5.43	9.30	3.89	40.33
9)	DW	MNPM	HMBP	6.15	9.08	3.28	41.14
10)	DB	MNPM	MNPM	10.64	10.64	4.33	40.33

Although the ROMs generate a good approximation of the aerodynamic coefficients CL, CD, and the efficiency E, the error on the pitching moment coefficient, CM, appears to increase compared to the analysis at $M_\infty = 6$. In particular, as illustrated in Fig.5.8, the maximum error occurs at low angles of attack (where the coefficient tends to be close to 0), then decreases. Fig. 5.8 shows, as an example, the Tangent Cone Empirical model for exposed elements, the MNPM approach for shadowed regions, and HBMP for the base flow, yielding average errors of:
$\text{err}_{C_L} = 6.21\%$, $\text{err}_{C_D} = 4.01\%$, $\text{err}_{E} = 5.08\%$, and $\text{err}_{C_M} = 37.73\%$.
Finally, a slight deviation between the approximated and high-fidelity solutions becomes apparent as the incidence increases.

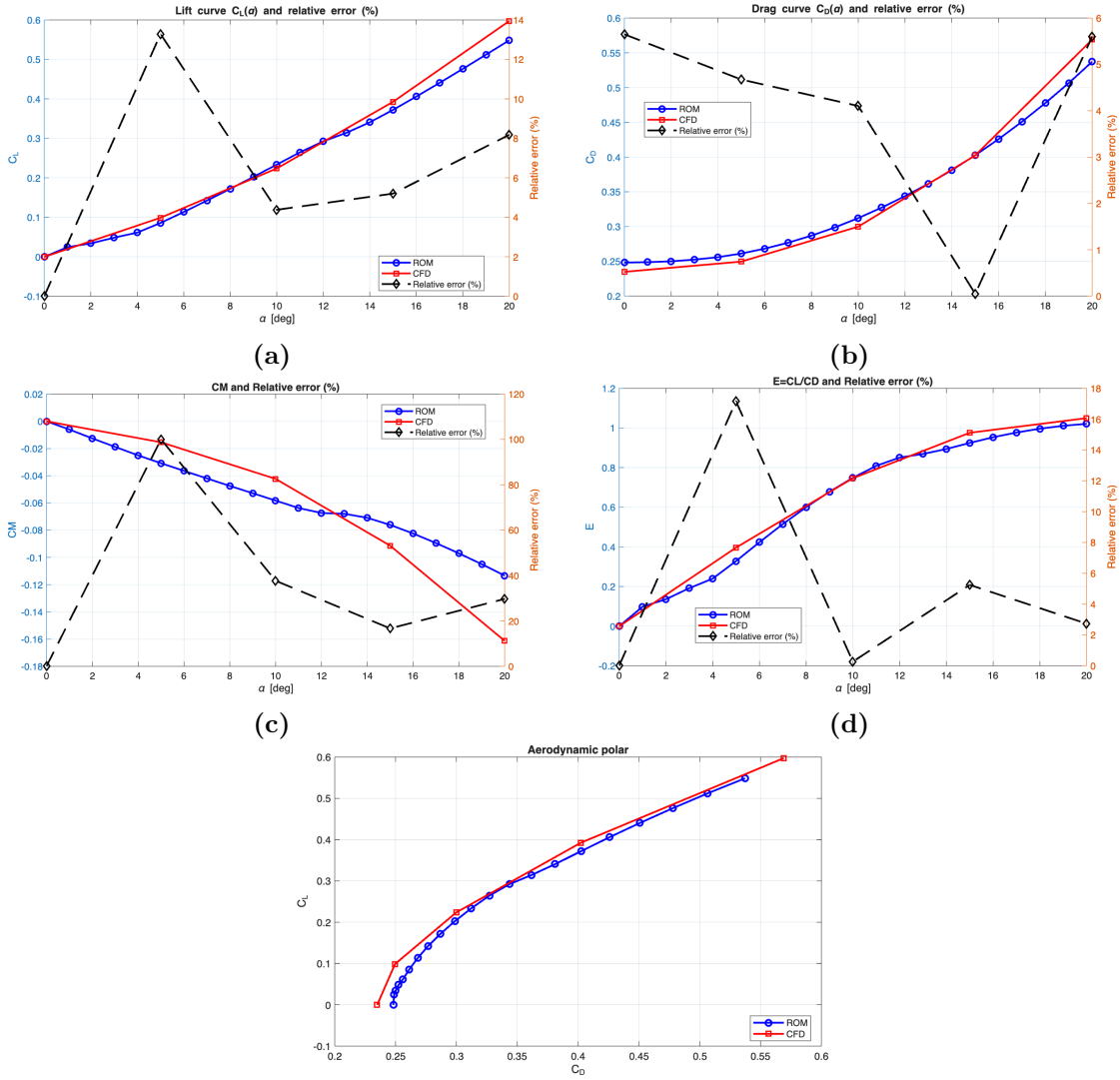

Figure 5.8: HB-2 Mean Relative Percentage Error : $M_\infty = 10$, 30 km. (a) CL. (b) CD. (c) CM. (d) $E = \frac{CL}{CD}$.

HGV

A second ranking, for the CFD analysis at $M = 10$ on the HGV configuration, is shown in Table 5.4.
Following a second parametric analysis comparing different wing-fuselage separation ratios, the 20% separation for the analyzed configuration yields the best result.
As for the simulation performed at $M_\infty = 6$, the Delta Wing and Tangent Wedge models for the wing element and the Modified Newtonian + Prandtl-Meyer model for the fuselage one are the best choices. For the shadow region, the Newtonian (Cp=0) and Prandtl-Meyer from free-stream methods are preferred for the wing element, while MNPM is suitable for the body. This choice may be related to the different intensity of the shock on the two components; in particular, for the fuselage component, with its blunt leading edge, the shock wave is more intense, suggesting the use of a Newtonian approach that captures its characteristics.
As for the HB-2 configuration analyzed at $M_\infty = 10$, the choice of basic method slightly affects force coefficients.
The results obtained from this combination of models show, as in the case at $M_\infty = 6$, an excellent fit with the corresponding CFD analysis results, with a slight divergence at high angles of attack.

Table 5.4: HGV: Best Methods for $M_\infty = 10$.

Rank	E-Wing	E-Body	S-Wing	S-Body	Base	$\bar{e}_{CL}\%$	$\bar{e}_{CD}\%$	$\bar{e}_{E}\%$	$\bar{e}_{CM}\%$
1)	TWE	MNPM	N	MNPM	HMBP	2.74	2.45	5.38	3.73
2)	TWE	MNPM	N	MNPM	MNPM	2.77	2.37	6.64	3.68
3)	DW	MNPM	PMFS	MNPM	MNPM	3.08	6.00	5.75	5.50
4)	TWE	MNPM	N	N	HMBP	6.83	2.69	8.24	3.18
5)	DB	MNPM	PMFS	N	MNPM	3.50	6.44	4.76	6.72
6)	TWE	MNPM	PMFS	MNPM	MNPM	5.34	3.86	6.00	6.30
7)	TWE	MNPM	PMFS	MNPM	HMBP	5.41	2.88	7.07	6.23
8)	DW	MNPM	PMFS	MNPM	HMBP	3.04	6.45	6.91	5.49
9)	DB	MNPM	PMFS	MNPM	HMBP	3.46	6.89	5.78	6.71
10)	TWE	MNPM	N	PMFS	HMBP	8.53	2.98	9.15	3.15

A representative case analysis is reported in Fig.5.9 where 9 different angles of attack ($\alpha = -20°, -15°, -10°, -5°, 0°, 5°, 10°, 15°, 20°$) were tested using Tangent Wedge and Newtonian for the wing, MNPM for the body and the Hight Mach Base Pressure for the base, yielding average errors of:
$\text{err}_{C_L} = 2.74\%$, $\text{err}_{C_D} = 2.45\%$, $\text{err}_{E} = 5.38\%$, and $\text{err}_{C_M} = 3.73\%$.

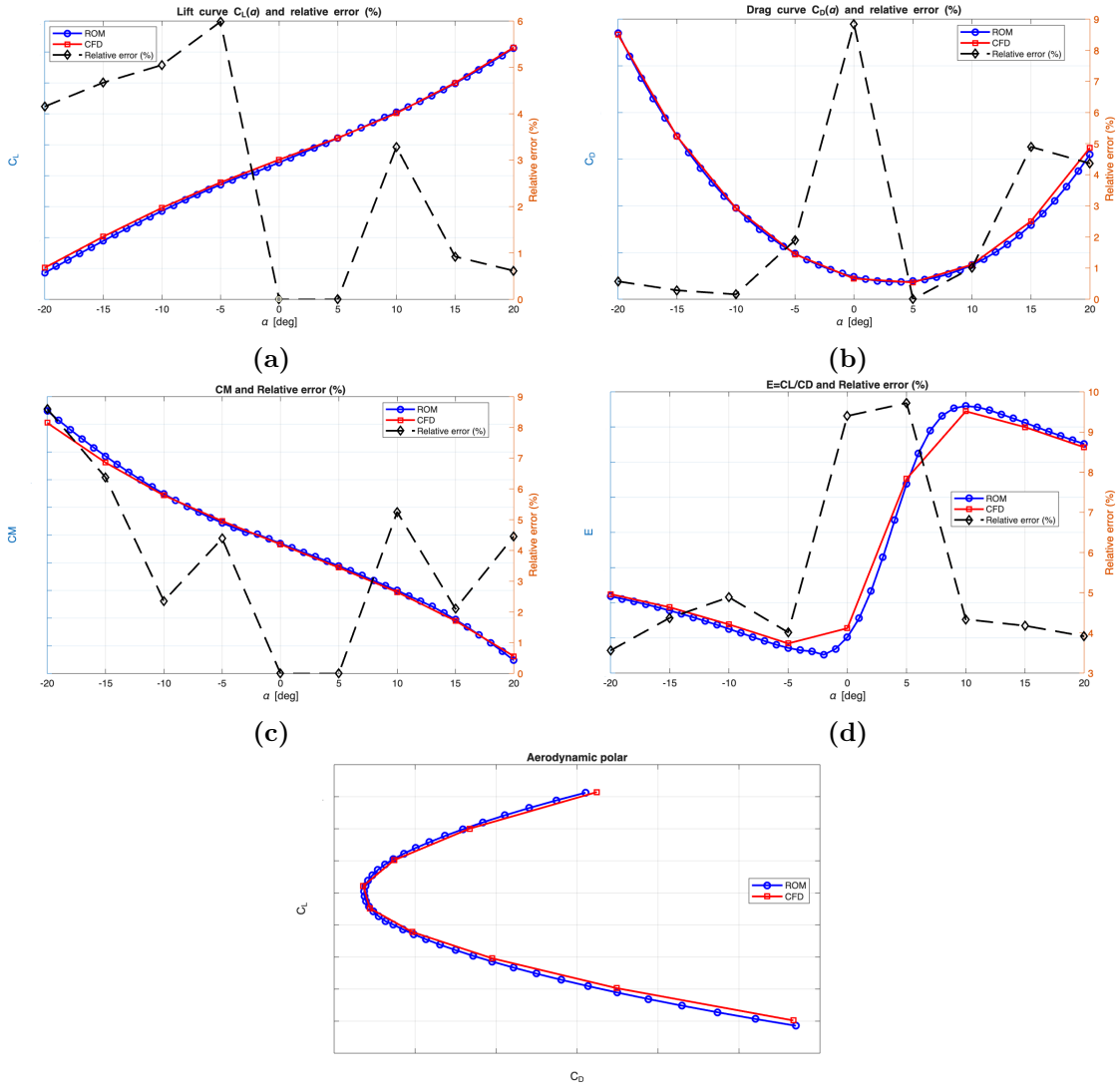

Figure 5.9: HGV Mean Relative Percentage Error : $M_\infty = 10$, 30 km. (a) CL. (b) CD. (c) CM. (d) $E = \frac{CL}{CD}$. (e) Polar CL-CD

5.4.4 M_∞=14

HB-2

A third ranking, for the CFD analysis at $M = 14$ on the HB-2 configuration, is shown in Table 5.5.
Once again, the Newtonian, Empirical Tangent Cone, and Dhalem-Beck models reproduce the pressure coefficient trend well for the exposed region. In this case, at sufficiently high Mach numbers, the Delta Wing method also generates a good approximation, although this is due to its nature, which combines the Tangent Wedge and Tangent Cone methods. For the shadow region, as discussed previously, the MNPM method appears to be the best choice.
In contrast to earlier analyses, the HMBP base method now results in better accuracy. This suggests that HMBP is preferable for high-Mach-number cases compared to the other methods considered.
Although the ROMs provide a good approximation of the aerodynamic coefficients CL, CD, and the efficiency E, the mean relative error in the pitching moment coefficient increases again for this configuration, starting at 45% across all model combinations.

Table 5.5: HB-2: Best Methods for $M_\infty = 14$.

Rank	E-Body	S-Body	Base	$\bar{e}_{CL}\%$	$\bar{e}_{CD}\%$	$\bar{e}_{E}\%$	$\bar{e}_{CM}\%$
1)	DW	MNPM	HMBP	4.99	6.65	4.68	49.13
2)	TCE	MNPM	HMBP	7.36	3.81	5.64	48.64
3)	MN	MNPM	HMBP	8.95	3.62	6.00	47.35
4)	MN	MNPM	MNPM	9.00	3.44	6.24	47.35
5)	TCE	MNPM	MNPM	7.42	4.14	5.88	48.64
6)	DW	MNPM	MNPM	5.04	7.19	4.91	49.13
7)	N	MNPM	HMBP	5.09	6.57	5.02	51.07
8)	N	MNPM	MNPM	5.15	7.11	5.24	51.07
9)	DB	MNPM	HMBP	5.21	8.37	4.46	51.22
10)	DB	MNPM	MNPM	5.13	8.91	4.68	51.22

Fig. 5.10 shows, as an example, the Delta Wing Empirical model for exposed elements, the MNPM approach for shadowed regions, and HBMP for the base flow, yielding average errors of:
$\text{err}_{C_L} = 4.99\%$, $\text{err}_{C_D} = 6.65\%$, $\text{err}_{E} = 4.68\%$, and $\text{err}_{C_M} = 49.13\%$.
Finally, a slight deviation between the approximated and high-fidelity solutions becomes apparent as the incidence increases.

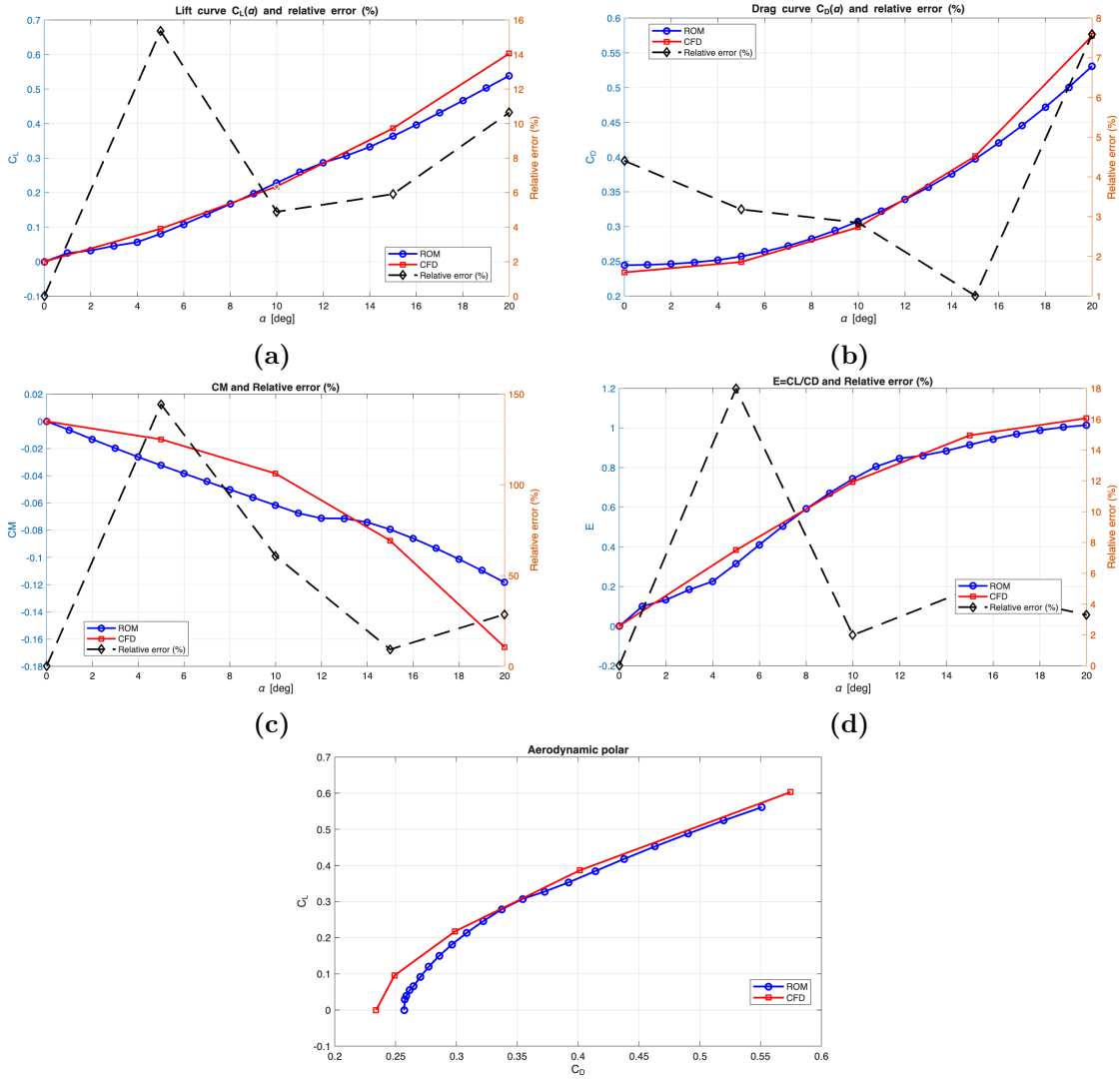

Figure 5.10: HB-2 Mean Relative Percentage Error : $M_\infty = 14$, 30 km. (a) CL. (b) CD. (c) CM. (d) $E = \frac{CL}{CD}$. (e) Polar CL-CD

HGV

A final ranking for the CFD analysis at $M = 14$ on the HGV configuration is presented in Table 5.5.
As in the previous cases, a 20% body–wing separation ratio is adopted to obtain the best results for this configuration. This separation allows an effective distinction between the geometrically blunt and sharp regions of the vehicle.
Compared with the lower Mach-number cases, the best approximations are obtained using the Van Dyke and Tangent Wedge Empirical methods for the exposed wing region, suggesting a deterioration in the accuracy of the Delta Wing method as the Mach number increases. As in the previous configurations, the PMFS and Newtonian shadow methods for the wing provide very similar results.
Regarding the fuselage, the best configuration at high Mach numbers is obtained using the Modified Newtonian plus Prandtl–Meyer model, while the HMBP method provides the most accurate prediction for the base region.

Table 5.6: HGV: Best Methods for $M_\infty = 14$.

Rank	E-Wing	E-Body	S-Wing	S-Body	Base	$\bar{e}_{CL}\%$	$\bar{e}_{CD}\%$	$\bar{e}_{E}\%$	$\bar{e}_{CM}\%$
1)	TWE	MNPM	N	MNPM	HMBP	1.93	3.50	5.82	5.43
2)	TWE	MNPM	PMFS	MNPM	MNPM	2.39	2.70	6.25	5.45
3)	TWE	MNPM	PMFS	MNPM	HMBP	2.39	2.89	6.81	5.42
4)	TWE	MNPM	N	MNPM	MNPM	1.93	4.15	6.48	5.40
5)	VD	MNPM	N	MNPM	HMBP	3.96	2.44	5.63	8.22
6)	VD	MNPM	N	MNPM	MNPM	3.98	2.44	6.26	8.21
7)	TWE	MNPM	N	N	HMBP	5.64	1.89	9.36	4.70
8)	TWE	MNPM	N	PMFS	HMBP	6.58	1.88	9.88	4.62
9)	TWE	MNPM	N	PMFS	PMFS	6.62	2.06	10.57	4.61
10)	VD	MNPM	PMFS	MNPM	MNPM	5.41	2.77	6.05	9.92

The results obtained from this combination of models show, as in the case at $M_\infty = 6$ and $M_\infty = 10$, an excellent fit with the corresponding CFD analysis results, with a slight divergence at high angles of attack. A representative case analysis is reported in Fig.5.11 where 9 different angles of attack ($\alpha = -20°, -15°, -10°, -5°, 0°, 5°, 10°, 15°, 20°$) were tested using Tangent Wedge and Newtonian for the wing, MNPM for the body and the Hight Mach Base Pressure for the base, yielding average errors of:
$\text{err}_{C_L} = 1.93\%$, $\text{err}_{C_D} = 3.50\%$, $\text{err}_{E} = 5.82\%$, and $\text{err}_{C_M} = 5.43\%$.

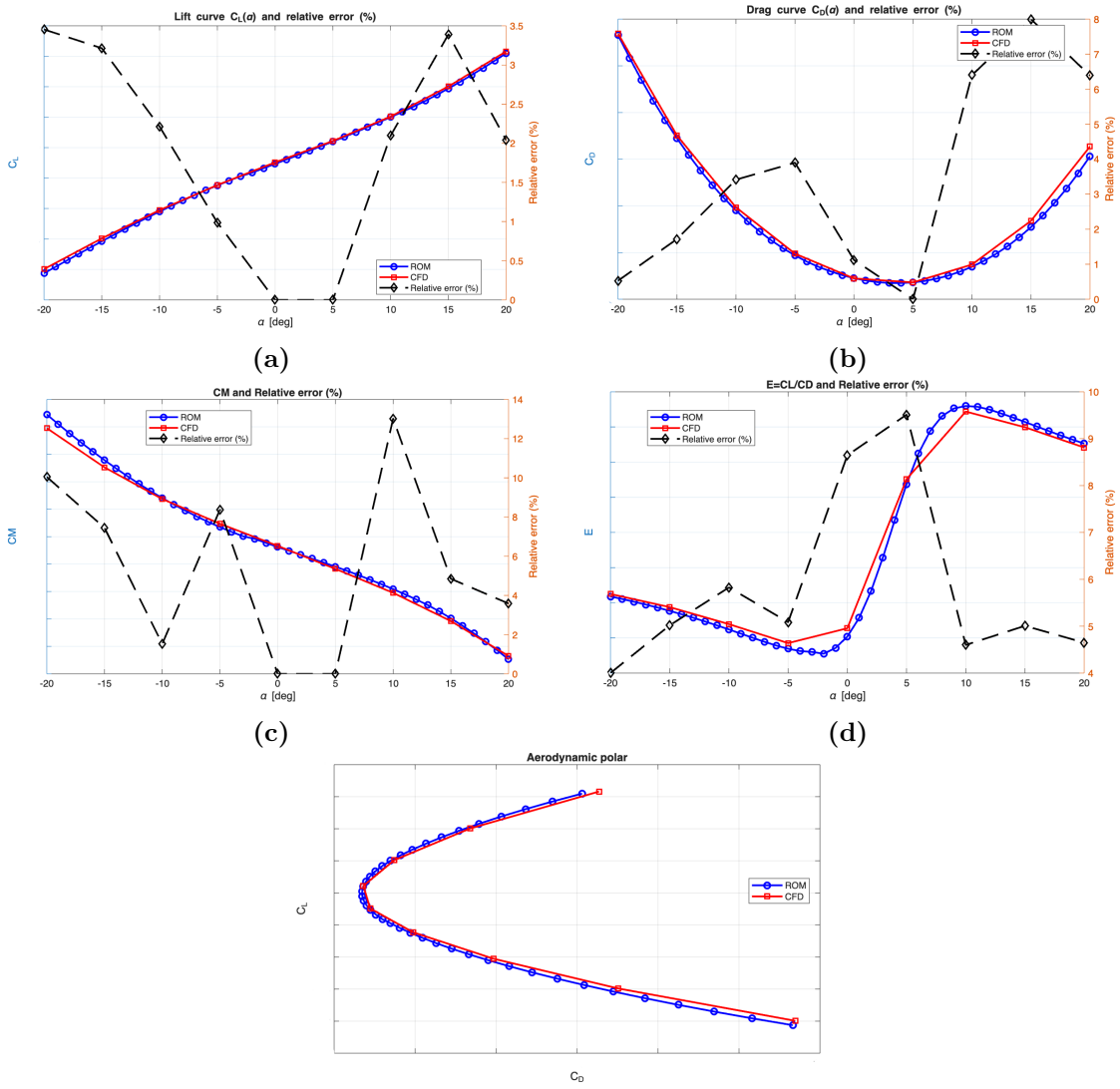

Figure 5.11: HGV Mean Relative Percentage Error : $M_\infty = 14$, 30 km. (a) CL. (b) CD. (c) CM. (d) $E = \frac{CL}{CD}$. (e) Polar CL-CD

5.5 CFD Analysis (With High-Temperature Effects)

A second CFD analysis was performed to account for the high–temperature effects typical of high–Mach-number flows, where the flow was modeled as a reacting air mixture using a five–species model composed of N_2, O_2, NO, N, and O in order to describe the main dissociation processes occurring in the post–shock region.
The simulations were carried out for both the HB-2 and HGV configurations at an altitude of 30 km for several Mach numbers and angles of attack, with the aim of evaluating the influence of real–gas effects on the aerodynamic coefficients and verifying the accuracy of the reduced–order aerodynamic models under more realistic hypersonic conditions.

5.5.1 Modeling & Numerical Choices

For this analysis, the following boundary conditions were adopted:

- **Domain Freestream** ⇒ Farfield, M_∞, ρ_∞, T_∞, Species Mass Fractions
- **Domain Bottom** ⇒ Supersonic outflow
- **Body** ⇒ Viscous wall, turbulent

The governing equations correspond to the three–dimensional compressible Reynolds averaged Navier-Stokes (RANS) equations, coupled with species transport equations for a reacting air mixture. A thermochemical nonequilibrium formulation was adopted using a five–species air model (N_2, O_2, NO, N, O) with a single–temperature description of the thermal modes, while chemical reactions were described using a reaction mechanism file provided by MBDA.
Turbulence was modeled using the one–equation Spalart–Allmaras model (SA-neg version). The governing equations were discretized using an upwind finite–volume scheme with AUSMDV flux splitting and second–order accuracy, while gradients were reconstructed with a least–squares approach. The simulations were performed under steady-state conditions using an implicit Backward–Euler scheme with a LU–SGS linear solver and a CFL number equal to one.
After residual convergence was achieved, the aerodynamic coefficients C_L, C_D, and C_M were extracted from the surface solution and compared with the predictions obtained from the reduced–order models.

5.5.2 M_∞=10

HB-2

A ranking of the best method combinations for the non-equilibrium CFD analysis with high-temperature effects at $M = 10$ on the HB-2 configuration is shown in Table 5.7.
Comparing this simulation with the corresponding case without high-temperature effects in Table 5.3, the best-fitting method combinations remain almost unchanged. In particular, the best choices are obtained with Newtonian and Tangent Cone models for the exposed region, and Modified Newtonian plus Prandtl–Meyer for the shadow one.
Unlike the previous simulation, with the same grid and boundary conditions, the error generally tends to increase when high-temperature effects are included, and the most affected coefficient is the pitching moment coefficient C_M.
This suggests that the pressure distribution and, more generally, the aerodynamic coefficients are influenced by real-gas effects, which will be analyzed in greater detail in Section 5.6.

Table 5.7: HB2: Best Methods for $M_\infty = 10$.

Rank	E-Body	S-Body	Base	$\bar{e}_{CL}\%$	$\bar{e}_{CD}\%$	$\bar{e}_{E}\%$	$\bar{e}_{CM}\%$
1)	MN	MNPM	HMBP	8.21	8.77	5.20	92.90
2)	MN	MNPM	MNPM	8.14	9.49	5.14	92.90
3)	TCE	MNPM	HMBP	8.73	9.66	5.04	94.73
4)	TCE	MNPM	MNPM	8.54	10.38	4.98	94.73
5)	N	MNPM	MNPM	12.80	11.98	5.25	100.95
6)	N	MNPM	HMBP	12.99	11.26	6.09	100.95
7)	DB	MNPM	MNPM	16.67	13.33	7.43	101.54
8)	DB	MNPM	HMBP	16.86	12.61	8.28	101.54
9)	DW	MNPM	MNPM	17.56	13.25	8.26	104.09
10)	DW	MNPM	HMBP	17.74	12.54	9.12	104.09

A representative case analysis is reported in Fig.5.12 where 5 different angles of attack ($\alpha = 0°, 5°, 10°, 15°, 20°$) were tested using Mofied Newtonian for the exposed regione, MNPM for the shadw and the Hight Mach Base Pressure for the base, yielding average errors of:
$\text{err}_{C_L} = 8.21\%$, $\text{err}_{C_D} = 8.77\%$, $\text{err}_{E} = 5.20\%$, and $\text{err}_{C_M} = 92.90\%$.
Again, the ROMs generate a good approximation of the aerodynamic coefficients C_L, C_D, and the efficiency E, while the error peak obtained at $\alpha = 5°$ in Fig. 5.12c for the pitching moment coefficient is partly related to the near-zero value of C_M.

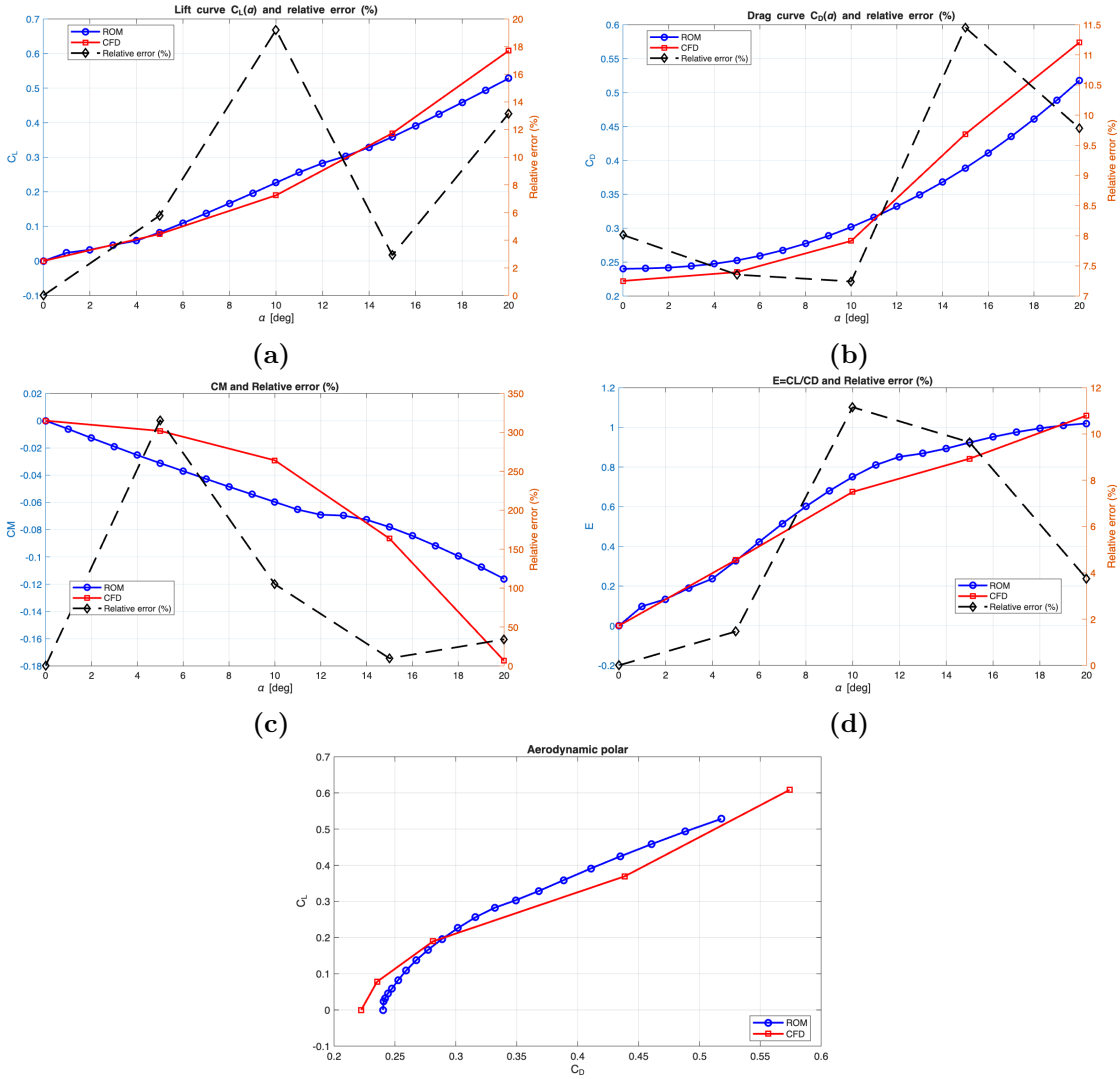

Figure 5.12: HB-2 Mean Relative Percentage Error : $M_\infty = 10$, 30 km. (a) CL. (b) CD. (c) CM. (d) $E = \frac{CL}{CD}$. (e) Polar CL-CD.

HGV

A ranking of the best method combinations for the non-equilibrium CFD analysis with high-temperature effects at $M = 10$ on the HGV configuration is shown in Table 5.8.
As in the previous cases, after a parametric analysis of the wing–fuselage separation parameter along the span, the 20% ratio results in the best choice.
Compared with the simulation performed without high-temperature effects, the Tangent Wedge Empirical and Van Dyke models result as the best choices for the wing in the exposed region, while Newtonian and Tangent Cone models (and their empirical formulations) provide the best results for the fuselage. On the other hand, the MNPM model for the fuselage and PMFS together with the classical Newtonian model for the wing are recommended for the shadow region.
Unlike the HB-2 analysis, despite a slight increase in the mean relative error over the five angles of attack compared with the case without real-gas effects, the reduced-order models are still able to accurately reproduce the trends of the aerodynamic coefficients, in particular the pitching moment coefficient.

Table 5.8: HGV: Best Methods for $M_\infty = 10$.

Rank	E-Wing	E-Body	S-Wing	S-Body	Base	$\bar{e}_{CL}\%$	$\bar{e}_{CD}\%$	$\bar{e}_{E}\%$	$\bar{e}_{CM}\%$
1)	TWE	MNPM	N	MNPM	MNPM	4.67	5.87	5.54	2.85
2)	TWE	MNPM	N	MNPM	HMBP	4.69	8.87	4.85	3.00
3)	TWE	MNPM	N	N	N	8.19	2.55	9.11	1.76
4)	TWE	TWE	PMFS	MNPM	MNPM	5.03	5.02	7.95	3.65
5)	TWE	MNPM	PMFS	MNPM	HMBP	6.41	8.41	5.52	3.11
6)	TWE	TC	PMFS	PMFS	PMFS	2.98	8.45	10.03	2.34
7)	TWE	MNPM	N	PMFS	PMFS	9.16	5.26	8.51	2.01
8)	TWE	TC	PMFS	MNPM	MNPM	4.29	9.83	6.80	4.06
9)	VD	MNPM	N	MNPM	MNPM	7.50	7.32	4.97	5.35
10)	TWE	DW	PMFS	PMFS	PMFS	4.65	6.91	11.37	2.22

Fig. 5.13 shows, as an example, the Tangent Wedge and Newtonian approaches for the wing, MNPM for the body and the base, evaluated over five different angles of attack $(0°, 5°, 10°, 15°, 20°)$[1], yielding average errors of:
$\text{err}_{C_L} = 4.67\%$, $\text{err}_{C_D} = 5.87\%$, $\text{err}_{E} = 5.54\%$, and $\text{err}_{C_M} = 2.85\%$.

[1]In the analysis including high-temperature effects for the HGV configuration, only positive angles of attack were tested.

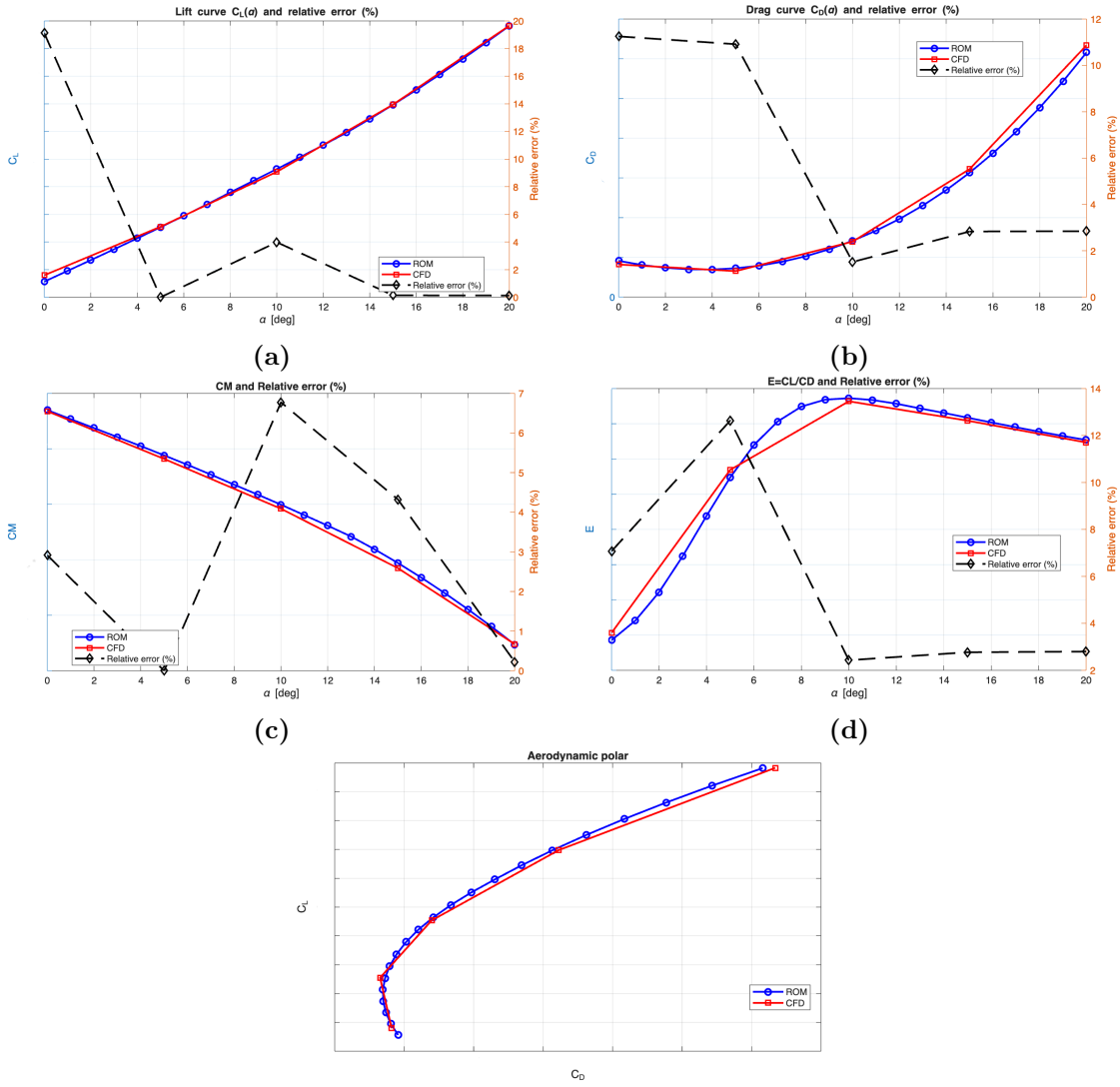

Figure 5.13: HGV Mean Relative Percentage Error : $M_\infty = 10$, 30 km. (a) CL. (b) CD. (c) CM. (d) $E = \frac{CL}{CD}$. (e) Polar CL-CD

5.5.3 M_∞=14

HB-2

A second ranking of the best method combinations for the non-equilibrium CFD analysis with high-temperature effects at $M = 14$ on the HB-2 configuration is shown in Table 5.9.
Again, for the blunted cone–cylinder plus flare configuration, the best model combinations remain the Newtonian and Tangent Cone approaches, together with their empirical formulations, for the exposed region, and MNPM for the base region. In this case it is also possible to observe that, as the Mach number increases, the High Mach Base Pressure method becomes the most suitable choice.
Compared with the analysis without real-gas effects, no significant discrepancies are observed in the aerodynamic efficiency, whereas an increase in the error is observed for the lift, drag, and in particular the pitching moment coefficients.
As in the previews analysis, the accuracy of the methods tends to decrease as the angle of attack increases.

Table 5.9: HB2: Best Methods for $M_\infty = 14$.

Rank	E-Body	S-Body	Base	$\bar{e}_{CL}\%$	$\bar{e}_{CD}\%$	$\bar{e}_{E}\%$	$\bar{e}_{CM}\%$
1)	MN	MNPM	HMBP	9.75	7.68	5.48	153.80
2)	MN	MNPM	MNPM	9.71	8.05	5.73	153.80
3)	TCE	MNPM	HMBP	10.36	8.77	5.08	158.70
4)	TCE	MNPM	MNPM	10.33	9.35	5.33	158.70
5)	DW	MNPM	HMBP	13.21	12.28	5.64	161.27
6)	DW	MNPM	MNPM	13.17	12.86	5.47	161.27
7)	N	MNPM	HMBP	11.96	12.20	4.73	167.01
8)	N	MNPM	MNPM	11.86	12.78	4.61	167.01
9)	MN	N	HMBP	26.58	7.62	20.65	147.27
10)	MN	N	N	26.81	6.77	22.55	147.27

A representative case analysis is reported in Fig.5.14 where 5 different angles of attack ($\alpha = 0°, 5°, 10°, 15°, 20°$) were tested using Mofied Newtonian for the exposed regione, MNPM for the shadw and the Hight Mach Base Pressure for the base, yielding average errors of:
$\text{err}_{C_L} = 9.75\%$, $\text{err}_{C_D} = 7.68\%$, $\text{err}_{E} = 5.48\%$, and $\text{err}_{C_M} = 153.80\%$.

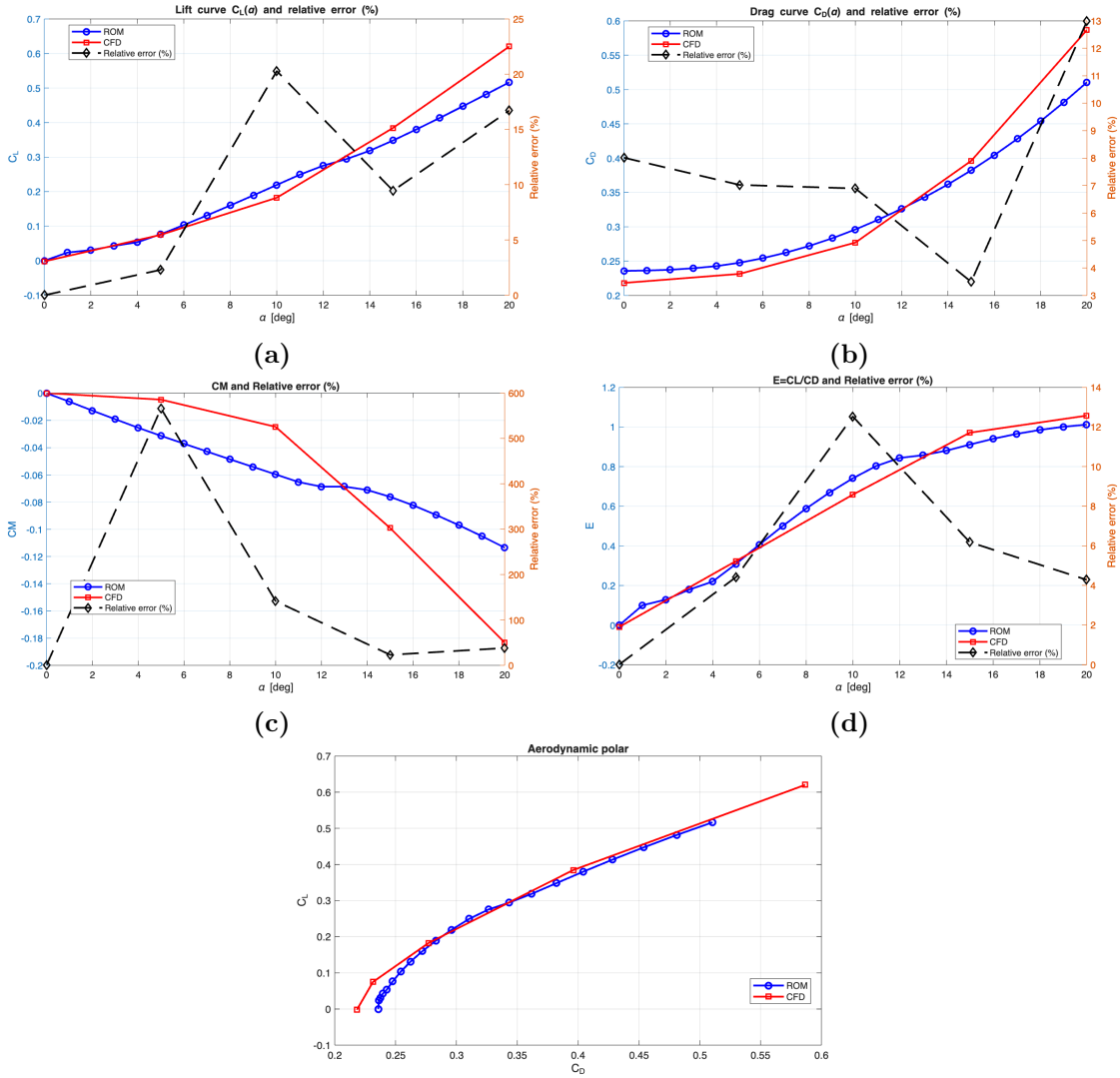

Figure 5.14: HB-2 Mean Relative Percentage Error : $M_\infty = 14$, 30 km. (a) CL. (b) CD. (c) CM. (d) $E = \frac{CL}{CD}$. (e) Polar CL-CD.

HGV

A last ranking of the best method combinations for the non-equilibrium CFD analysis with high-temperature effects at $M = 14$ on the HGV configuration is finally shown in Table 5.10.
Again, the parametric analysis leads to a wing–body separation equal to 20% of the half wingspan; this separation ensures the correct applicability of the methods, which are known to perform differently over different geometries.
In this case, as in the previous ones, Tangent Wedge Empirical and Van Dyke approaches for the exposed region, combined with Prandtl–Meyer from the free stream and the classical Newtonian ($C_p = 0$) formulation for the shadow region, result in the best combination for a sharp geometry such as the wing. On the other hand, MNPM, which estimates the subsonic region behind the bow shock, results in the most suitable method for a blunt body configuration such as the fuselage.
Although the mean relative errors appear to increase compared with the analysis carried out at $M = 10$ and with the analysis without real-gas effects, the models are still able to approximate the different aerodynamic coefficients well, in particular C_M.

Table 5.10: HGV: Best Methods for $M_\infty = 14$.

Rank	E-Wing	E-Body	S-Wing	S-Body	Base	$\bar{e}_{CL}\%$	$\bar{e}_{CD}\%$	$\bar{e}_{E}\%$	$\bar{e}_{CM}\%$
1)	TWE	MNPM	N	MNPM	MNPM	7.52	10.38	6.65	2.94
2)	TWE	MNPM	N	MNPM	HMBP	7.48	12.14	6.11	3.00
3)	TWE	TWE	PMFS	MNPM	MNPM	5.61	8.18	11.83	5.60
4)	TWE	MNPM	PMFS	MNPM	HMBP	8.64	12.08	6.70	4.09
5)	VD	TWE	PMFS	MNPM	MNPM	6.37	6.65	11.73	7.80
6)	TWE	MNPM	N	N	N	12.03	8.47	10.20	1.90
7)	DB	MNPM	PMFS	MNPM	HMBP	7.61	13.79	5.42	5.94
8)	DB	MNPM	N	MNPM	MNPM	8.25	12.37	5.14	7.75
9)	TWE	MNPM	PMFS	MNPM	MNPM	8.60	13.86	7.05	4.17
10)	TWE	TC	PMFS	PMFS	PMFS	3.45	11.24	15.51	3.93

Fig. 5.15 shows, as an example, the Tangent Wedge and Newtonian approaches for the wing, MNPM for the body and the base, evaluated over five different angles of attack $(0°, 5°, 10°, 15°, 20°)$[2], yielding average errors of:
$\text{err}_{C_L} = 7.52\%$, $\text{err}_{C_D} = 10.38\%$, $\text{err}_{E} = 6.65\%$, and $\text{err}_{C_M} = 2.94\%$.

[2]In the analysis including high-temperature effects for the HGV configuration, only positive angles of attack were tested.

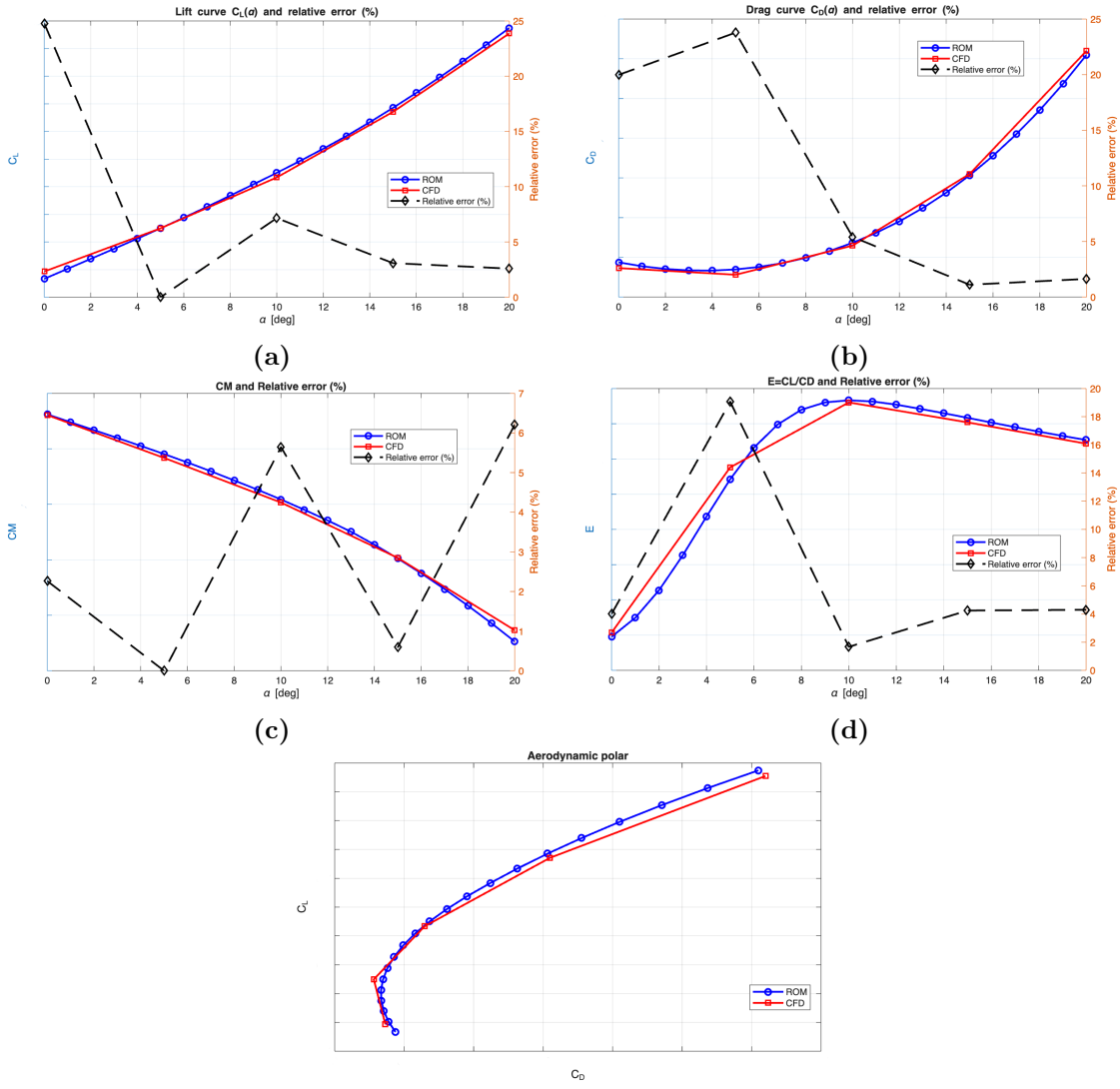

Figure 5.15: HGV Mean Relative Percentage Error : $M_\infty = 14$, 30 km. (a) CL. (b) CD. (c) CM. (d) $E = \frac{CL}{CD}$. (e) Polar CL-CD

5.5.4 M_∞=20

HGV

A final analysis was performed for the HGV configuration by increasing the Mach number to $M_\infty = 20$, considering five angles of attack (0°, 5°, 10°, 15°, 20°).
Once again, a wing–body separation ratio equal to 20% of the half wingspan was adopted in order to improve the accuracy of the simulation. A ranking of the best reduced–order model combinations is reported in Table 5.11.
It can be observed that the Modified Newtonian + Prandtl–Meyer method represents the most suitable choice for the fuselage region, both for the exposed and the shadow surfaces. This behaviour can be explained by the fact that this approach is the only one among the considered models that accounts for the coexistence of subsonic and supersonic flow regions downstream of a strong shock wave over blunt-nosed configurations. On the other hand, empirical models belonging to the Tangent Wedge family, such as Tangent Wedge Empirical, Delta Wing and Dahlem–Beck methods, provide the most accurate predictions for the exposed region of the wing.
The pressure coefficient distribution in the shadow region of the wing, consistently with the previous analyses, is better approximated by using either the classical Newtonian theory ($C_p = 0$) or the Prandtl–Meyer from free-stream approach while, in this case, the choice of the base-flow model does not appear to significantly affect the overall results.

Table 5.11: HGV: Best Methods for $M_\infty = 20$.

Rank	E-Wing	E-Body	S-Wing	S-Body	Base	$\bar{e}_{CL}\%$	$\bar{e}_{CD}\%$	$\bar{e}_{E}\%$	$\bar{e}_{CM}\%$
1)	TWE	MNPM	N	MNPM	MNPM	9.88	12.47	7.90	4.37
2)	TWE	MNPM	N	MNPM	HMBP	9.85	13.47	7.57	4.35
3)	TWE	MNPM	PMFS	MNPM	HMBP	10.49	13.61	7.96	4.91
4)	TWE	MNPM	PMFS	MNPM	MNPM	10.47	14.60	7.68	4.88
5)	DW	MNPM	PMFS	MNPM	HMBP	5.82	13.36	7.79	11.02
6)	DB	MNPM	PMFS	MNPM	HMBP	9.82	16.70	6.83	5.26
7)	DW	MNPM	PMFS	MNPM	MNPM	5.83	14.09	7.93	11.03
8)	DB	MNPM	N	MNPM	MNPM	10.14	15.94	6.75	6.27
9)	DW	MNPM	N	MNPM	MNPM	6.30	13.06	7.73	12.09
10)	DB	MNPM	PMFS	MNPM	MNPM	9.83	17.49	6.56	5.33

Although the relative error in the aerodynamic coefficients, obtained from the comparison with the CFD analysis, is on average slightly higher than that observed at lower Mach numbers, the selected methods still show a high level of accuracy.
Fig. 5.16 shows, as an example, the Tangent Wedge Empirical and Newtonian

approaches for the wing, MNPM for the body and the base, evaluated over five different angles of attack $(0°, 5°, 10°, 15°, 20°)$yielding average errors of: $\text{err}_{C_L} = 9.88\%$, $\text{err}_{C_D} = 12.47\%$, $\text{err}_E = 7.90\%$, and $\text{err}_{C_M} = 4.37\%$.

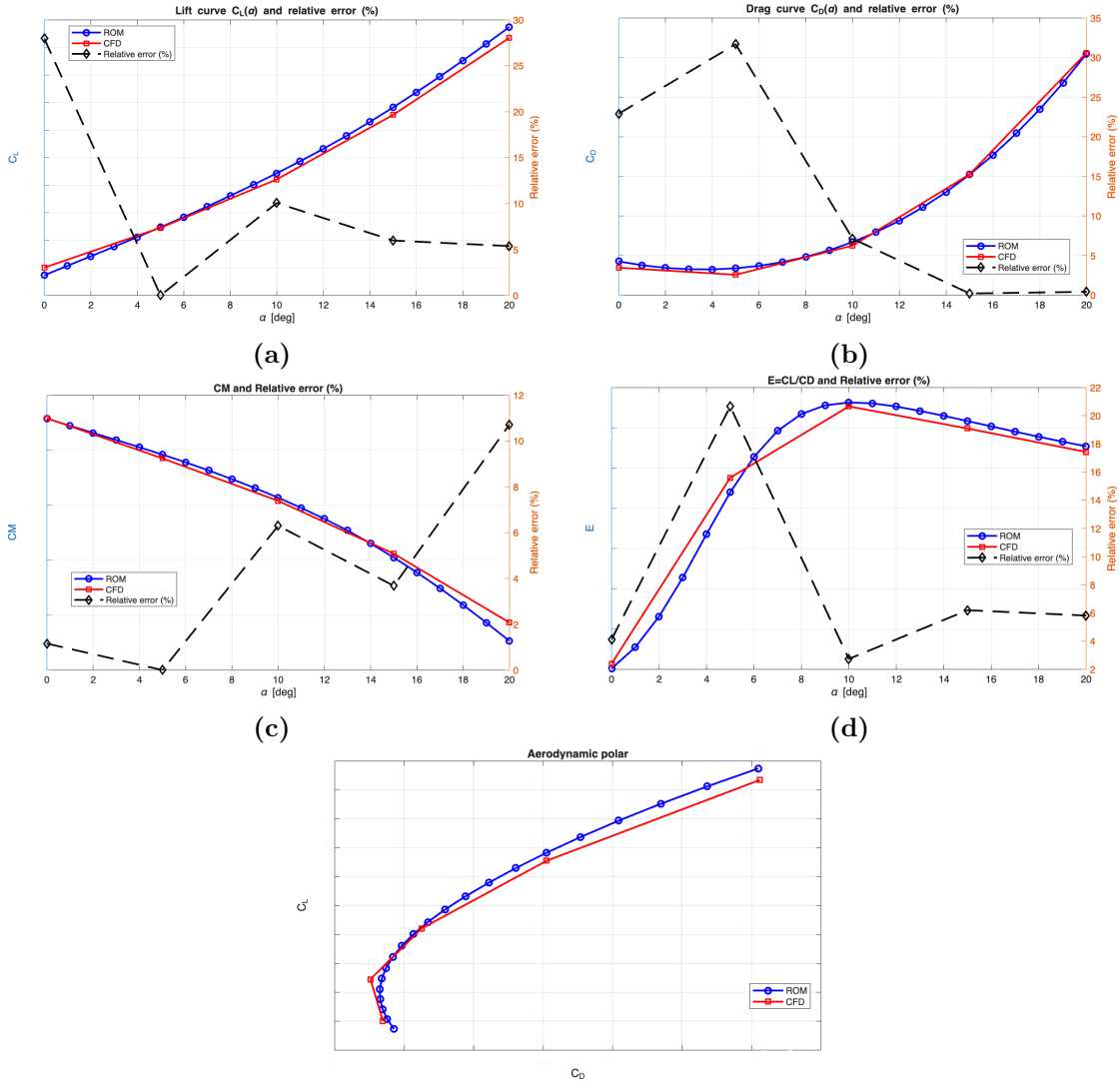

Figure 5.16: HGV Mean Relative Percentage Error : $M_\infty = 20$, 30 km. (a) CL. (b) CD. (c) CM. (d) $E = \frac{CL}{CD}$. (e) Polar CL-CD

5.6 Mach Number and Real-gas effects on the aerodynamic coefficients

As observed in the previous analyses, the accuracy of the reduced-order models tends to decrease when high-temperature effects are considered, compared to the analyses performed on the same geometries under identical flight conditions in terms of altitude and Mach number. In particular, the prediction of the pitching-moment coefficient shows significant discrepancies relative to the high-fidelity CFD solution for a blunt-nose configuration such as the HB-2, especially at large angles of attack and at high Mach numbers.
This section shows in detail the high-temperature effects on CFD and the combined impact of increased Mach number on aerodynamic coefficients.

5.6.1 HGV

In accordance with the Mach independence principle, the main aerodynamic coefficients tend to approach asymptotic trends as the Mach number increases. In particular, it can be observed that the lift and drag coefficients (Figures 5.17 and 5.18) decrease as the Mach number increase, while the pitching-moment coefficient (Figure 5.18) tends to increase. High-temperature effects (HTE), associated with molecular dissociation processes characterized by endothermic reactions and the consequent absorption of thermal energy, further amplify this phenomenon by altering the pressure distribution over the vehicle surface.
Similarly to the aerodynamic coefficients, the aerodynamic efficiency (Figure 5.20), being their ratio, also tends to approach a plateau as the Mach number increases. The decrease of the lift and drag coefficients with increasing Mach number and with the onset of real-gas effects may explain the deterioration of the approximations provided by the reduced-order models observed in the previous section.
In particular, for a fixed Mach number, geometry, and specific heat ratio, the same combination of reduced-order models always produces the same aerodynamic coefficients. As a consequence, such combination of models appear more suitable for viscous analyses under perfect-gas assumptions, where high-temperature effects are neglected.

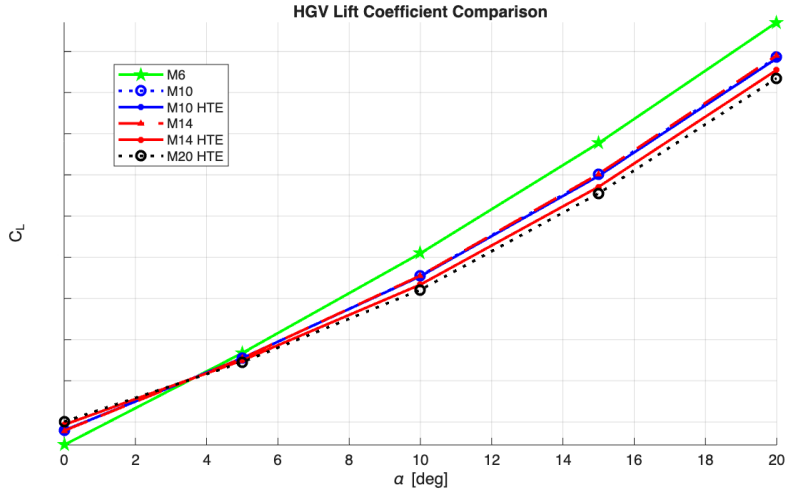

Figure 5.17: HGV: C_L comparison for different Mach numbers with and without real-gas effects at various angles of attack at 30 km altitude.

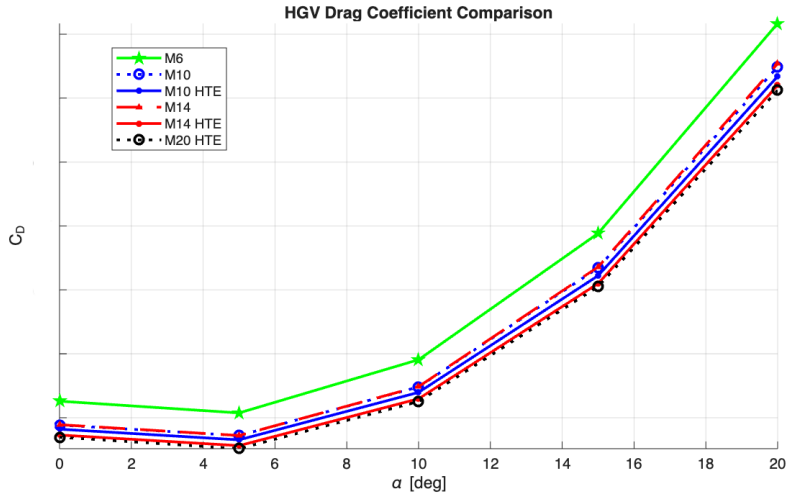

Figure 5.18: HGV: C_D comparison for different Mach numbers with and without real-gas effects at various angles of attack at 30 km altitude.

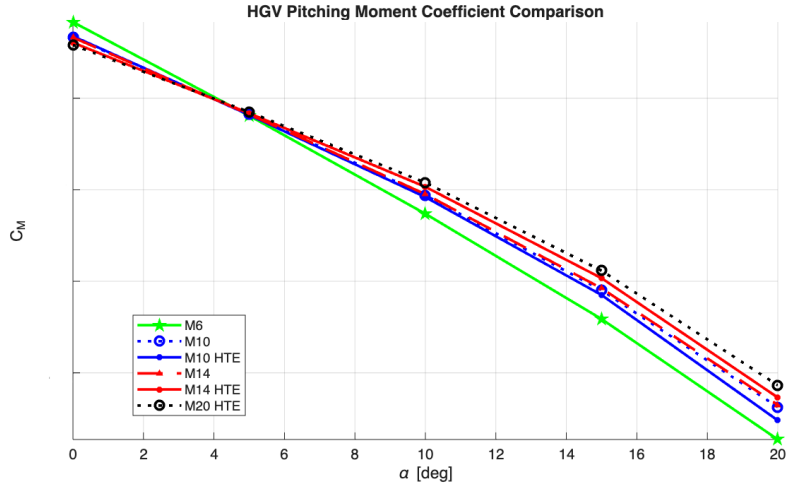

Figure 5.19: HGV: C_M comparison for different Mach numbers with and without real-gas effects at various angles of attack at 30 km altitude.

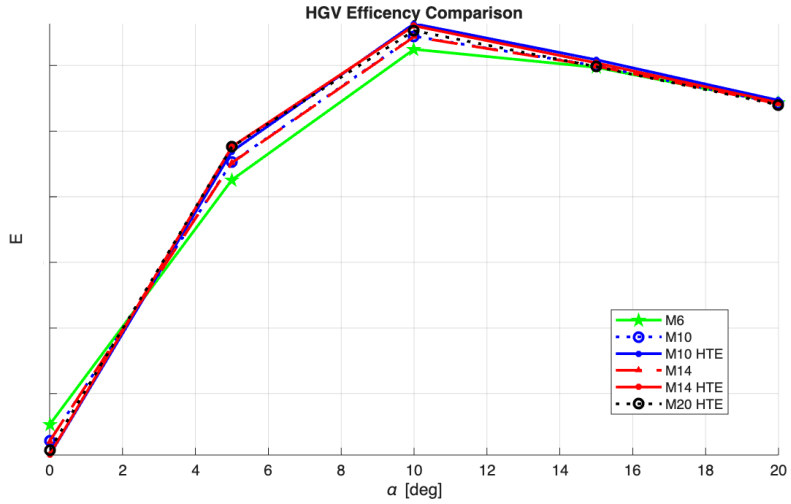

Figure 5.20: HGV: Efficency comparison for different Mach numbers with and without real-gas effects at various angles of attack at 30 km altitude.

5.6.2 HB-2

Similar considerations can be made for the HB-2 geometry, with the exception of the pitching-moment coefficient, which does not appear to increase with increasing Mach number.

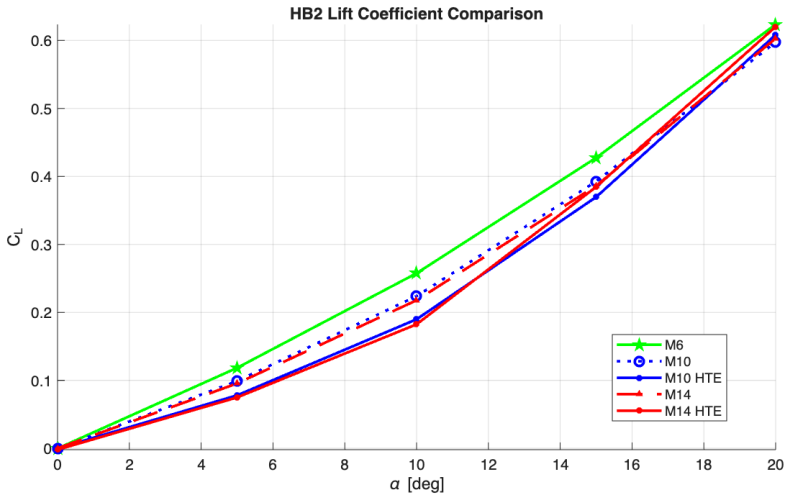

Figure 5.21: HB-2: C_L comparison for different Mach numbers with and without real-gas effects at various angles of attack at 30 km altitude.

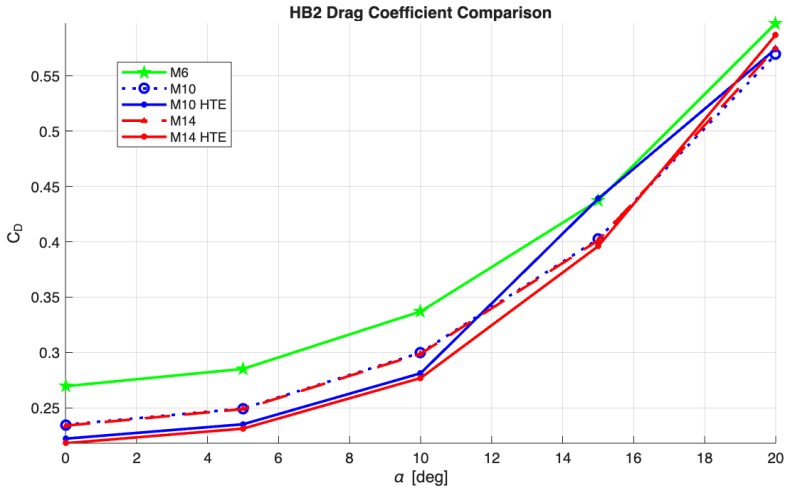

Figure 5.22: HB-2: C_D comparison for different Mach numbers with and without real-gas effects at various angles of attack at 30 km altitude.

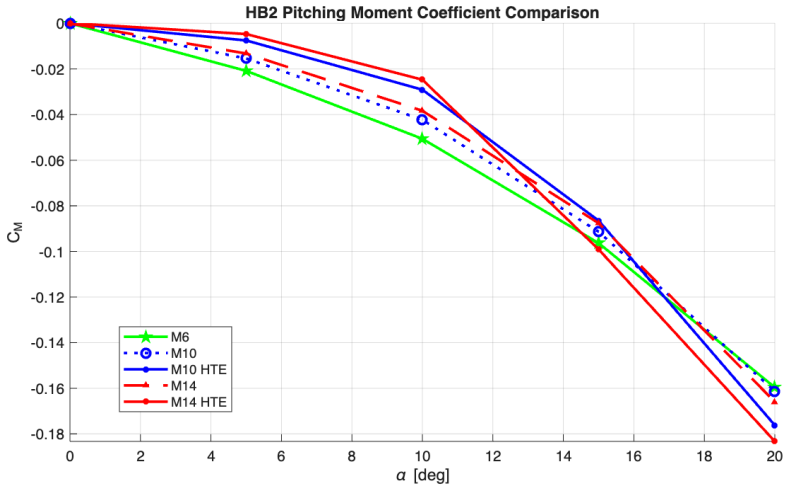

Figure 5.23: HB-2: C_M comparison for different Mach numbers with and without real-gas effects at various angles of attack at 30 km altitude.

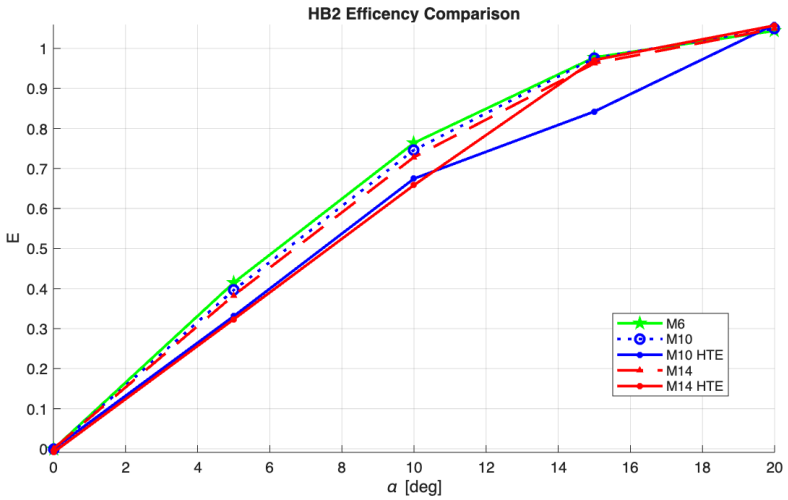

Figure 5.24: HB-2: Efficency comparison for different Mach numbers with and without real-gas effects at various angles of attack at 30 km altitude.

Comparison with experimental data

The CFD analyses for both geometries were compared with literature data to assess their accuracy. In the specific case of the HB-2 geometry, the wind tunnel measurements reported in [12] were used as reference.
The comparison was performed at the same Mach number and with a Reynolds number

$$Re_d = \frac{\rho_\infty V_\infty d}{\mu_\infty} \tag{5.2}$$

based on the centerbody diameter d, similar to the value used in the experiment (10^6).
Since only the normal force coefficient C_N and the pitching moment coefficient C_m are reported in the experimental dataset, the aerodynamic coefficients obtained from the CFD analysis were combined to obtain the normal force coefficient as

$$C_N = C_L \cos\alpha + C_D \sin\alpha \tag{5.3}$$

This leads to the following comparison :

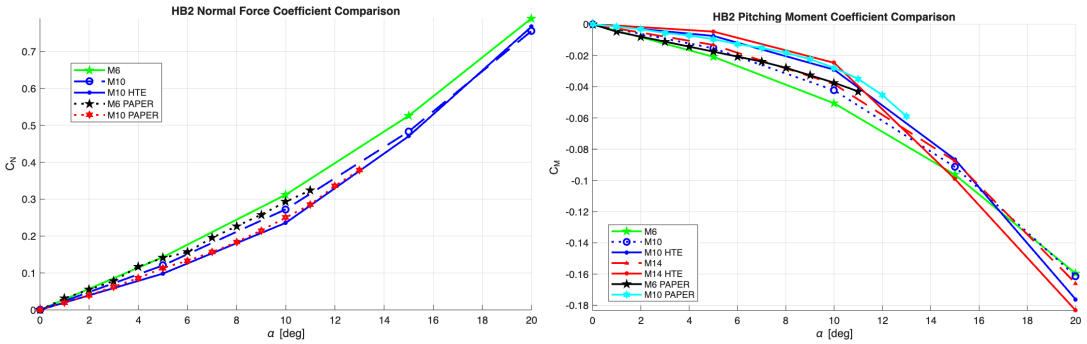

Figure 5.25: HB-2: C_N and C_m comparison for different Mach numbers between CFD and experimental data

The normal force and the pitching-moment coefficient show good agreement with respect to wind tunnel results, confirming the accuracy of the numerical analysis. In particular, simulations performed under the real gas assumption at $M_\infty = 10$ are more accurate than those at $M_\infty = 6$ without high-temperature effects, suggesting the need to include such effects in the hypersonic regime even at lower Machs.

5.7 Residual Analysis and CFD Post-Processing

Although the aerodynamic coefficients obtained from CFD were consistent with literature data, it is worth noting that, due to time constraints, a mesh sensitivity analysis was not performed. Instead, meshes with a limited number of elements were employed as an initial first guess, in order to enable extensive testing of the console across multiple configurations within the available time. However, the meshing and refinement criteria presented above were chosen in accordance with the guidelines proposed by MBDA.
To assess the quality and convergence of the numerical solution, the residuals of the governing equations were first examined. Subsequently, the main output quantities were monitored to identify any non-physical behavior and to ensure the overall consistency of the results.

5.7.1 Residual Analysis

To monitor the residual behavior and the convergence of the aerodynamic coefficients for each tested configuration, Python and MATLAB routines provided by MBDA were employed. It was observed that, although the residuals remained relatively low during the final iterations ($< 10^{-3}$), they tended to reach a plateau and exhibited small oscillations from one iteration to the next around this level (see Fig. 5.26a). This behavior may be attributed to flow unsteadiness, yet the problem is treated under a steady-state assumption.
At the same time, the convergence of the aerodynamic coefficients as a function of the iteration number was also investigated. It was observed that these coefficients tend to approach an asymptotic value after approximately 5000 iterations. Based on this analysis, for each configuration, the aerodynamic coefficients used for comparison with the reduced-order models in Sections 5.4 and 5.5 were extracted as the average of their values over the last 500 iterations.
Figure 5.26 shows, as an example, the residuals of continuity (R_ρ), momentum ($R_{\rho v_x}$, $R_{\rho v_y}$, $R_{\rho v_z}$), energy ($R_{\rho E}$), and turbulent dissipation ($R_{\rho \nu \varepsilon}$), together with the corresponding asymptotic convergence of the aerodynamic coefficients, for the HGV and HB-2 configurations tested at $M_\infty = 14$ and an altitude of 30 km.

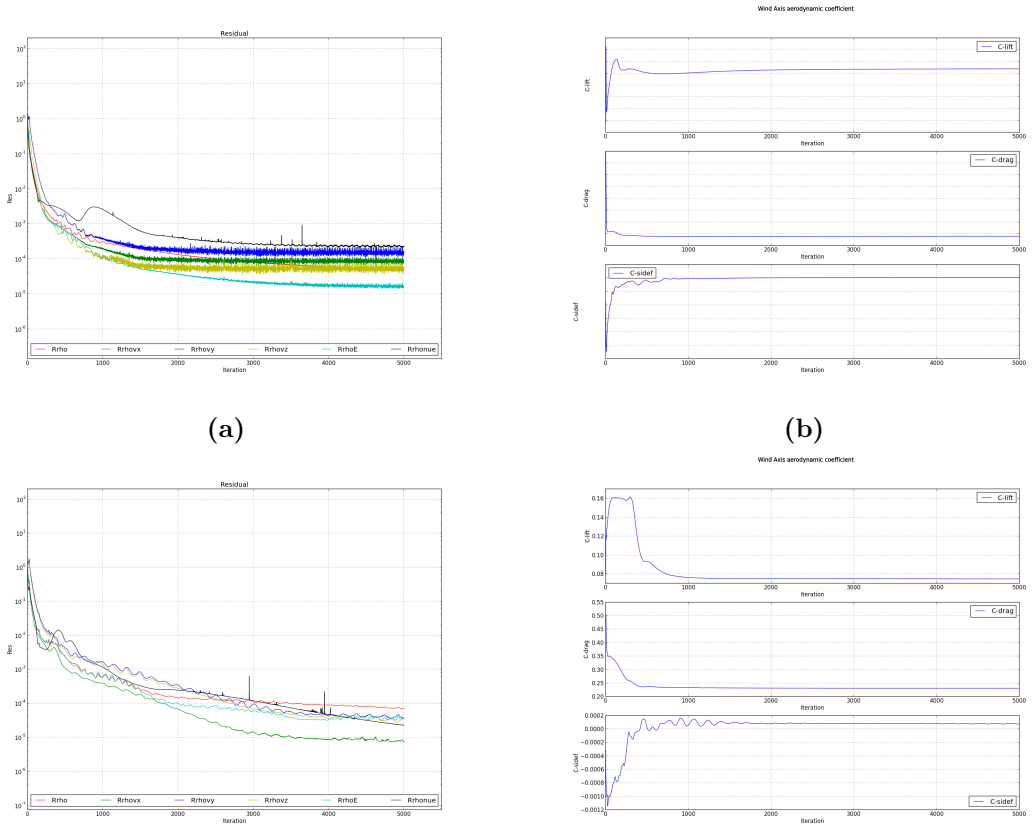

Figure 5.26: Convergence Analysis (a) Residual HGV M14, $\alpha = 10$. (b) Aerodynamic Coefficents HGV M14, $\alpha = 10$. (c) Residual HB2 M14, $\alpha = 5$. (d) Aerodynamic Coefficents HB2 M14, $\alpha = 5$.

5.7.2 CFD Contours

Finally, in order to identify any non-physical behavior and to verify the overall consistency of the results, the main output quantities were monitored within the META software by Beta CAE Systems. In this section, only a selection of contour plots for the HB-2 configuration is presented.

Mach Number and Streamlines

The analysis of the Mach number contours did not reveal significant differences, under the same boundary conditions, between the cases with and without high-temperature effects (HTE), except in the wake region.
On the other hand, the presence of the boundary layer (blue region around the body) can be clearly observed, together with the shock generated by the flare. As the angle of attack increases, this shock tends to compress the streamlines more strongly near the wall in the ventral region and to generate a third shock through its interaction with the nose one.

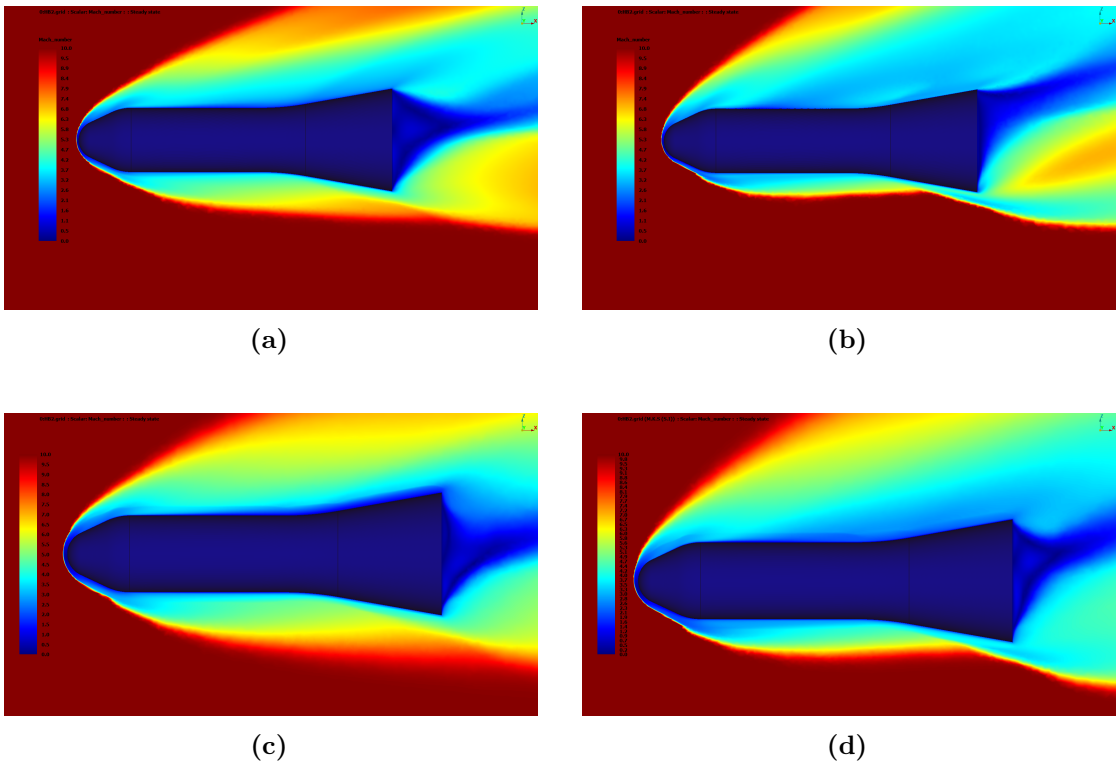

(a) **(b)**

(c) **(d)**

Figure 5.27: Mach Number: (a) HB2: Mach Number $M_\infty = 10$, $\alpha = 10$, HTE. (b) HB2: Mach Number $M_\infty = 10$, $\alpha = 20$, HTE. (c) HB2: Mach Number $M_\infty = 10$, $\alpha = 10$, no HTE. (d) HB2: Mach Number $M_\infty = 10$, $\alpha = 20$, no HTE.

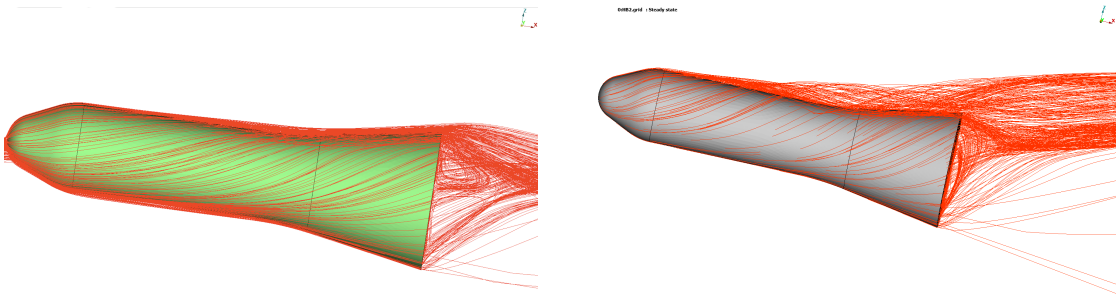

(a) **(b)**

Figure 5.28: Streamlines: (a) HB2: Streamline $M_\infty = 10$, $\alpha = 10$, HTE. (b) HB2: Streamline $M_\infty = 10$, $\alpha = 20$, HTE.

Dissociation and Specific Heat Ratio

The analysis of the specific heat ratio contours reveals a clear decrease of γ across the shock layer, with a minimum located in the stagnation region and a subsequent recovery due to flow expansion and cooling. This non-negligible behavior is directly related to the increase in temperature and the onset of molecular dissociation, highlighting the importance of adopting real-gas models to achieve a more physically accurate description of the flow.
Other relevant quantities, shown in Fig. 5.30, are the species mass fractions and the resulting products of the chemical reactions. In agreement with dissociation temperatures, a significant production of atomic oxygen (O) and nitric oxide (NO) is observed, mainly resulting from the dissociation of molecular oxygen (O_2) and the subsequent recombination reactions involving nitrogen. On the other hand, atomic nitrogen (N) is present only in limited regions downstream of the bow shock.

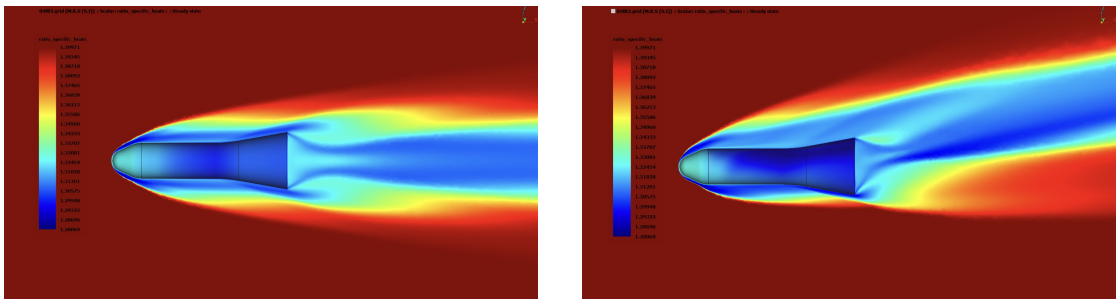

(a) **(b)**

Figure 5.29: Rateo of Specific Heats and (a) HB2: Mach Number $M_\infty = 14$, $\alpha = 0$, HTE. (b) HB2: Mach Number $M_\infty = 14$, $\alpha = 10$, HTE.

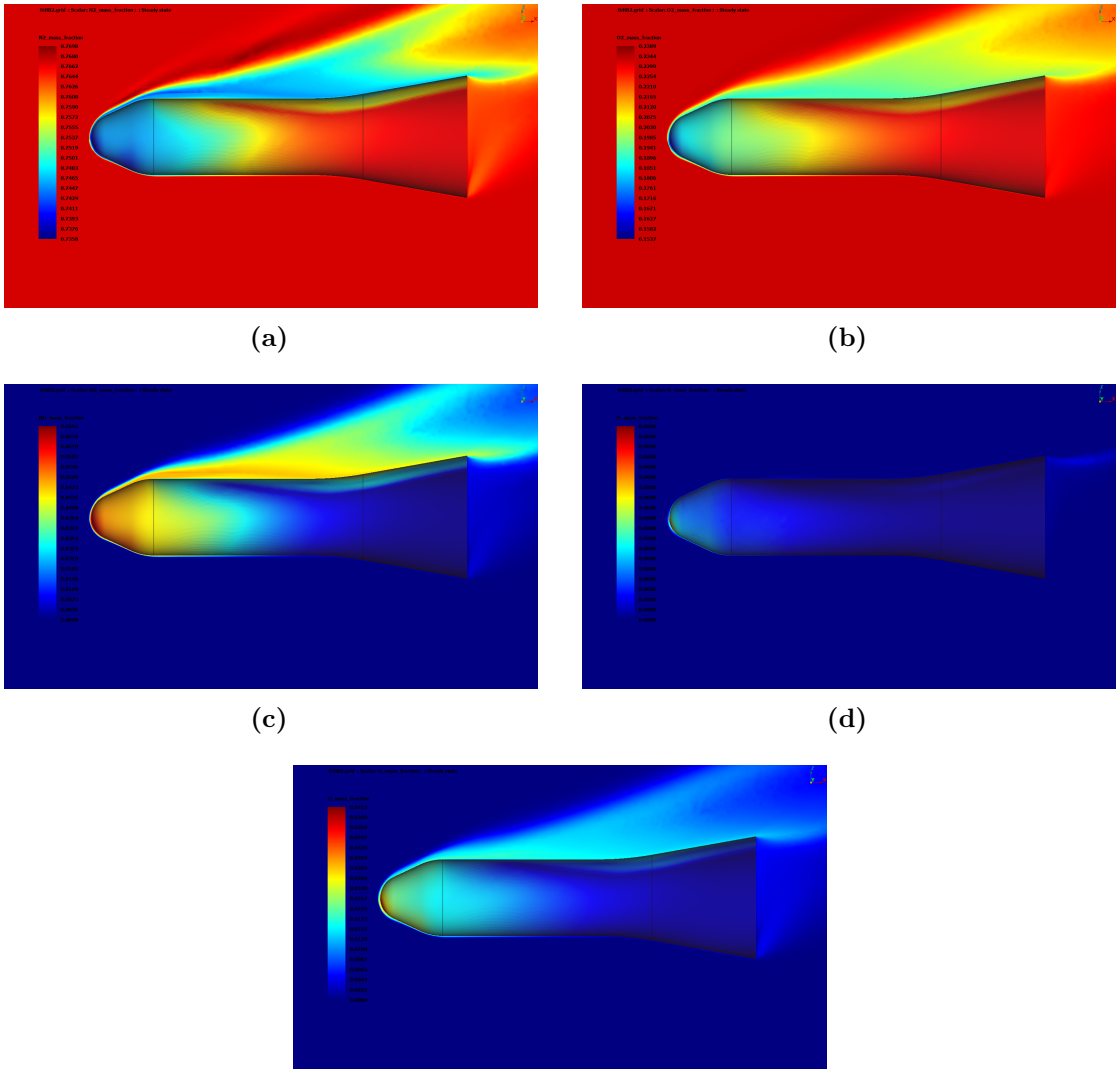

(a) **(b)**

(c) **(d)**

(e)

Figure 5.30: HB2 Mass Fraction for $M_\infty = 10$, $\alpha = 20$, (a) N2 Mass fraction. (b) O2 Mass fraction. (c) NO Mass fraction. (d) N Mass fraction. (e) O Mass fraction.

Pressure Coefficient

A further analysis was carried out to compare the surface pressure-coefficient distributions obtained from the CFD simulations with those predicted by the different reduced-order methods. In particular, the C_p distributions associated with the best-fitting methods for the various configurations were examined visually using the same color scale. No significant discrepancies were observed, further confirming the suitability of these reduced-order approaches for preliminary analysis, as shown, for example, in Fig. 5.31.

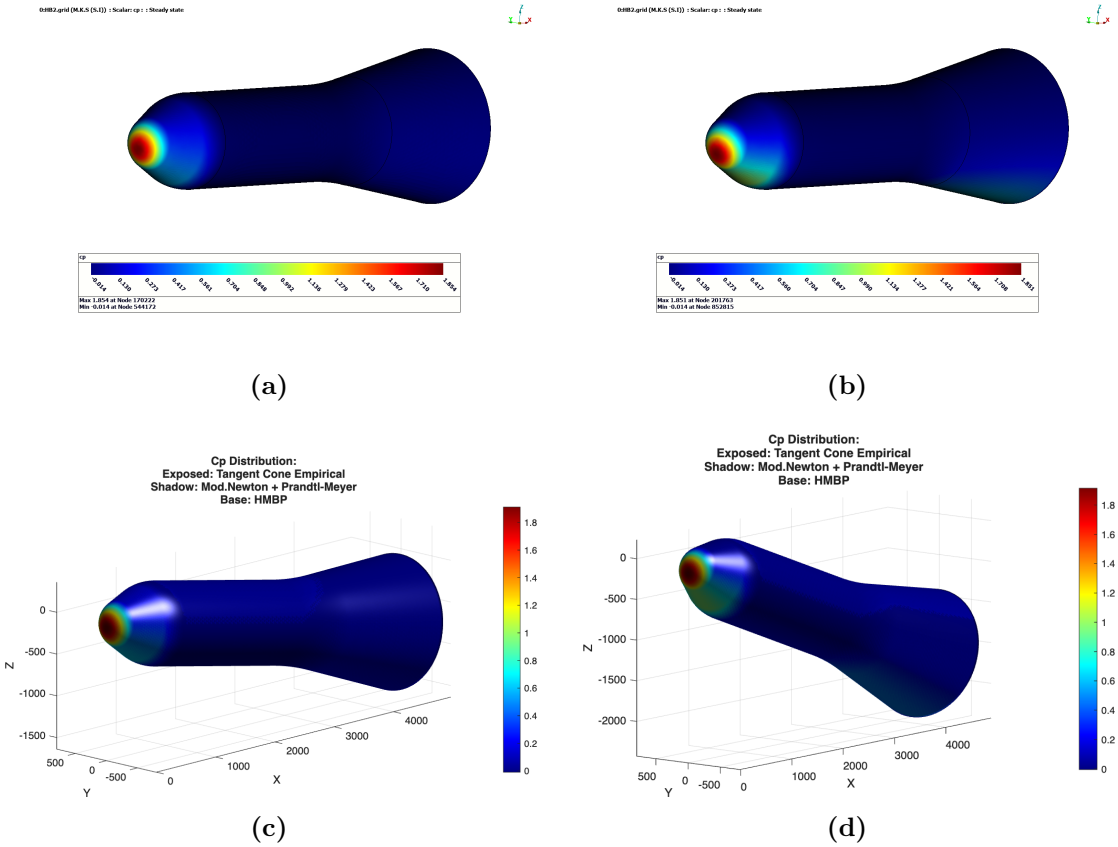

Figure 5.31: Pressure Coefficent C_p, $\alpha = 20$, 30 km: (a) CFD: $M_\infty = 10$, $\alpha = 10$. (b) CFD: $M_\infty = 14$, $\alpha = 20$. (c) ROM: TCE+MNPM+HMBP, $M_\infty = 10$, $\alpha = 10$. (d) ROM: TCE+MNPM+HMBP, $M_\infty = 14$, $\alpha = 20$.

5.8 Computational Cost and Summary

The analyses presented in this chapter have shown that several reduced-order method combinations can provide accurate approximations of the surface pressure coefficient distributions and, in most cases, of all the main aerodynamic coefficients. It has also been observed that accuracy generally decreases when real-gas effects are considered. Nevertheless, the results remain satisfactory, with relative errors generally below 12%, especially for glider-type configurations. A less accurate prediction has instead been observed for the pitching moment coefficient of the HB-2 configuration.

On the other hand, the high-fidelity analyses, although capable of providing highly accurate results and good agreement with available experimental data, proved extremely expensive computationally, especially when high-temperature effects were included. All CFD simulations were performed on 24 cores, using meshes of approximately 10 million elements and 5000 iterations for each angle of attack, to ensure convergence of the output parameters and a sufficient reduction in the residuals. In the most expensive case, viscous simulations including high-temperature effects, each tested angle of attack required approximately 4 hours for the HB-2 configuration and about 7 hours for the HGV configuration. It should be emphasized that the computational cost is strongly dependent on the number of mesh elements and, for more accurate analyses, the mesh size can reach hundreds of millions of cells, leading to extremely long computational times on the same number of processor cores.

As an example, the computational times required by the reduced-order methods can be compared with those of CFD for the HGV configuration at $M_\infty = 10$, including high-temperature effects and considering a total of five angles of attack (see Section 5.5.2). The corresponding results are reported in Table 5.12. Together with those presented in the previous section, they highlight the strong computational efficiency of the reduced-order framework, which requires only seconds rather than hours, making it particularly well-suited for preliminary design studies and large parametric analyses.

The ROM speed was exploited in the Fast Console to select the best combination of reduced-order models based on geometry and Mach number. Specifically, 504 different combinations were tested for the body-wing separation option at 5 or 9 angles of attack in about half an hour, and 78 combinations for full-body options in about 8 minutes. Based on this analysis, Figure 5.32 was constructed to guide the user in selecting the best combination of fitting models within the console .

Table 5.12: HGV: computational time comparison at $M_\infty = 10$.

Configuration	E-Wing	E-Body	S-Wing	S-Body	Base	Time
1)	TWE	MNPM	N	MNPM	MNPM	17.83 s
2)	TWE	MNPM	N	MNPM	HMBP	18.15 s
3)	TWE	MNPM	N	N	N	9.09 s
4)	TWE	TWE	PMFS	MNPM	MNPM	11.84 s
5)	TWE	MNPM	PMFS	MNPM	HMBP	21.72 s
6)	TWE	TC	PMFS	PMFS	PMFS	7.19 s
7)	TWE	MNPM	N	PMFS	PMFS	11.89 s
8)	TWE	TC	PMFS	MNPM	MNPM	12.91 s
9)	VD	MNPM	N	MNPM	MNPM	20.57 s
10)	TWE	DW	PMFS	PMFS	PMFS	6.27 s
CFD						25.5 h

Type	Part	M = 6	M = 10	M = 14	M = 20
Body - Wing (HGV)	Body Exposed	MNPM, TWE	MNPM, TC, TWE	MNPM, TC, TWE	MNPM
	Body Shadow	MNPM, PMS, N	MNPM, PMS, N	MNPM	MNPM
	Wing Exposed	DW, TWE, HFS, VD	TWE, VD	TWE, VD, DB	TWE, DB
	Wing Shadow	PMFS, N	PMFS, N	PMFS, N	PMFS, N
	Base	MNPM / HMBP	MNPM / HMBP / PMFS / N	MNPM / HMBP	MNPM / HMBP
Full - Body (HB-2)	Exposed	TCE, MN, DB, N	TCE, MN	TCE, MN	/
	Shadow	MNPM, N, PMFS	MNPM	MNPM	/
	Base	MNPM, N, PMFS	MNPM / HMBP	MNPM / HMBP	/

Figure 5.32: Best Models Combination

Chapter 6

Conclusions

This work investigated the applicability and accuracy of reduced-order models for the rapid evaluation of aerothermodynamic databases for hypersonic vehicles by developing a MATLAB-based tool that estimates, in a very short time, the main aerodynamic coefficients for arbitrary input geometries.
In order to assess the performance of the tool, reference data were generated by means of high-fidelity viscous steady-state CFD simulations, including aerodynamic coefficients and surface pressure distributions, while accounting for high-temperature effects and real-gas behavior.
The comparison with CFD results showed that, despite their simplified formulation, reduced-order models can provide accurate predictions of the main aerodynamic quantities. In particular, an analysis aimed at identifying the best combination of models as a function of the vehicle geometry led to a significant reduction in prediction errors. For the tested configurations, the mean relative errors averaged over angle of attack remained below 10% for most aerodynamic coefficients and the aerodynamic efficiency. However, some discrepancies were observed in the prediction of the pitching moment coefficient for blunt bodies, such as the HB-2, especially at high angles of attack and when real-gas effects were considered. In these conditions, a reduction in lift and drag coefficients with increasing angle of attack was observed, leading to a decrease in prediction accuracy.
Nevertheless, some limitations must be acknowledged. Due to time constraints and the need to generate a sufficiently large database, a mesh sensitivity study was not performed, and relatively coarse grids were employed. Additionally, the assumption of vibrational equilibrium may affect the absolute accuracy of the CFD reference solutions.
On the other hand, the analysis highlighted the significant computational advantage of reduced-order methods, which reduce computation times from several hours or days to only a few seconds. This makes them particularly attractive for large parametric studies, optimization loops, and early-stage design processes.

In conclusion, the MATLAB console developed in this work, together with reduced-order modeling techniques, represents a powerful and efficient tool for the preliminary assessment of hypersonic vehicle performance.

6.1 Future Developments

Several possible developments could further improve the tool developed within this work:

1. The integration within the console of reduced-order models for the estimation of stagnation-point and surface heat fluxes, extending the tool capabilities toward preliminary aerothermal analysis.

2. The development and integration of a machine-learning algorithm for automatic surface classification, enabling the identification of aerodynamic components (e.g. wings, control surfaces, etc.) and the selection of the most appropriate reduced-order model based on the local geometry.

3. The extension of the tool to include sideslip angle effects and control surfaces, enabling the evaluation of aerodynamic derivatives and preliminary trajectory analysis.

4. The introduction of viscous corrections and a variable specific heat ratio γ, determined through a function depending on the local flight conditions and altitude. In addition, the development of blending functions to ensure a smooth pressure distribution between adjacent surfaces where different reduced-order models are applied.

Appendix A

Taylor–Maccoll Equation

The solution of the Taylor–Maccoll equation presented here is taken from the MATLAB function `Taylor_Maccoll_Supersonic_Cone-master`, developed by Dyuman Joshi [8] for an inviscid and calorically perfect gas.
Starting from the following initial conditions:

$$\begin{cases} \beta_s \quad \text{conical shock angle}, \\ M_1 \quad \text{freestream Mach number}, \\ \gamma = 1.4 \quad \text{ratio of specific heats}, \end{cases} \tag{A.1}$$

the post-shock conditions are evaluated using the oblique-shock relations:

$$\delta_{\text{OSW}} = atan\left(2\cot(\beta)\,\frac{M_\infty^2\sin^2(\beta)-1}{M_\infty^2(\gamma+\cos(2\beta))+2}\right), \tag{A.2}$$

which yield

$$\begin{cases} M_{n1} = M_1\sin\beta, \\ M_{n2} = \sqrt{\dfrac{1+\dfrac{\gamma-1}{2}M_{n1}^2}{\gamma M_{n1}^2-\dfrac{\gamma-1}{2}}}, \\ M_2 = \dfrac{M_{n2}}{\sin(\beta-\delta_{\text{OSW}})}. \end{cases} \tag{A.3}$$

The initial velocity components are then evaluated as

$$\begin{cases} V = \left(\dfrac{2}{(\gamma-1)M_2^2}+1\right)^{-1/2}, \\ V_r = V\cos(\beta_s-\delta_{\text{OSW}}), \\ V_\beta = -V\sin(\beta_s-\delta_{\text{OSW}}) = \dfrac{dV_r}{d\beta}, \end{cases} \tag{A.4}$$

where V denotes the total velocity, V_r the radial velocity, and V_β the angular velocity.
The integration domain for the angle β_s is defined from the shock angle down to a nearly zero value,

$$\beta_{\text{span}} = [\beta_s,\ 10^{-10}],$$

and the initial condition vector is defined as

$$\mathbf{V}_{\text{init}} = [V_r,\ V_\beta].$$

The Taylor–Maccoll equation is implemented by Joshi through the following MATLAB function:

```
function [z0] = TM_Equations(theta,z,k)
% INPUTS
% theta : Integration angle [rad] (= beta)
% z     : Radial and angular velocities
% k     : Ratio of specific heats (= gamma)

% OUTPUT
% z0    : State-space derivatives

z0 = zeros(2,1);   % z0(1) = dVr/dTheta
% z0(2) = d2Vr/dTheta2

A = (k-1)/2;

num = (-2*A*z(1)) - (A*z(2)*cot(theta)) + (2*A*z(1)^3) + ...
(A*z(1)^2*z(2)*cot(theta)) + (2*A*z(1)*z(2)^2) + ...
(A*z(2)^3*cot(theta)) + (z(1)*z(2)^2);

den = A*(1 - z(1)^2 - z(2)^2) - z(2)^2;

z0(1) = z(2);
z0(2) = num/den;
```

Finally, the Taylor–Maccoll equation is solved using the MATLAB routine `ode15s`:

```
sol = ode15s(@TM_Equations, beta_span, V_init, options, gamma);

delta_c = sol.xe;                       % cone angle
Vc2     = sol.ye(1)^2 + sol.ye(2)^2;    % total velocity squared
Mc      = sqrt(2/((gamma-1)*(1/Vc2 - 1))); % Mach number on cone surface
```

Bibliography

[1] John D. Anderson. *Hypersonic and High-Temperature Gas Dynamics*. Second edition published by the American Institute of Aeronautics and Astronautics, 2006. New York: McGraw-Hill, 2006 (cit. on pp. 3, 7, 8, 10, 11, 15–17, 20, 23, 26).

[2] John D. Anderson Jr. *Modern Compressible Flow: With Historical Perspective*. 3rd. New York: McGraw-Hill, 2003 (cit. on p. 6).

[3] Arvel E. Gentry, Douglas N. Smyth, and Wayne R. Oliver. *The Mark IV Supersonic-Hypersonic Arbitrary-Body Program. Volume II: Program Formulation*. Technical Report AFFDL-TR-73-159, Volume II. Long Beach, California: Douglas Aircraft Company, McDonnell Douglas Corporation, Nov. 1973 (cit. on pp. 13, 18, 50, 53).

[4] E. Bonner, W. Clever, and K. Dunn. *Aerodynamic Preliminary Analysis System II. Part I: Theory*. Tech. rep. NASA Contractor Report 182076. Los Angeles, California: North American Aircraft Operations, Rockwell International Corporation, 1991 (cit. on pp. 13, 30).

[5] David Adamczak and Amarshi A. Bhungalia. «Supersonic Hypersonic Arbitrary Body Program (S/HABP)». In: *Thermal and Fluids Analysis Workshop (TFAWS)*. Presentation slides. Air Force Research Laboratory (AFRL/VA). Cleveland, Ohio, Aug. 2003 (cit. on p. 13).

[6] Tianqiang Huang, Guoyi He, and Qi Wang. «Calculation of Aerodynamic Characteristics of Hypersonic Vehicles Based on the Surface Element Method». In: *Advances in Aerospace Science and Technology* 7 (2022) (cit. on p. 30).

[7] G. Cafiero. *Gasdinamica – Oblique Shock Waves: Graphical Representations*. Course material, Politecnico di Torino. 2023 (cit. on p. 52).

[8] MATLAB File Exchange. *Supersonic Flow over a Cone*. `https://it.mathworks.com/matlabcentral/fileexchange/91055-supersonic-flow-over-a-cone`, 2021 (cit. on pp. 53, 54, 117).

[9] G. Cafiero. *Gasdinamica – Shock Expansion Method: Thick Wing Sections*. Course material, Politecnico di Torino. 2023 (cit. on p. 56).

[10] F.Portis, D.D'Ambrosio, A.Schettino, and P.Roncioni. «Evaluating Reduced-Order Methods for Hypersonic Vehicle Aerodynamics». In: *Proceedings of the 75th International Astronautical Congress (IAC)*. Milan, Italy: International Astronautical Federation (IAF), Oct. 2024. DOI: https://doi.org/10.52202/078369-0104 (cit. on p. 61).

[11] Cameron L. Tracy and David Wright. «Modeling the Performance of Hypersonic Boost-Glide Missiles». In: *Science & Global Security* (2020) (cit. on p. 74).

[12] J. Don Gray. *Summary Report on Aerodynamic Characteristics of Standard Models HB-1 and HB-2*. Tech. rep. AEDC-TDR-64-137. Arnold Air Force Station, Tennessee: Arnold Engineering Development Center (AEDC), U.S. Air Force Systems Command, 1964 (cit. on p. 106).

[13] David J. Kinney. «Aero-Thermodynamics for Conceptual Design». In: *42nd AIAA Aerospace Sciences Meeting and Exhibit*. AIAA 2004-31. NASA Ames Research Center. Reno, Nevada, Jan. 2004.

[14] Christopher I. Cruz and Alan W. Wilhite. «Prediction of High-Speed Aerodynamic Characteristics Using the Aerodynamic Preliminary Analysis System (APAS)». In: *AIAA 7th Applied Aerodynamics Conference*. Seattle, Washington: American Institute of Aeronautics and Astronautics, July 1989.

[15] Dominic Dirkx and Erwin Mooij. «Continuous Aerodynamic Modelling of Entry Shapes». In: *AIAA Atmospheric Flight Mechanics Conference*. Portland, Oregon: American Institute of Aeronautics and Astronautics, Aug. 2011.

[16] Mark D. Maughmer, Lisa P. Ozoroski, David M. Straussfogel, and Lyle N. Long. «Validation of Engineering Methods for Predicting Hypersonic Vehicle Control Forces and Moments». In: *Journal of Guidance, Control, and Dynamics* 16.4 (July 1993).

[17] Mark D. Maughmer, Lisa P. Ozoroski, David M. Straussfogel, and Lyle N. Long. *Validation of Engineering Methods for Predicting Hypersonic Vehicle Control Forces and Moments — Volume I: Summary*. Tech. rep. NASA CR-186571. Hampton, Virginia: NASA Langley Research Center, Mar. 1990.

[18] John D. Shaughnessy, S. Zane Pinckney, John D. McMinn, Christopher I. Cruz, and Marie-Louise Kelley. *Hypersonic Vehicle Simulation Model: Winged-Cone Configuration*. Tech. rep. NASA TM-102610. Hampton, Virginia: NASA Langley Research Center, Nov. 1990.

[19] John E. Theisinger and Robert D. Braun. «Multi-Objective Hypersonic Entry Aeroshell Shape Optimization». In: *Journal of Spacecraft and Rockets* 46.5 (Sept. 2009).

[20] H. E. Moore and J. E. Williams. «Aerodynamic Prediction Rationale for Analyses of Hypersonic Configurations». In: *27th Aerospace Sciences Meeting*. AIAA 89-0525. McDonnell Douglas Astronautics Company. Reno, Nevada: American Institute of Aeronautics and Astronautics, Jan. 1989.

[21] Cameron L. Tracy and David Wright. «Modeling the Performance of Hypersonic Boost-Glide Missiles». In: *Science & Global Security* 28.3 (2020), pp. 135–170.

[22] Antonio Iannello. «Valutazione di un codice CFD per flussi ipersonici in non equilibrio chimico e termico». Tesi di Laurea Magistrale. Politecnico di Torino, 2025.